Title

THE EFFECT OF SURFACE-APPLIED REACTIVE ELEMENTS ON THE HIGH TEMPERATURE OXIDATION OF CHROMIUM-CONTAINING ALLOYS

Author

Hou, P.Y.

Publication Date

1986-11-01

Lawrence Berkeley Laboratory
UNIVERSITY OF CALIFORNIA

Materials & Molecular Research Division

THE EFFECT OF SURFACE-APPLIED REACTIVE ELEMENTS ON THE HIGH TEMPERATURE OXIDATION OF CHROMIUM-CONTAINING ALLOYS

P.Y. Hou
(Ph.D. Thesis)

November 1986

Prepared for the U.S. Department of Energy under Contract DE-AC03-76SF00098

DISCLAIMER

The Effect of Surface-Applied Reactive Elements on the High Temperature Oxidation of Chromium-Containing Alloys

Peggy Yen Hou

Ph.D. Thesis

November 1986

Materials and Molecular Research Division

Lawrence Berkeley Laboratory

and

Department of Materials Science and Mineral Engineering

University of California

Berkeley, California 94720

The Effect of Surface-Applied Reactive Elements on the High Temperature Oxidation of Chromium-Containing Alloys

Peggy Yen Hou

Abstract

It is well known that the addition of reactive metals, such as Y, Ce, La etc., or fine dispersions of their oxides, to alloys containing Cr has considerable beneficial effects on the development, growth and mechanical stability of the oxide scales formed at high temperatures. In order to further investigate the cause of these effects, this study is concerned with the influence of the reactive metals and/or their oxides when they are present only on the alloy surfaces prior to the oxidation at 1000°C and 1100°C in 1 atm. O_2. Three binary alloys were used: Co-15wt%Cr, a non-Cr_2O_3 former which will develop the Cr_2O_3 scale with reactive metal oxide additions to the alloy; Co-25wt%Cr, a borderline Cr_2O_3 former and Ni-25wt%Cr, a good Cr_2O_3 former. The oxides of Ca, Ce, La, Y, Hf and Zr were applied as a thin surface coating through the application and decomposition of their aqueous nitrate salts. Y and La were also introduced in their metallic form by ion-implantation.

Unlike the case where the reactive elements are present in the alloy, none of the surface-applied oxides promoted a continuous Cr_2O_3 external scale with alloys that are not already good Cr_2O_3 formers. Some, La, Y and especially Ca oxides, could locally enhance the Cr_2O_3 formation on Co-25Cr at 1000°C, but lost their effectiveness at 1100°C. The degree of such an effect was sensitive to the amount of applied oxides and it appears that in these cases the surface-applied oxides only act as a physical barrier to oxygen. The implanted Y or La also had no effect on the oxidation of Co-15Cr but showed a little effect on the Co-25Cr. With the latter alloy, the implanted species caused the formation of a slightly more Cr-rich scale. The degree of this chromium enrichment increased with increasing implantation dosage. Only when the dose was as high as $1x10^{18}$ ions/cm^2, which corresponds to a peak concentration of approximately 20 at%, could a continuous external Cr_2O_3 scale be promoted. However, this scale did not remain protective, but broke down

after its thickness exceeded 7-8 times that of the implantation depth.

The surface oxides appeared to be most beneficial on the established Cr_2O_3 forming alloy. Surface-applied CeO_2, Y_2O_3 and La_2O_3 were particularly effective in reducing the growth rate of the Cr_2O_3 scale and improving the scale adhesion. The presence of these surface oxides also prevented base metal oxide formation and changed the growth direction of the scale. All of these observed effects were similar to those found when the reactive element oxides were present within the alloys. Nevertheless, the surface-applied ZrO_2 and CaO showed very little effect and the presence of applied HfO_2 even made the oxide scales nonadherent causing a breakaway behavior at the early stage of the oxidation process. Implantation of Y and La produced essentially the same effects as the beneficial surface-applied oxides. Results have provided a better understanding of the improved scale adherence caused by the reactive metal or oxide additions. Possible reasons for the effectiveness of some surface-applied reactive elements and the noneffectiveness of others on the Cr_2O_3 former, and the inability of any of the surface reactive elements to promote a stable, continuous Cr_2O_3 external scale formation on non-Cr_2O_3 formers are discussed.

Acknowledgement

I would like to express my deepest gratitude to Dr. John Stringer of EPRI for his guidance and support throughout the entire course of this work. I am also grateful to John for the amount of freedom he has given me to work independently and the abundance of understanding he has shown concerning my conflicts of family and professional lives.

Special thanks are due to Professor Alan Searcy and to Professor Leo Brewer for carefully reading and correcting this manuscript. I am especially grateful to professor Searcy for his kind helps in many ways and his discussions that often challenge me to think more thoroughly about my research.

Many thanks to the staff at the Heavy Ion Linear Accelerator Center for their assistance in the implantation procedure, to Kin-Man Yu for his help with the Rutherford Backscattering analysis, to Ken Gaugler for showing me how to use the Scanning Auger spectrometer and the SIMS, to Wayland Wong for his help in machining, and to Erlene, Wayland and Elodia for their friendship.

Lastly, I want to thank my parents for all the love and support they have poured into my life. I am also greatly indebted to my husband, without whose love, uncouragement, understanding and support this work could not have been completed.

The financial support from the Electric Power Research Institute under contract number RP 2261, and in part from the Director, Office of Energy Research, Office of Basic Energy Sciences, Materials Sciences Division of the U. S. Department of Energy under Contract Number DE-AC03-76SF00098 is greatly appreciated.

Table of Contents

CHAPTER ONE

Introduction

Metals and alloys operating at high temperatures depend on slow-growing and adherent scales for protection. At present, the best protective oxides are Cr_2O_3 and Al_2O_3, since diffusion through them is relatively slow in comparison to most other oxides; since they are also stable, relatively little difficulty exists in selecting an alloy which contains sufficient chromium or aluminum to provide a protective Cr_2O_3 or Al_2O_3 scale under various service environments. However, their protectiveness is usually greatly hindered by their nonadherent nature. Spallation of these scales usually occurs during service especially under thermal cycling conditions. The stresses developed due to differences in thermal expansion or contraction of the oxide and alloy lead to spallation of the protective oxide scale and as a consequence, excessive rates of metal loss due to oxidation of the less protective base metals.

It is well known that the addition of reactive metals, such as Y, Ce, La, etc., or fine distribution of their oxide particles, to high-temperature heat-resistant alloys has a number of beneficial effects on their oxidation behavior. Whittle and Stringer[1] have extensively reviewed these effects. For both Cr_2O_3 and Al_2O_3-forming alloys, the oxide adhesion is greatly improved under thermal cycling conditions. For Cr_2O_3 formers the rate of growth of oxide is diminished above 900°C; the direction of growth of the oxides is changed, from metal transport out to oxygen transport in; and significantly less Cr is required in the alloy to develop a continuous Cr_2O_3 external scale and to suppress the formation of the base metal oxides.

Numerous investigations have been carried out to ascertain the cause of these effects. Mechanistic models which explain and relate all or most of the observed effects on the Cr_2O_3 forming alloys are the following: Stringer *et al.*[2] postulated that the disperoid particles in the alloy surface act as nucleation sites for the oxides, thus decreasing the internuclear spacing and promoting the formation of a continuous, fine grained Cr_2O_3 scale. As a consequence of the reduced grain sizes, the density of dislocations which are believed to be the cation transport paths in the oxide scale are also reduced. Scale growth therefore results from short-circuit oxygen transport down

the oxide grain boundaries. Golightly *et al.*[3] suggested that the growth of the Cr_2O_3 scale without any reactive element addition is controlled largely by the outward diffusion of Cr^{3+} ions, coupled with a small oxygen inward diffusion. Lateral growth of the scale occurred near the scale/gas interface causing large areas to grow out of contact with the alloy. Conversely, in the presence of the additions which segregate to oxide defects, the outward transport of cations is greatly reduced, allowing the scale growth to be controlled by the inward transport of oxygen, eliminating lateral oxide growth within the scale. This leads to total contact between the scale and the alloy. According to these two models, improved scale adhesion is considered to be caused by the change in the growth mechanism of the scale. However, these two effects may not necessarily be related, since with Al_2O_3-forming alloys, great improvement in adhesion is often observed to result from active metal additions without any other obvious effects. A number of explanations have been given for the improvement in adhesion alone[1]. The functions of the additives are believed to be either 1) to act as vacancy sinks, therefore preventing vacancies from condensing at the scale/alloy interface to generate voids, 2) to provide preferential diffusion paths for oxygen to facilitate inward growth of internal oxide pegs, or 3) to improve the interfacial strength of the scale/alloy interface either by segregating to the interface to enhance bonding[4],[5] or by gettering impurities which normally diffuse from the bulk of the alloy to the interface to weaken it.[6],[7]

Although there have been many hypotheses proposed, none is at present universally accepted. Interestingly, however, one of the original patents[8] concerning the reactive element addition indicated that these elements were not only effective as alloying additions but were effective to similar degrees when applied as a surface coat with a thickness of approximately 2-3 μm. The coatings can be the elements, their oxides, hydroxides, or other salts which would decompose to oxides at high temperature. Furthermore, Antill *et al.*[9] demonstrated that ion-implantation of the reactive elements into a subsurface depth of less than 0.1 μm can also be beneficial. From a pratical point of view, the surface deposition is attractive as a means of avoiding potential probloms associated with alloying additions, such as the difficulty in alloying or any adverse effect on the mechanical properties of the alloy which result from the presence of the reac-

tive elements or their oxides. Furthermore, the surface-application of salts is valuable for its simplicity. From the point of view of elucidating the mechanism of the 'reactive-element effect', these superficial techniques are particularly interesting, since several aspects of the most successful current model imply that the reactive element is present within the alloy.

Very recently, several investigators have studied the effects of these superficial treatments to heat resisting alloys and have confirmed that beneficial effects can be obtained. Application techniques include ion–implantation[10]–[24] as well as surface oxide coats.[25]–[30] However, these studies concentrated on alloy systems that are already strong Cr_2O_3 formers; therefore, they neglect one of the important effects, that dispersions of the reactive element oxides in the alloy could promote Cr_2O_3 scale formation on ordinarily non-Cr_2O_3 forming alloys.[31]–[34] Furthermore, earlier investigations concerning the effects of surface oxide coats[25]–[30] have not address the mechanistic issues, most only concentrating on evaluating the performance of the surface additives on Cr_2O_3-forming alloys.

The present study is concerned with the effect of ion-implanted reactive elements and of reactive metal oxide deposits produced by the thermal decomposition of aqueous nitrate solutions on alloy systems ranging from non-Cr_2O_3-formers to good Cr_2O_3-formers. The study concentrates on whether these surface deposited reactive elements or their oxides can promote Cr_2O_3 scale formation on non-established Cr_2O_3 formers, and on characterization of the effects they have on established Cr_2O_3 formers. Results are compared with those found when these oxides are present in the alloys in order to gain further understanding of the 'reactive element effect'.

Three binary alloys are used: Co-15wt%Cr, which normally does not form Cr_2O_3, but can be induced to form protective Cr_2O_3 scale by an internal dispersion of reactive metal oxides;[34] Co-25wt%Cr, a borderline alloy which does not normally form Cr_2O_3 at high oxygen pressures, but will at low oxygen pressures;[35] and Ni-25wt%Cr, which is a good Cr_2O_3 former.[36] The nitrates of Ca, Ce, Hf, La, Y and Zr are selected since all of them except Ca have been shown to be beneficial as alloying additions. Ca was included because it forms one of the most stable oxides and because it was applied as a surface coat in the original patent[8] and proved to be particularly beneficial.

Yttrium was chosen from the limited ion sources available for the implantation studies since it has been the most widely studied element in recent ion-implantation works. Some preliminary studies on Co-15Cr and Co-25Cr alloys used lanthanum as the ion source, and xenon was used as the inert element for the study of radiation effects caused by the implantation process on subsequent oxidation behaviors.

A more detailed summary of the reactive element effects due to alloying additions and previous models proposed for their explanations are given in the next chapter. Review of ion-implantation and surface oxide application works are also included. The main part of the thesis containing the experimental results and discussions are given in chapters four and five where the effects due to the surface applications on normally non-Cr_2O_3 formers or Cr_2O_3 formers are presented separately.

CHAPTER TWO

Technical Background

2.1 Effects of Alloying Additions of Reactive Elements and Their Oxides

It was discovered over fifty years ago that additions of rare earth metals as melt deoxidants to Nichrome (Ni-20wt%Cr) heating elements substantially increase their lifetimes in cyclic heating and cooling tests[37] by increasing the adhesion of the protective scale to the alloy. The amount of the rare earth additions were 0.01-0.5 wt%. In a later patent,[8] it was found in fact that elements from groups IIA, IIIA, IVA and VA of the periodic table could produce similar beneficial effects, although their effectiveness decreased on passing from group II to group V, but increased with increasing atomic weight within a particular group.

Subsequent work carried out by various other investigators indeed has confirmed that a wide range of additions can have a similar effect, as long as the additions form a more stable oxide than the Cr_2O_3 or Al_2O_3 which can be formed by oxidizing the alloy. Therefore, the effect, which was at first called the 'rare-earth effect' is now called the 'reactive element effect', and the additions are commonly referred to as oxygen active element additions, reactive element additions or active element additions. In this work, the term 'reactive elements' is chosen. A reactive element is often abbreviated as RE, and reactive element oxide as REO.

As mentioned in the introduction, the effects of these reactive elements on the Cr_2O_3-forming alloys are fourfold. First of all, selective oxidation of chromium is enhanced. This effect is particularly noticeable on alloy systems which normally do not have enough chromium to form a complete external Cr_2O_3 scale. With the presence of the reactive elements and especially their oxide dispersions, an external Cr_2O_3 scale can be promoted. This has been demonstrated by Stringer and Wright[32] on Co-21wt%Cr-3vol%Y_2O_3, by Davis *et al.*[31] on Ni-13.5wt%Cr-1vol%ThO_2, by Wright and Wilcox[33] on Fe-16wt%Cr-3vol%Y_2O_3, and by Whittle *et al.*[34] on Co-10wt%Cr-1wt%Hf, Ti and Zr.

The work by Whittle *et al.*[34] was especially interesting. The ternary addition of 1 wt% Hf,

Ti or Zr did not show any effect on the oxidation behavior of the Co-Cr alloy. But, after converting the added Hf, Ti or Zr metal to its oxide during an internal oxidation pretreatment, subsequent oxidation produced a continuous, well adhered, protective Cr_2O_3 layer, with very little Co-containing oxides. Thus, in terms of promoting selective oxidation of chromium, an oxide dispersion is clearly more effective than the corresponding active metal addition. In an alloy system which normally would develop the Cr_2O_3 protective scale upon oxidation, the reactive element addition simply reduces the transient stage of oxidation. In that the time it takes to develop the continuous Cr_2O_3 layer is shortened and there is less base metal oxidation.

The second effect of the reactive element addition on Cr_2O_3-forming alloys is to reduce the growth rate of the Cr_2O_3 scale. Francis and Whitlow[38] suggested that while the oxidation rate of an Fe-25wt%Cr alloy is approximately parabolic, that of an Fe-25Cr-1Y alloy is asymptotic. Beltran[39] reported a cubic rate behavior of Cr_2O_3 growth on a Co-30Cr-0.1Y alloy instead of the parabolic-type behavior observed with the binary alloy. Whatever the resulting rate law of Cr_2O_3 growth is with the reactive element addition, it is undoubtable that the growth rate on the reactive element-containing alloy at elevated temperatures is considerably less. At 900°C, the reduction in growth rate is only marginal, but as the oxidation temperature increases, the reduction becomes greater.

Inert platinum markers placed on Ni-20wt%Cr-2vol%ThO_2[40],[41] or Ni-20wt%Cr-3vol%Y_2O_3[2] were found at the scale/gas interface after oxidation, but on a dispersion-free alloy, Ni-30wt%Cr, they were found at the scale/alloy interface.[40] This difference clearly indicates that the dispersion produces a change in growth mechanism. While the Cr_2O_3 scale formed on the dispersion-free alloy grew predominantly by outward transport of chromium through the scale, it grew predominantly by inward transport of oxygen on the dispersion-containing alloys.

Lastly, the addition of reactive elements or the dispersion of their oxides promotes good scale adherence. This conclusion is evident both from cyclic oxidation tests[42]–[45] and from the reduction in scale spallation at the end of isothermal exposures. The work of Michels[45] for example, showed that the final weight change on a Ni-20 wt%Cr alloy after 504 hours of thermal cycling

oxidation at 1100°C was a negative 32.4 mg/cm^2, indicating tremendous metal loss. On the other hand, the same alloy containing dispersions of ThO_2, Y_2O_3, or La_2O_3 showed an average of only 0.42 mg/cm^2 weight increase under the same oxidizing conditions.

For alloys that form Al_2O_3 as the external scale, the only apparent effect of the reactive element additions is to improve scale adhesion. It was noted by Tien and Pettit[46] that inert platinum markers placed on the surface of an iron-based Al_2O_3-forming alloy prior to oxidation were always found at the gas/scale interface irrespective of whether the alloy contained RE or REO additions. The growth of the Al_2O_3 scale was suggested to be via oxygen diffusing inward along oxide grain boundaries. This growth mechanism was recently confirmed by O^{18} tracer studies of Al_2O_3 scale formation on NiCrAl alloys.[47] The growth rate of the Al_2O_3 scale however, was variously reported to be either slightly decreased,[48]–[51] unaltered[3],[38],[46] or slightly increased[46],[51],[52] by different reactive metals or their oxides added to different alloy systems. Similar discrepancies exist in reports of the effect of the same reactive metal addition to similar alloy systems.[48],[53] Therefore, it is not entirely clear whether there is any real reduction in rate with Al_2O_3 and it is generally accepted that the addition of reactive metals or oxides does not dramatically affect the growth rate of Al_2O_3 scales. Similarly, the additions seem to show little effect, if any, in reducing the transient stage of oxidation or reducing the amount of Al required to form Al_2O_3 as they do when present in Cr_2O_3-forming alloys.

The improved adhesion of the Al_2O_3 scales can be related to the differences in morphologies observed between the scales formed on reactive element-doped or undoped alloys. The first feature was the lack of voids at the scale/alloy interface under the adherent oxide formed on reactive metal-containing alloys. The alloy surface after the Al_2O_3 scale had been removed was completely covered with imprints of oxide grains for the doped alloys whereas there were numerous smooth areas, representing areas of no contact between scale and alloy, for the addition-free alloys. The second feature was the relative smoothness of the adherent Al_2O_3 scale at the gas/scale interface. Such scales did not develop a convoluted morphology with oxide ridges as often observed with dispersion-free alloys. Lastly, fingers of Al_2O_3 containing the reactive metal additions were found

penetrating into the alloy from the scale. These intrusions or "pegs" may have different morphologies with different reactive metal additions and their concentration was found to increase with increasing active element content in the alloy.[49]

2.2 Models Explaining the Effects of Reactive Element Additions

2.2.1 Selective Oxidation of Chromium

The ability of reactive metals or their oxides present in Cr_2O_3-forming alloys to promote the protective Cr_2O_3 scale development was first suggested by Davis *et al.*[31] to be due to an enhanced chromium diffusion in the alloy. Studies[54],[55] have shown that the diffusivity of chromium in a dispersion-containing (ThO_2 or CeO_2) Ni or Ni-Cr alloy was an order of magnitude higher than that of a dispersion-free alloy. Since the transition between external scale development and internal oxidation is dependent upon the interdiffusivity of the scale forming species,[56] an increase in the diffusivity of chromium in the alloy (D_{Cr}^{alloy}) would naturely enhance the external Cr_2O_3 scale development.

More recent diffusivity measurements carried out by Seltzer *et al.*[57],[58] on Y_2O_3 and ThO_2 containing Ni-Cr and Co-Cr alloys have shown that the presence of dispersoids alone does not enhance the diffusivity of chromium in the alloy. However, D_{Cr}^{alloy} increases with decreased alloy grain sizes. When the alloy grain size of both the dispersion-containing and the dispersion-free alloys were the same, no enhanced D_{Cr}^{alloy} was observed. Their observations were in accord with those of Giggins and Pettit,[59] which showed that Cr_2O_3 developed on Ni-Cr alloys more readily over alloy grain boundaries than over the bulk of the grains, and on cold-worked surfaces than on polished ones. Since both active metal and oxide dispersions tend to stabilize a fine alloy grain size,[60] the enhanced D_{Cr}^{alloy} observed earlier by Fleetwood[54] and Wenderott[55] can be explained as a result of the decreased grain sizes produced by the oxide dispersions. Thus, it is possible that the presence of the active metals or oxides decreases alloy grain sizes which in turn increases D_{Cr}^{alloy} and aids the initial development of the Cr_2O_3 scale. Nevertheless, as described in the previous section, Co-15wt%Cr alloys containing 1wt% Ti, Zr or Hf in the temperature range 1000°-1200°C failed to form a continuous Cr_2O_3 scale, but after an internal oxidation pretreatment converting

the Ti, Zr or Hf to their oxides without oxidizing the Cr in the alloy, a continuous Cr_2O_3 scale was developed.[34] There was no change in alloy grain size as a result of the internal oxidation and it is equally unlikely that much substructure was generated by this treatment. This work indicates that the enhanced chromium diffusivity in the alloy caused by the decreased grain sizes cannot be a major factor in promoting the initial protective scale development. Rather, the evidence supports the mechanism suggested by Stringer *et al.*[2] that the oxide dispersions reduce spacings between the first nuclei formed on alloy surfaces and thus promots a continuous Cr_2O_3 scale.

The model proposed by Stringer *et al.*[2] has been briefly described in the introduction section. A summary of it is presented schematically in Figure 1 using a Ni-20wt%Cr alloy with and without a 2vol%ThO_2 addition as an example. The dispersoid represents surface discontinuities which are postulated to act as heterogeneous nucleation sites. It is not necessary to postulate that the dispersoids preferentially act as nucleation sites for the Cr_2O_3 nuclei. Their function is only to decrease the distance between adjacent Cr_2O_3 nuclei and thus reduce the time required for the lateral growth process to form a complete layer of Cr_2O_3 and terminate the formation of base-metal oxides. Some indirect experimental evidence for this model can be cited as the following: the grain size of the oxide over the dispersion-containing material is usually between five to ten times smaller than the oxide over dispersion-free materials; oxide dispersions always are found more effective in promoting the initial scale development than metallic additions; stable nitride dispersions have effects similar to oxide dispersions, at least in Fe-Cr alloys;[61] and *in situ* oxidation of Ni-Cr-ThO_2 alloys in a high voltage microscope indicated that ThO_2 particles along with grain boundaries, slip steps and other inclusions acted as preferential nucleation sites for oxidation.[62]

The nucleation of Cr_2O_3 on a Ni-20Cr based alloys with or without the dispersion of Y_2O_3 was recently studied by Brasi *et al.*[63] The alloys were oxidized at 1000°C in H_2/H_2O mixtures in which the oxygen partial pressures ranged between 10^{-19}-10^{-24} atm. Characterization of the oxides formed was mainly carried out using analytical electron microscopy. It was concluded that the earilier development of the protective Cr_2O_3 scale on dispersion-containing alloys could not be

accounted for by the mechanism proposed by Stringer *et al.*,[2] since no preferential nuclation of any oxide particle was oberved at dispersoid particles intersecting the specimen surface. Nevertheless, their results also showed that the oxide grains of the Cr_2O_3 scale were smaller on the Y_2O_3-containing alloy, and a higher number density of Cr_2O_3 nulei were present when the Cr_2O_3 scale was not yet continuous. It seems that both of the above observations could support the 'nucleation model'. Furthermore, direct observation of Y_2O_3 acting as preferential nucleation sites may not have been possible on a system where the Y_2O_3 particles, with diameters 5-100 μm, were uniformly distributed, because the earliest observation made was with a surface coverage of 40% or more of Cr_2O_3 with grain sizes ranging between 50-80 μm.

2.2.2 Reduced Scale Growth

Essecntially three main mechanisms have been proposed to explain the reduction in scale growth rate and possible modification to the transport process brought about by metallic or oxide additions. The mechanisms are: a) doping effects; b) formation of a partial or complete blocking layer; and c) blocking of short circuit diffusion paths in the scale.

Doping Effects

Investigators[38],[45] who explained the decreased oxidation rate by doping effects essentially make use of the Wagner-Hauffe model which proposes that when a foreign ion or dopant is added to a nonstoichiometric oxide, electroneutrality must be maintained by a redistribution of electronic and ionic defects. For example, with a metal-deficient p-type oxide like NiO, addition of trivalent ions such as Cr^{3+} increases the concentration of cation vacancies but decreases the concentration of electron holes. Since transport of cations through the cation vacancies is rate determining in scale growth, there is an observed increase in oxidation rate. But the model requires that the true defect structure of the parent oxide be fully understood, that the foreign cations enter normal cation positions in the parent oxide, and that the growth of the oxide proceeds predominately by lattice diffusion. For Cr_2O_3, none of the above criteria are met with certainty. There is some evidence that at temperatures above about 1200°C Cr_2O_3 is an intrinsic electronic conductor,[64] but other evidence[65]–[67] indicates that Cr_2O_3 is a p-type semiconductor. The main

weakness of the doping argument lies in the apparently equal efficiency of a wide range of additions regardless of their charge states. Therefore, it was later suggested[13] that ionic size effects are more likely to explain any changes in transport rate through scales than Wagner-Hauffe doping. The presence of the larger additives (for example, Y^{3+} is 35% larger than Cr^{3+}) in the growing Cr_2O_3 layer would induce stress. This stress is believed to be relaxed by cationic vacancy trapping on the larger ions forming an M-V_{Cr} complex, which would account for the reduced diffusion flux in the active metal doped Cr_2O_3 and hence for the reduced growth rate of the Cr_2O_3 scale. However, fine dispersions of Al_2O_3 in Ni-20Cr have been shown to produce the same effects as the Y_2O_3 dispersion,[44] and the ionic redii of Al^{3+} is certainly comparable to that of Cr^{3+}.

Blocking Layer

Wood and Boustead[68] suggested that the asymptotic growth rate obtained by additions of Y or Gd to Fe-Cr alloys was more readily explained by some time-dependent phenomenon, for example, the development of a layer of compound such as $YCrO_3$ or Y_2O_3 at the oxide/alloy interface. Detailed investigation was unable to detect a complete layer, although a Y-rich compound was found along about 50% of the scale/alloy interface. Beltran[39] suggested that the reduced oxidation rate of Co-30Cr containing 1wt% Y might be caused by the precipitation of rare earth oxides in the alloy matrix, with the precipitates acting as a "set of sieves in series" to block diffusion of chromium. Giggins and Pettit[40] on the other hand proposed a model in which the dispersoid particles present in the scale reduce the scale growth rate by decreasing the cross-sectional area of Cr_2O_3 available for transport of chromium. This model was later proved to be incompatible with experimental results by Stringer *et al.*,[2] since the observed reduction in oxidation rate would require a much higher concentration of dispersoid particles present in the scale to effectively act as a blocking layer. Furthermore, the "blocking layer" argument probably falls down because even relatively small additions of either active metals or their oxides can produce reductions in oxidation rates which would require a very considerable reduction in diffusion areas.

Blocking Short Circuit Paths

Instead of envisaging the dispersoid particles as reducing cross sectional areas for the transport of chromium in the scale, Golightly *et al.*[3] suggested that these particles segregate to oxide grain boundaries and suppress cation transport. Stringer *et al.*[2] also suggested that the dispersoids only block short circuit diffusion paths for chromium. However, they believe that the principal paths for cation diffusion in the Cr_2O_3 scale are not grain boundaries but dislocations, since it has been reported[69] that grain boundaries in ionic solids are short circuit paths for anions, not for cations. The presence of the dispersoid in the alloy was found to reduce the oxide grain size. If these grain sizes were reduced to a level corresponding to the interdislocation distance in a pile-up, a single dislocation is no longer stable within the grain and will move to the grain boundary where it ceases to be a cation diffusion path. Thus, if the short circuit diffusion paths for chromium in Cr_2O_3 were indeed dislocations, reducing the grain size of the oxide below certain limits would reduce the density of the paths and hence the diffusion rate. Equally, the oxygen diffusion rate via grain boundaries will be increased due to the reduced oxide grain sizes and a reversal in growth direction occurs. Unfortunately, sufficiently precise data to compare the actual transport rates during oxidation with those expected for bulk or short circuit diffusions are not available. It is at this point impossible to verify the validity of these hypotheses that the mechanism of reducing the scale growth rate is indeed by blocking or eliminating short circuit diffusion paths.

2.2.3 Improved Scale Adhesion

The effect of improving the scale/alloy adherence has been the aspect studied in most detail, and several mechanisms have been proposed. Essentially, these are independent of whether the alloy contains a metallic addition of the active element or a dispersion of its oxide. The added active elements will be oxidized preferentially to chromium or aluminum ahead of the oxide/alloy interface due to their high affinity for oxygen, and since the additions are present in very low concentrations, the resulting oxides will be in the form of discontinuous internal oxide particles in the alloy.

The proposed mechanistic models for the improvement in scale adherence are briefly summarized in this section. It is important to realize that although these models may differ a great

deal from one another, they are not necessarily mutually exclusive.

Graded Seal Model

The graded seal mechanism is based on the supposition that a layer of compound oxide is developed between the surface scale and the alloy which has a thermal expansion coefficient intermediate between that of the scale the the substrate.[70] However, there are very few systems in which a complete, or even partial layer of a compound oxide has been observed experimentally.

Vacancy Sink Mechanism

Stringer[71] first proposed that oxide particles produced in an alloy by internal oxidation or alloying acted as receptive sinks for cation vacancies, thereby preventing void formation and consequent loss of adhesion at the alloy/scale interface. There has been indeed clear evidence that the presence of an active metal or an oxide dispersion in the alloy[46],[49] or in a shallow implantation region[19],[21] minimizes the development of voids at the alloy/scale interface. Allam *et al.*[49] even noted a reappearance of voids after very long exposures on alloy systems containing very low concentrations of active elements (0.05wt% addition of Hf or Y). Such behavior was not observed when the active metal concentrations were higher, indicating a continuing supply of vacancies and that the vacancy sinks can eventually become saturated. The question arises however, as to the source of vacancies which condense at the scale/alloy interface to form voids.

Oxide Keying or Pegging

As mentioned in section 2.1, one of the major morphological differences observed between dispersion-free and dispersion-containing Al_2O_3-forming alloys is the presence of oxide pegs or fingers penetrating into the alloy substrate from the scale. Lustman[72] and Wukusick and Collins[73] suggested that this internal and intergranular oxidation, stimulated by the reactive element addition, can key the scale to the alloy substrate, and therefore, increase the scale adherence. Studies by Allam *et al.*[48],[49] have shown that the morphology and distribution of the pegs are critical in improving scale adhesion. A finer, more uniform distribution of small oxide pegs is more efficient in combating scale spallation. Large pegs on the other hand appear to be capable of initiating scale failure. These investigations also demonstrated that these pegs consisted primarily of

Al_2O_3, and are formed by enhanced inward growth of Al_2O_3 along the incoherent boundary between the active element oxide and the alloy substrate. More recent study by Hindam and Whittle[74] however, indicated that the pegs actually develop by preferential diffusion along active element oxide dispersions incorporated within the Al_2O_3 scale. The active element oxide precipitates (HfO_2 was used in their study) within the scale act as short circuit diffusion paths for oxygen transport leading to preferential localized scale thickening in the neighborhood of these particle.

According to Hindam and Whittle[75], the reasons a peg-like morphology or a tortuous alloy/scale interface can improve scale adhesion are the following: relief of stresses by the two-phase pegs-containing region acting as a "graded seal" which gradually accommodates the variation in the physical properties of the two phases (scale and alloy); impediment of crack propagation due to the large interfacial contact areas associated with the peg microstructure; and stress relief achieved by plastic deformation of the alloy protrusions trapped between the pegs.

Although the formation of oxide pegs which mechanically key the scale to the substrate has been recognized as a pertinent factor in improving scale adhesion, there are alloy systems which do not form any pegs but still remain adherent under severe cyclic oxidation conditions[7],[76]. Furthermore, active element additions to Cr_2O_3-forming alloys do not generally lead to appreciable oxide peg development, but improvement in scale adhesion is usually observed.

Improved Mechanical Properties of the Scale

This proposal asserts that the finer-grained oxide produced on an alloy containing an addition or dispersion will be more easily deformed via grain boundary sliding, thereby allowing the relief of growth and thermally induced stresses which would otherwise cause spallation.[42],[46],[77] Recent studies by Delaunay *et al.*[78] using *in situ* deflection measurements showed that the compressive stresses developed during oxidation were much less for yttrium-containing heat-resistant alloys than for Y-free alloys. The presence of yttrium in the scale was believed to improve its plasticity by increasing the amount and/or mobility of vacancies, since yttrium added in very low amounts always improves alumina sintering.[79] Hollenberg and Gordon[80] on the other hand, studied the effects of different dopants on the creep behavior of polycrystalline Al_2O_3 found

that although Fe^{2+} and Ti^{4+} increased the creep rate of alumina, Cr^{3+} showed no apparent effect. Furthermore, Kuenzly and Douglass[52] suggested that the scale plasticity is actually decreased by the addition of yttrium since Y_2O_3, $YAlO_3$ and $Y_3Al_5O_{12}$ form at grain boundaries and inhibit plastic deformation of Al_2O_3 by a grain boundary sliding mechanism.

Modification of Scale Growth Process

Golightly *et al.*[3] have suggested that in addition to inward oxygen diffusion along Al_2O_3 grain boundaries, outward transport of aluminum occurs, probably along line defects in the oxide. Reaction between the inward- and outward-diffusing species results in the formation of oxide within the existing scale layer. This lateral growth of oxides within the scale produces large compressive stresses and leads to localized detachment of the scale from the underlying alloy. When reactive metal oxides are present in the scale, they most likely segregate to line defects and block short circuit diffusion of aluminum outward. This would eliminate any oxide lateral growth within the existing scale, hence preventing the formation of convoluted scale morphologies and maintaining a much better scale/alloy contact which then gives rise to enhanced scale adherence.

The effectiveness of ion-implanted yttrium on a Al_2O_3-forming alloy was also explained by Lau *et al.*[19] to be related to the scale growth process. These authors suggested that the implanted yttrium acts as a catalyst on the alloy surface to modify the nucleation and growth of the oxide scale. As a consequence, the resulting oxide has a much finer grain size which can accommodate higher stress and thus improve scale adherence.

Improved Chemical Bonding at the Scale/Alloy Interface

The adhesion of oxide scales to the underlying substrate is clearly dependent upon the nature of the atomic bonds which are developed across the scale/alloy interface. McDonald and Eberhart[81] suggested that the presence of a highly oxygen-active element at the alloy/oxide interface by some means improved the atomic bonding between the scale and the alloy substrate.

A recent study by Smialek and Browning[5] using *in situ* Auger and XPS measurements has confirmed the segregation of active metal dopants (Y and Zr) to the Al_2O_3/NiCrAl interface. The presence of these oxygen active elements at the interface is believed to strengthen its bonding since

oxide-metal bonding properties have been found to correlate closely with the free energy of formation of the oxide ($\Delta G_{f,oxide}$). Those metals with a more negative $\Delta G_{f,oxide}$ were found to exhibit a stronger contact with sapphire.[81],[82] Furthermore, results from molecular orbital studies which modeled the bonding of Y, Al, Ni atoms to Ni_9 clusters and AlO_6, YO_6 clusters to Ni_9, Al_{10} and Y_{10} clusters[4] predict a substantial bond enhancement should a few monolayers of yttrium exist between the Al_2O_3 scales and the nickel substrate.

However, arguing against this is the observation that the presence of an Al_2O_3 dispersion in Fe–25Cr–4Al[46], or in aluminized Co-10Cr-1Al,[83] both Al_2O_3-forming alloys, also results in a significant increase in adhesion.

Impurity Gettering Model

While the previous model suggests that the presence of active metals or oxides at the scale/alloy interface increases the chemical bonding and strengthens the interface, this model[6],[7] proposes that the bonding at the interface is intrinsically strong. It is the segregation of impurities, particularly sulfur, to this interface that makes it weak. The function of active elements present in the alloy is then to getter these impurities, preventing them from segregating to the interface.

The detrimental effect of sulfur on oxide-metal bonding was first suggested by Briant and Mulford[83] in their study of sulfur segregation and grain boundary embrittlement of Ni-base superalloys. The bond weakening effect of sulfur at grain boundaries in metals has been modeled by quantum chemical molecular orbital techniques[84]. This study found that sulfur (and other common impurities) served to pull electrons away from metal atoms by the formation of heteropolar M-S bonds and prevent these electrons from contributing to the stronger metallic-type bonds across the grain boundary. It is uncertain however, if an analogous bond weakening should occur at a metal/oxide interface.

The sulfur gettering ability of the active elements is related to the more negative free energy of formation of their sulfides. Smeggil *et al.*[7] in their studies, observed numerous active metal sulfides in the alloy after oxidation. The resulting Al_2O_3 scale was adherent without any

measurable sulfur concentration at the scale/alloy interface. Furthermore, the addition of Y_2S_3 particles to the NiCrAl alloy resulted in a detrimental effect on scale adhesion. This fact was explained by Smeggil *et al.*[7] to be due to the liberation of "free sulfur" from the Y_2S_3 to segregate to the interface.

The effectiveness of dispersed oxides like Y_2O_3 in enhancing scale adhesion is accounted for in this model by suggesting that sulfur segregates to the dispersoid/alloy interfaces instead of to the critical scale/alloy interface. Such segregation can occur regardless of the type of oxide dispersions present, even Al_2O_3.

2.3 Effects of Surface Applied Reactive Elements and Their Oxides

2.3.1 Surface Salt Deposition

As early as 1945 Pfeil[8] reported in a patent that surface application of reactive element oxides to chromium-containing heat-resistant alloys can increase their service life. The reactive element oxides were applied as surface films via hot dipping or anodic deposition of the nitrates of these elements. In the former case, the article was simply dipped into the nitrate solution while hot and withdrawn while still hot enough to evaporate off the solvent. A slightly acidic solution containing 10wt% of the salt was found to give a satisfactory film. With anodic deposition, the article to be plated was made the anode immersed in the nitrate solution. The voltage was increased slowly from 2 volts until deposition was indicated by the evolution of gas around the article. Subsequent heat treatment decomposed the nitrate salts to oxides. The coated alloys were then tested in air at 1200°C. While the untreated Ni-20wt%Cr alloy showed a life of 33 hours at 1200°C, the same alloy treated with surface oxide films was found to last 60-65 hours under the same conditions. It was noted that the surface films were not as effective as reactive elements included in the alloy. Also, it was found necessary that the film produced a fine dispersion of the reactive elements on the surface. This dispersion need not be continuous, although the particles that compose it should be uniformly distributed, and the film must be gas-permeable.

Further studies using the nitrate salt deposition method were not carried out until much

later. Landkof *et al.*[30] followed the hot dipping method reported in the original patent closely and studied the effect of six different reactive element additions (Y, La, Ce, Ca, Hf and Zr) to 304 and 310 stainless steels and to Inconel 738. Tyzack *et al.*[25] also used the hot dipping method. They applied CeO_2 on a 20Cr/25Ni/niobium stabilized (20/25/Nb) austenitic stainless steel via an alcoholic solution of ceric ammonium nitrate. Bennett *et al.*[29] studied the oxidation of the same stainless steel and the effect of sol-gel applied CeO_2 and SiO_2 and that of chemical vapor deposited SiO_2. The sols were essentially a stable dispersion of colloidal units of hydrous oxides or hydroxides in a liquid. The colloidal sizes range from 200 nm to 1 μm. After the sol was applied to the samples by dipping, spin coating or electrophoresis, it was dried and transformed to a gel. The last stage of preparation involved firing of the gel at temperature above 150°C. The gel then became consolidated as a ceramic with a density dependent upon the degree of aggregation of the basic colloidial units in the sol. The chemical vapor deposition (CVD) was carried out in two stages. These consisted of preoxidation of the steel in steam followed by the deposition of silica produced by the decomposition of tetraethoxysilane from a flowing stream carrier. Ecer *et al.*[28] also applied oxide dispersions directly on alloys rather than using the nitrate salts. Powders of MgO, CeO_2, Cr_2O_3 or Co_3O_4 were mixed in alcohol. Specimens of Ni-50wt%Cr or Fe-25wt%Cr were coated by dipping in the alcohol slurry and were air dried. The effect of CeO_2, Cr_2O_3 and Co_3O_4 powders on the oxidation of Ni-50Cr and the effect of MgO and CeO_2 on the oxidation of Fe-25Cr were studied.

Except for the CVD coating on silica, which can be as thick as 27 μm,[27],[29] all of the various methods produce surface coatings not thicker than 4 μm. The thinnest is that of CeO_2 produced by the sol-gel method, 0.3 μm thick.[29] Although Landkof *et al.*[30] using Auger microscopy reported the applied Y_2O_3 coating to be only 0.08 μm all of their SEM micrographs showed a much thicker coating, about 2-3 μm thick. The Auger analysis was probably made on an area with very thin coverage since it is characteristic for these coatings to be nonuniformly distributed on the specimen surface.

In general, the presence of these surface reactive element oxides on the various alloys studied

affects their oxidation behavior in two ways: they reduce the oxidation rate and improve the scale adhesion. However, this is not always true with every reactive element studied. Among the six different surface oxide coats applied to the Type 304 steel, Ce, Y and La oxides were effective but not the oxides of Hf, Zr or Ca.[30] Also, dispersions of CeO_2 particles on Fe-25Cr alloy improved the scale adhesion and greatly reduced its growth rate, while MgO powders gave no improvement in oxidation rate but only in scale adhesion.[28] Although there have not been studies involving alloying Ca or Mg for a direct comparison, the addition of Hf or Zr in alloys is known to be beneficial.[34] The difference in behavior between bulk alloying of these elements and surface coating of their oxides was explained by Landkof *et al.*[30] to be due to the anisotropic nature of these oxides, making them susceptible to cracking which promotes scale separation from the base metal.

Among the surface dopants which are beneficial, only slight variations exist in their relative effectiveness. On 304 s.s., the order of effectiveness decreases from yttrium oxide to cerium oxide to lanthanum oxide.[30] The ceria and silica sol-gel coatings applied to preoxidized 20/25/Nb stainless steel were both beneficial, with the silica coating being slightly more effective.[29] Preoxidation of this steel prior to the coating process was essential for reducing the oxidation rate of the alloy. Bennett *et al.*[29] suggested that the preoxidized steel surface, which has a spinel oxide layer approximately 1 μm thick, possibly facilitates the initial laying down and/or adhesion of the coating. No evidence of interaction between coatings and the preoxidized layer was observed. Coatings which are less than about 2 μm thick can produce a noticeable effect, but the oxidation resistance of the steel is progressively improved by increasing the coating thickness up to $\sim$ 10 μm.

No compositional changes of the resulting oxide scales were observed with the ceria or silica sol-gel coated 20/25/Nb steel.[29] This is in contrast to the study of Tyzack *et al.*[25] who found that the scale developed on this alloy after a CeO_2 deposition was richer in chromium without any presence of the base metal, iron. The elimination of fast-growing iron oxide spikes by the presence of these surface reactive element oxides was also observed on Fe–25Cr[28] and on 304 s.s..[30] In both cases, the scale which developed was a fine grained, thin layer of Cr_2O_3. The oxide grain size was found to be 1/5 that of the scale formed on a bare alloy.[28] On alloys that are very strong

Cr_2O_3 formers such as 310 s.s.,[30] In. 738[30] and Ni–50Cr[28], the surface oxide dispersions produced no compositional change of the scale since the scales developed on these alloys are Cr_2O_3 even without the addition of the reactive element oxides. The surface coats result in a thinner Cr_2O_3 scale which is more adherent. Furthermore, compared to the untreated Ni-50Cr, the CeO_2-applied specimens exhibited a scale with an oxide grain size about a factor of two smaller. There was also a smaller Cr-depletion zone and less protrusion of the scale into the alloy with fewer voids detected in the underlying alloy and at the scale/alloy interface[28].

The bulk of the applied cerium oxide studied by Tyzack *et al.*[25] and Ecer *et al.*[28] was found to remain at the outer surface of the scale after oxidation. However, some of the particles could also be found at the scale/alloy interface and some within the scale using optical and SEM microscopy.[28] The ceria or silica sol-gel coatings were found to be incorporated within the scale, being located primarily within the outer spinel layer. In all cases, the oxidation or development of the chromia layer seems to occur beneath the applied surface coats. The work of Landkof *et al.*[30] was the only one which reported a complete disappearance of the applied Y_2O_3 after 15 minutes of oxidation at 1000°C. Again, this Auger analysis must have been probed on an area with extremely low Y_2O_3 content since the presence of the applied yttrium oxide on the scale outer surface was evident both in SEM micrographs and in EDX analysis even after much longer than 15 min. of oxidation at the same temperature.

When comparing the relative effectiveness of these surface applied oxides to alloying additions, Ecer *et al.*[28] reported a final weight gain after 20 hours at 1000°C to be twice as high when the cerium is present as a surface oxide dispersion on Ni-50Cr as when it was alloyed. Furthermore, the effects of these surface additions seem temporal. When the oxidizing condition is more severe with temperatures at 1000°C or higher, the scales usually begin to show spallation with a consequent increase in the oxidation rate after no more than 150 hours .[8],[28],[30] The only exception is the CVD deposited silica coating ($\sim$ 4 μm thick) on the 20/25/Nb steel which lasted 1000 hours at 1000°C. Generally, when the oxidizing temperature is lower than 900°C, the coatings lasted much longer before deteriorating. Bennett *et al.*[29] reported a 5000 hours life time at 900°C

with their ceria or silica coatings and Tyzack *et al.*[25] reported 1000-2000 hours with CeO_2 applied via hot dipping in nitrate solutions.

All of the alloy systems studied thus far are Cr_2O_3 formers; that is, a continuous external Cr_2O_3 scale is formed, whether beneath a layer of base metal oxides or mixed spinels, under the oxidation environment even without the presence of the reactive element oxide additions. The only exception is the type 304 s.s. whose chromium content makes it a borderline Cr_2O_3 former at 1000°C in air. This alloy oxidizes under such conditions to a spinel layer which consists mainly of Fe and Cr with some Mn. The application of yttrium, cerium or lanthanum oxides on the alloy surface prior to oxidation changed the scale composition to a single layer of Cr_2O_3 containing only minor amounts of Fe.[30] Nevertheless, this effect was only observed when there was Si present in the 304 s.s. Model alloys having the same composition as the 304 s.s. except without the 1 wt% Si showed no improved oxidation behavior with the surface Y_2O_3 dispersion. Furthermore, a model type 304 s.s. with the Si but without the 2 wt% Mn present showed an even higher degree of protection when treated with the surface applied Y_2O_3.[30] No explanations were given for these observations.

At present, the mechanisms involved in producing the beneficial effects by these surface oxide dispersions are still unclear. Some investigators[28],[30] believed that the deposited oxides act as preferential nucleation sites on the alloy surfaces as proposed by Stringer *et al.*[2] with alloying additions, thus causing the earlier development of the Cr_2O_3 scale. The reduced scale growth rate was explained by Ecer *et al.*[28] as due to the blocking of anionic transport in the scale. The incorporation of CeO_2 particles into the scale allows the adsorption of Ce ions to oxide grain boundaries, which in turn is proposed to block grain boundary diffusion of the anions. The reduction of anion mobility reduces the compressive stresses in the scale resulting in less buckling and thus better scale adhesion. Bennett *et al.*[29] on the other hand suggested that the reduction in growth rate arises from the formation of a thin barrier film which effectively impedes cation and oxidant movement. The film that resulted from a silica sol-gel coating was identified as α-quartz, but a corresponding layer was not found with the ceria sol-gel coatings. It was suggested that the

improved oxide adherence from the sol-gel ceria coatings resulted from their incorporation within the oxide scale, modifying the scale properties to reduce thermal strains which are a result of thermal cycling and are responsible for spallation.

2.3.2 Ion-implantation

Ion-implantation is a process which can modify the surface and near-surface properties of a material without affecting its bulk. The technique has been successfully used in many practical applications for improving wear resistance of engineering components.[86] During the last decade, an increasing number of corrosion studies have been undertaken using various ions implanted into metals and alloys. The role of ion-implantation in high temperature oxidation has been recently reviewed by several authors.[87]–[90] In this subsection, only the results from works concerning the influence of implanted reactive elements on the high temperature oxidation behavior of heat-resistant alloys will be considered. First, a general description of the ion implantation process is given.

Implantation Process

Ion-implantation is a non-equilibrium process that produces metastable systems having remarkable stabilities. The procedure involves the bombardment of a metal surface in a moderate vacuum with a beam of the chosen elemental ions, accelerated in an electric field to energies up to a few hundred kilo electron volts. The target metal surface temperature is normally only slightly above ambient. The ions penetrate into the surface layers of the metal coming to rest in a continuous, approximately Gaussian, distribution, about a mean range. Statistical fluctuations in the energy loss process determine the width of the distribution. Its form can be calculated with reasonable accuracy using the LSS approximation.[91] Since the penetration is achieved entirely by a high kinetic energy rather than diffusion, the mean range of implanted ions is short, typically 0.1 μm.

The associated radiation induced damage of the metal arising from the ion bombardment will form a highly disordered region to a depth somewhat greater than the range of the implanted ions. This, together with the presence of the additional implanted atoms will generate

considerable stress within the implanted region. However, the radiation induced damage can be reduced or eliminated by annealing the metal at temperatures at which vacancy assisted self diffusion becomes possible, so that the defects created by the irradiation recombine or disperse.

Another physical effect of ion implantation is the accompanying collisional mechanism resulting in sputtering. The sputtering process often produces marked surface structure on the target[92] which can give rise to a higher effective reaction surface area that leads to an increase in oxide nucleation sites in oxidation. Furthermore, preferential sputtering of one particular species in an alloy target may occur depending on the binding energy of the atoms. For example, Ni or Co has been found to sputter three or four times faster than Cr.[93] In a binary alloy of Ni-Cr or Co-Cr, this could then lead to an alloy surface enrichment of Cr.

Effect on Fe-Cr-Ni and Ni-Cr Alloys Forming Cr_2O_3 Protective Scale

Among this group of Cr_2O_3-forming alloys, Ni-20Cr,[15],[18],[21] Ni-33Cr,[13] Fe–43Ni–27Cr[13] and a 20Cr/25Ni/niobium stabilized (20/25/Nb) austenitic stainless steel[9],[11],[12],[17],[22]–[24] were used as the base alloys for the implantation studies. The 20/25/Nb steel was oxidized in CO_2 at 700, 800 and 850°C for up to a maximum of 7157 hours. The other alloys were tested in O_2 at 800–1000°C for no more than 80 hours. The implanted species showed little influence at 800 or 900°C as compared to that at 1000°C,[18] but for the steel at the lower temperature range (700–850°C), similar effects were often observed regardless of the temperature variation.

The nominal implantation doses usually range between 10^{14} and 10^{18} ions/cm^2. By calculation, 1x10^{15}/cm^2 of yttrium implanted at 400 keV corresponds to a maximum ion concentration of 0.17 at% at a depth of 0.15 μm. Neglecting any material loss due to sputtering, an increase in dosage by an order of magnitude results in a parallel increase in maximum ion concentration. The implantation depth remains the same with fixed implanting ion, target and implantation voltage. Implanted yttrium was found to be present primarily in an oxidized state up to 100-500 nm from the surface but as metal at greater depths.[22] Varying the voltage during the implantation process can give a much more uniform distribution of the dopant within the implanted region. Nevertheless, whether the dopant profile has a uniform or a near-Gaussian distribution within the surface

region does not affect its effectiveness in subsequent oxidations.[9] Furthermore, the effectiveness of implanted species does not seem to be a function of the implantation depth. Voltages ranging from 50 keV[13] to 410 keV[9] have been used which produced an ion range of about 0.01 μm to 0.2 μm. At either end of the range, the implanted reactive element was found to be equally effective.

The effectiveness of the implanted reactive elements did not result from the physical effects associated with the implantation process. This was demonstrated by studying the effects produced by implanting similar dosages of either an inert element such as Kr[9] or Ar,[13] or a principal constituent of the alloy such as Cr in Ni–20Cr[15] or Nb[9] or Ni[14] in 20/25/Nb steel.

Yttrium has been the most widely studied dopant. It has been found to markedly decrease the oxidation rate and improve the scale adhesion on all of the Cr_2O_3-forming alloys studied. The extent of protection was similar to that from yttrium alloy additions, at least within the reported testing conditions. On Ni–Cr[13],[15],[18] and Fe–Ni–Cr[13] alloys the implanted yttrium also decreased the time necessary for the establishment of a continuous Cr_2O_3 scale, which in turn prevented completely or partially the formation of an outer NiO or spinel layer. The Cr_2O_3 grain size was smaller on the yttrium implanted than the unimplanted alloys. TEM studies[21] also showed fewer voids present within the Cr_2O_3 layer formed on implanted Ni-20Cr after 15 min. at 1000°C. On the 20/25/Nb steel,[14],[22] the implanted yttrium brought no significant compositional changes in the resulting oxide scale. Normally, the scale consists of an outer (Fe, Mn, Ni) spinel layer, an inner Cr_2O_3 layer and a thin silica band at the oxide/steel interface. Effects of the implanted yttrium were to eliminate or reduce the concentration of Ni and Fe in the spinel layer, and to reduce the thickness and grain size of the chromia layer.

Other reactive elements have also been studied.[12],[14]–[18],[22],[23] Cerium is as effective as yttrium, producing apparently the same effects. A dosage dependence was observed using Y and Ce. Piven *et al.*[13] reported an increasing effectiveness of yttrium from a dosage of $2x10^{14}/cm^2$ to $9x10^{15}/cm^2$. The higher dose resulted in a greater reduction in oxidation rate and was able to prevent any base metal oxide formation. Similarly, Bennett *et al.*[14] found that above thresholds of between $5x10^{14}$ and $5x10^{15}$ yttrium and between $5x10^{15}$ and 10^{16} cerium ions/cm^2 the implanta-

tion of both elements was effective in reducing the oxidation rate and improving the scale adhesion. Higher doses progressively increased the induction period before the start of spallation, as well as its subsequent extent. The highest dose, 10^{17} Ce or Y/cm^2, completely inhibited spallation for at least 3331 hours of oxidation in the case of Ce and 7157 hours in the case of Y. In their earlier studies[9],[11] the implanted yttrium was found to be less effective or not effective at all when compared with 0.13-0.41 wt% of yttrium alloying addition. The implanted specimens usually resumed normal oxidation behavior after a limited period of oxidation. This duration of effectiveness was shorter at higher oxidation temperatures. Since the implanted dose used then was only $3x10^{15}$ ions/cm^2, in light of the dosage effect later established,[14] it becomes clear why those yttrium implants were not very effective.

Although yttrium and cerium proved to be very effective dopants, implanted calcium, silicon, scandium and aluminum on Ni–20Cr[18] were found to be less protective. The kinetics for the silicon, scandium and aluminum implanted surfaces were even irreproducible, with slow rates of weight gain after the transition stage being followed by breakaway type behavior. On 20/25/Nb steel, Bennett *et al.*[23] found similar beneficial influences from the implantation of La, Eu and Yb as from Y and Ce, but negligible effects with Pt, Al, Si[12] or Sc[23] implants. Alloying additions of Al and Si[94] have been shown to markedly improve scale adhesion of Ni-20Cr alloy; oxide dispersions of Al_2O_3[44],[45] in Ni-20Cr were also found to be effective. It is not known why some of the surface implanted species were very effective while some others were not. In the case of Sc, Bennett *et al.*[23] suggested that it is because Sc_2O_3 forms a range of solid solutions with Cr_2O_3, the Sc cannot form discrete oxide particles within the scale to block the grain boundary diffusion which leads to scale growth.

The distribution of the implanted reactive element after oxidation has been a great concern for at least two reasons. First of all, since the reactive elements have high affinity for oxygen, they will be oxidized as soon as oxidation starts, thus showing negligible diffusion throughout the oxidation process. This enables them to act as an internal marker which allows the determination of the scale growth direction . Secondly, knowing the exact location and chemical state of the reac-

tive elements in the complex oxide scale may help to understand the mechanism involved for their effectiveness.

On Ni-Cr and Fe-Ni-Cr alloys forming the protective Cr_2O_3 scales, an earlier investigation[13] used secondary ion mass spectrometry (SIMS) to evaluate the distribution of yttrium in the scale. In most analyses the yttrium peak was found to have maintained its general Gaussian shape. However, the location of the peak maximum was not accurately determined, since the yttrium profile varied from specimen to specimen, and even from grain to grain without a clear reason. Therefore, a general conclusion was that the yttrium was distributed throughout the Cr_2O_3 layer, which was at least 100 times thicker than the average implantation depth. Later work[18],[21] studied the scale formed on Ni-20Cr alloy using analytical electron microscopy, and was able to show more precisely where the yttrium was concentrated. After only 15 minutes at 1000°C, yttrium was found throughout the Cr_2O_3 layer. No yttrium containing phases could be detected, so it was concluded to be in solid solution in the scale and in the alloy.[21] After a longer period of oxidation, 24 hours at 1000°C, the yttrium became incorporated entirely in the Cr_2O_3 scale. However, the yttrium was not distributed uniformly nor was it concentrated at the scale/metal interface or on the oxide grain boundaries. Regions enriched in yttrium were detected within grains and at grain boundaries, while in other regions the yttrium content was below the detection limit of the instrument. The yttrium-enriched regions were found to be located towards the outside of the Cr_2O_3 scale only, and the yttrium was present either as Y_2O_3 or possibly $YCrO_4$ or $YCrO_3$.[18]

The fact that those species (Ce, Y and La) which could provide an oxidation resistance were concentrated near the outside of the Cr_2O_3 scale has been further established by Bennett *et al* using SIMS,[9] EPMA[12],[14] and STEM.[23],[24] In contrast, Al and Si which did not show any beneficial effects, were found to be concentrated within the SiO_2 layer which formed between the Cr_2O_3 scale and the alloy on the 20/25/Nb steel.[12] A more recent study[23] on the implanted 20/25/Nb steel indicated that although yttrium was concentrated at the outer part of the Cr_2O_3 layer, it was also present at the Cr_2O_3-silica interface (i.e. the inner part of the Cr_2O_3 layer). Successive analyses established that the former was part of a continuous band, whereas yttrium was

only present non-uniformly at the latter location. The chemical state of cerium is undoubtedly CeO_2,[14] but which form the yttrium is present in the scale is not as clear. It was suggested[23] that Y is present as discrete Y_2O_3 grains about 0.1 μm in diameter, located at triple points within equiaxed Mn, Fe spinel grains which is a layer formed immediately outside the Cr_2O_3 layer on the 20/25/Nb steel. Lathanum on the other hand was detected within these Fe, Mn spinel grains, possibly in solid solution since no La_2O_3 particles could be found.

As it is evident from these experimental results that the implanted species concentrate at the outer part of the Cr_2O_3 scale, indicating a change in the scale growth direction, many questions still remain before the mechanism behind the reactive element effects can be elucidated. In particular, the spacial distribution of the implanted species needs to be established, that is to verify whether they were uniformly present within the grains,[24] preferentially segregated at triple points,[23] or found as clusters within the Cr_2O_3 scales[18] as suggested by previous investigotors.

Effect on MCrAl Alloys Forming Al_2O_3 Protective Scale

There has been less research carried out on effects of ion-implanted species on Al_2O_3-forming alloys than on Cr_2O_3-forming alloys. Earlier works[9]–[12] were concerned with implanting aluminum bcause a substantial aluminum content (4-5 wt%) is required to yield protective alpha-Al_2O_3 films. Increasing the near-surface aluminum concentration by ion-implantation was found[10] to reduce the oxidation rate of a low Al-bearing alloy, Fe-24Cr-1.5Al-0.09Y, which oxidized in air at 1100°C to a scale whose principal constituent was an (Fe,Mn,Cr) spinel containing some Al_2O_3. Increased aluminum ion doses provided a reservoir of aluminum close to the alloy surface which resulted in the formation of an increasingly protective oxide film richer in Al_2O_3. On the other hand, aluminum implantation into alloys which normally form the Al_2O_3 protective scale showed no influence upon the oxidation behavior of these alloys, even with an implantation dose as high as 10^{17}ions/cm^2.[11]

Among the reactive elements, yttrium was the one predominately used for the studies. No clear understanding of the effects of the implanted yttrium on the scale growth rate has emerged. The implantation of 9×10^{15} Y ions/cm^2 was found[13] to have no influence on the oxidation rate of

an Fe-41Ni-25Cr-10Al alloy at 1000°C during 20 h exposure. However, Sprague *et al.*[16] found that implantation of $2x10^{16}$ Y/cm^2 caused a factor of two increase in the oxidation rate of Co-22Cr-11Al at 700°C.

The major established effect of yttrium implantation is in improving the spalling resistance of the protective Al_2O_3 oxide scale. Regardless of its shallow implantation depth, the implanted yttrium improved the cyclic oxidation resistance of a Ni-20Cr-2Al alloy oxidized at 1100°C in air for as long as 560 hours.[19] Nevertheless, during long term oxidation tests, it was found that the Y-implanted specimens did not have the same degree of protection as those with yttrium present within the alloy. For example, Bennett *et al.*[12] has shown that while the oxide scales formed on a yttrium-bearing alloy remained adherent throughout 3271 h exposure at 850°C, the effectiveness of the scale formed on the yttrium-implanted alloy broke down after 784 h.

CHAPTER THREE

Experimental Procedure

3.1 Alloy Preparation

The three binary alloys used in this study were prepared from high purity elements by induction melting and casting under an argon atmosphere. The alloy ingots were cleaned by machining off the outer surface layers and then were homogenized by annealing in evacuated, sealed quartz tubes for 24 hours at 1100°C. The grain size of the Co-Cr alloys ranged from 260 to 1040 μm and the grains had an equiaxed structure free from inclusions. The grains of the Ni-Cr alloy had an elongated structure perpendicular to the casting walls. Average grain width was $\sim$ 460 μm, and a few small Cr_2O_3 particles were found randomly distributed in the alloy.

A ternary alloy with the nominal composition Co-25wt%Cr-1wt%Y was also made in order to compare the effects of Y in the bulk alloy to those of Y applied to the surface. A small portion of the homogenized Co-25Cr ingot was cut and placed with 99.9% pure Y chips in an alumina crucible and melted in an arc furnace under a reduced Ar atmosphere. The melting and solidification of the ingot was repeated three times in the arc furnace in order to achieve good mixing of the components. The resulting ingot was a 25 x 25 x 19 mm square block. After machining off the outer layer of the ingot, it was again homogenized at 1100°C in vacuum for 24 hours. X-ray diffraction analysis of this alloy did not show any Y containing compounds except near edges of the ingot, where Y_2O_3 was present due to internal oxidation of the Y. Observation under the optical microscope showed that the Y concentrated at grain boundaries. The alloy grains were slightly elongated with a relatively uniform grain size. The average grain width was 28 μm and the average grain length was 61 μm. These grains were much smaller than those of the Co-25Cr alloy. Chemical compositions of all the alloys studied are given in Table 1.

Specimens approximately 10 x 15 x 1 mm were cut from the center of the homogenized blocks, and a 2.2 mm diameter hole was drilled on one of the faces. All surfaces were polished to a 600-grit SiC finish and cleaned with alcohol before testing.

3.2 Salt Deposition of Reactive Element Oxides

Deposition of the nitrate salts was carried out by a "hot spraying" method. The specimens were first oxidized at 400°C in air for half an hour to increase the surface wettability. 10 wt% nitrate solutions adjusted with HNO_3 to pH=2 were then sprayed onto the two main faces of the specimen using a commercial air brush while keeping the specimen at approximately 200°C. Immediately following their deposition, the applied nitrate salts were heated in air at 400°C for another hour to decompose them to oxides. The resulting oxides stayed dry on the specimen surface except for CaO which easily absorbed water from the atmosphere. This absorbed water was quickly removed during heating of the specimen in the subsequent oxidation experiment. However, as a consequence of the wetting effect, these specimens usually had a much higher concentration of CaO near the bottom, leaving a thin film of the deposited oxide on the rest of the surface.

The chemical and physical characteristics of the coatings have been examined to some degree. The oxides were shown by X-ray diffraction to be CaO, CeO_2, Y_2O_3, La_2O_3, HfO_2 and ZrO_2. Macroscopic uniformity was usually achieved with the spraying technique. Nevertheless, distribution of the oxides on a microscopic scale varied significantly. Typically, the thickness of the deposited oxide coats was between 2-4 μm. Surface topographies of the various nitrate converted oxides are shown in Figure 2. The La, Y and Ca oxides are seen to have a crystalline structure which is more or less continuous across the entire specimen surface. The Ce, Hf, and Zr oxides on the other hand, show a dense but cracked structure. The cracks presumably developed from the drying, and flakes of oxides were easily detached form the substrate, especially from substrates coated with HfO_2. The deposited nitrates of all the elements before decomposition showed the same morphology as their corresponding oxides.

Much thinner coatings of CeO_2, ZrO_2 and HfO_2 could be obtained by placing a normally coated specimen in an ultrasonic bath of ethanol and washing off the excess applied oxides. This procedure usually removes most of the deposited ZrO_2 or HfO_2 and reveals a clean alloy surface. However, a uniformly thin coverage of CeO_2 remained on the CeO_2-treated specimen. The morphology of this thin CeO_2 deposit is shown in Figure 3.

3.3 Ion-implantation of Reactive Elements

The ion-implantation was carried out in the injector portion of the heavy ion linear accelerator (superHILAC) at LBL. The ions formed in the injector were subsequently focused onto the targets.

The injector uses PIC (Penning Ion Gauge) type ion sources. A plasma of an inert carrier gas, usually Ar or Xe, is formed in the cylindrical arc chamber with the aid of a magnetic field provided by the source magnet. A small strip of the solid source material (e.g. Y) is placed so that arc ions will bombard it, thus releasing ions from the solid to the plasma column. Ions are then extracted through a slit in the side of the arc cylinder through a potential drop of about 20 keV. The acceleration voltage of the ions was usually adjusted to 400 keV. Focusing of the beam is accomplished by means of several sets of quadrupoles. The beam is also analyzed by the magnetic field to select the desired mass and charge stage of the ions. Sources of La^{2+} ,Y^{+} and Xe^{+} have been used and average beam current density was 3 $\mu A/cm^2$. A simplified schematic of the system is illustrated in Figure 4. The vacuum in the beam line and the target chamber was typically between 10^{-6} and 10^{-7} torr.

Specimens used for the ion-implantation were disc-shaped with a diameter of 15 mm and a thickness of 1 mm. Each specimen was polished to a 600-grid surface finish and carefully degreased immediately before the implantation. Individual specimens were held in an aluminum seat which covered 5 mm of the periphery of the specimen to give each specimen an implanted area next to an unimplanted area for later comparison of oxidation behaviors. The specimen-aluminum seat assembly was then put on a specimen holder which can be introduced into the beam line. A schematic of the specimen holder assembly is shown in Figure 5.

The specimen holders sit on two identical and parallel shafts (for simplicity, only one is drawn in Figure 5) on which a total of eight specimens can be mounted. The specimens are placed in the target chamber in vacuum via the flange. The ion beam comes through the collimator onto any specimen which is appropriately aligned on the shaft. The shaft can also be rotated 180° to allow implantation on both faces of the specimens. The desired dosage is a known function of the

total amount of beam current to which the specimen is exposed. Since the specimen holder is insulated from the shaft, direct reading of this current can be obtained via the electrical connections. The actual dosage on the implanted face should however be less than that indicated by the total current because emission of secondary electrons from the specimen surface is not suppressed nor accounted for. Later experimental measurement of the implanted dosage on selected specimens using the Rutherford backscattering (RBS) technique showed that the error was about 50%. In this thesis, a "dosage" is always referred to the value obtained from the total current, unless it is stated otherwise. It should be borne in mind that the actual dosage is only approximately half of this value.

Dosages used in this study varied from 10^{15} to 10^{18} ions/cm^2. From the Lindhard, Scharff and Schiott[91] theory, the depth distribution of the ions can be calculated. The calculated maximum concentration and depth, together with the depth of the implanted zone are detailed in Table 2. Results obtained from selected specimens probed by backscattering with 2 MeV He ions are also presented. The theoretical calculation and experimental results agreed well only on the implantation depth. As mentioned earlier, the actual dosage is always lower than anticipated. The maximum atomic concentration of the Gaussian distribution is also less than calculated.

Spatial distribution of the ions on the implanted surface is not very uniform since the ion beam could not be rastered across the specimen surface. Usually, the beam was defocused to a circular or oval shape which covered an area of approximately 10 cm^2 in order to achieve better uniformity. Nevertheless, the beam intensity was highest at the center of the beam (Figure 6). The variation in implanted dosage from edge to center was found to be a factor of 4 on this particular specimen.

The HILAC implanted carbon along with the interested element from the ion source. Figure 7 shows an Auger depth profile of a Co-25Cr alloy implanted with 1x10^{18}Y$^+$/cm^2. A very distinguishable carbon profile is present within the implanted range. Because of the low atomic weight of carbon, most carbon atoms were introduced closer to the surface than most yttrium atoms. This carbon contamination probably resulted from an inadequate vacuum in the beam line.

Some implanted specimens were annealed to remove radiation damage. The annealing was carried out in quartz tubes sealed under $\sim 1x10^{-6}$ Torr vacuum at 700°C for 5 hours.

3.4 Internal Oxidation Pretreatment

Internal oxidation of some ion-implanted Co-25Cr specimens was carried out prior to the normal oxidation experiment in order to convert the Y present in the alloy to Y_2O_3. Specimens of the untreated Co-25Cr alloy and of the Co-25Cr-1Y alloy were always included during this pretreatment in order to make possible comparisons of their subsequent oxidation behaviors.

Equal weights of a Cr/Cr_2O_3 powder mixture was used to establish a P_{O_2} which is high enough to oxidize the Y internally but not high enough to oxidize the Cr or the Co in the alloy. The powder mixture and the specimens were put in separate arms of a dumbell-shaped quartz tube to avoid contact of the powders with the specimen surfaces. The quartz tube was then sealed under $\sim 1x10^{-6}$ torr vacuum. All internal oxidation runs were carried out at 1000°C to minimize oxygen diffusion through the quartz.

The ion-implanted specimens to be internally oxidized were pretreated for only 2 hours. Since it is not desirable to clean these specimen surfaces by subsequent polishing, precautions were made to minimize any possible containmination from the quartz by placing both the powder mixture and the specimens in separate alumina boats. Studies[95] had indicated that transition metals can react with vitreous quartz at high temperatures and liberate SiO gas which can deposit on the specimen surfaces. Implanted areas on the specimens usually showed a slight coloration after the pretreatment, but non-implanted areas showed no significant difference. These specimens were only cleaned by washing in an ultrasonic bath of ethanol before the subsequent oxidation experiment.

When the internal oxidation pretreatment time was 100 hours, which involved only the untreated Co-25Cr and the Co-25Cr-1Y alloys, the powders and the specimens were placed directly in the quartz tube without the alumina boats. These specimens usually had a very thin film of Si-rich oxide present on the surface after the internal oxidation pretreatment. This film

was easily removed by slight polishing using 600 grid SiC paper. The side of the dumbell which contained the Cr/Cr_2O_3 powder mixtures was found to be badly cracked upon cooling, indicating some reaction had taken place between the powders and the quartz.

Characterization of the internal oxidation pretreated specimens using Auger and SIMS will be described in section 5.1.4 where the effects due to the internal oxidation pretreatment are presented.

3.5 Oxidation

Oxidation tests were carried out in pure, dry oxygen at 1 atm. total pressure. A Cahn 2000 microbalance was used for kinetics measurements at 1000°C. The apparatus which contains the microbalance has been described in detail elsewhere.[96] Specimens were loaded into the apparatus and equilibrated with oxygen before the furnace was turned on. The heating rate of the quartz lamp radiation furnace was high enough to achieve a stable specimen temperature of 1000°C in 10 minutes. After the desired oxidation time, the furnace was turned off and specimens were cooled in O_2 to room temperature in $\sim$ 30 minutes during which time the weight lost due to any spallation could be measured on the microbalance. Duplicate oxidation runs were made in a horizontal tube furnace. In this system, the temperature was first allowed to stabilize at 1000°C while the reaction tube was equilibrated with oxygen. Specimens, either hung from a holder or contained in alumina crucibles, could then be pushed into the hot zone to start the oxidation reaction. The process of introducing the specimens into the hot zone usually takes $\sim$ 5 minutes to prevent cracking of the alumina holder. At the end of each reaction or each thermal cycle (20 hours per cycle), the specimen holder was pulled out of the furnace and specimens were allowed to cool in crucibles covered with lids at room temperature in air. Experimental results obtained from the two furnace systems consistently agreed well. A few experiments were also carried out in the horizontal tube furnace at 1100°C in order to compare the relative behavior at a higher temperature.

3.6 Scale Characterization

Analyses of the oxidized specimens involved initial observations of the oxide top surfaces

under a scanning electron microscope equipped with an energy dispersive X-ray (EDX) analyzer, and the oxides on selected specimens were determined by X-ray diffraction (XRD). Subsequently, these specimens were mounted and polished for cross section observations using both an optical microscope and the EDX equipped SEM. Occasionally, some of the coated specimens were imaged under the SEM using backscattered electrons in order to visualize the location and distribution of the applied reactive element oxides in the scale. The resolution and sensitivity of this technique is however too low to detect any reactive element containing compounds on ion-implanted specimens.

Some thin coatings, as well as some oxide scales were studied using a Physical Electronics Model 590 Scanning Auger Microprobe (SAM) and UTJ Secondary Ion Mass Spectrometer (SIMS). SIMS depth analysis was used especially to determine the distribution of the implanted reactive element in the oxide scale. Although this technique is extremely nonquantitative, the high sensitivity which allows the detection of even 10 ppm of Y in the scale makes it a very useful tool. SIMS depth profiles of the oxide scale formed on salt-treated Ni-25Cr alloys were also done from both the top side and the underside of the scale to better determine the distribution of the applied reactive element oxides after oxidation.

The undersides of the oxide formed on Ni-25Cr previously treated with the reactive elements were examined by first supporting the thin oxide with paraffin wax or epoxy, followed by deep etching away the underlying metal using 10 vol% Br_2 in methanol. It was necessary to have the wax or epoxy support, otherwise the oxides shattered after the metal had been etched away. Fracture cross sections of these scales were then made by breaking the scale along with the wax or epoxy supports. Fracture cross sections of scales formed on Co-15Cr alloys were made by mechanically breaking the scales from the metal. This procedure was possible since the scales formed on this alloy were quite thick and fractured at the alloy-scale interface.

3.7 Marker Experiments

Marker experiments using Engelhard liquid platinum were carried out on Ni-25Cr reactive-element-oxide-treated alloys in order to distinguish the growth direction of the oxide scale. The

results of marker experiments are not necessarily unambiguous, but they, together with supplementary data from the distribution of the deposited reactive element oxides in the oxide scale, can give a clear view of the growth direction.

The Pt was applied in two ways. One method was to apply the liquid Pt in three strips onto the Ni-25Cr alloy surface at room temperature, followed by the usual reactive element oxide deposition at 400°C. The second method was to apply a thin layer of the reactive element oxides on the alloy surface, then apply the liquid Pt strips onto the deposited oxide layer at room temperature. The liquid base easily wets and penetrates the thin surface oxide coats. After drying of the liquid base containing the Pt, these treated specimens were oxidized in the usual manner.

CHAPTER FOUR

The Effect of Surface-Applied RE and REO on Non-Cr_2O_3 Forming Alloys: Co-15Cr, Co-25Cr

In this chapter, the oxidation behavior of salt-coated and ion-implanted Co-15Cr and Co-25Cr alloys are discussed in comparison to the untreated alloys and alloys with bulk additions of the reactive elements or their oxides. The influence due to surface deposited salts on both alloys will be discussed first. Ion-implantation work concentrated on the Co-25Cr alloy, since preliminary studies had shown that implantation of reactive elements in the Co-15Cr alloy gave no observable effects on its subsequent oxidation behavior.

4.1 Results

4.1.1 Salt Deposition on Co-15Cr Alloy

The weight gain vs. time curves for Co-15Cr and the same alloy coated with three different amounts of Y_2O_3 oxidized at 1000°C are shown in Figure 8. The Y_2O_3 addition on the alloy surface had essentially no effect on the oxidation kinetics. Results of oxidation tests with all the different surface oxide coats carried out in the horizontal tube furnace are summarized in Table 3. The weight gain data lay within a scatter band of 5%, and it is seen that none of the applied oxides showed an influence on the oxidation rate.

The uncoated Co-15Cr alloy oxidized to its typical two-layer oxide morphology with an outer columnar CoO layer and an inner layer consisting of CoO, Cr_2O_3 and $CoCr_2O_4$.[97],[98] The same morphology was observed for the surface-coated specimens. Figure 9 compares the fracture cross section of the scales formed on an uncoated and an HfO_2-coated specimens. The backscattered electron image clearly indicates that Hf concentrates at the inner/outer scale interface. The presence of the applied REO at the same location was also observed with scales formed on a Y_2O_3-coated specimen using EDX line scan.

Although the externally-applied REO seemed to show no influence on the overall oxidation

kinetics or the scale morphology of the Co-15Cr alloy, their presence did affect the oxidation during the initial 1-2 hours of exposure. The kinetics for the uncoated specimen were parabolic starting from the beginning of oxidation. The Y_2O_3-coated specimen on the other hand, shows a negative deviation from parabolic behavior during the first hours. Presumably, this is due to the fact that the presence of the Y_2O_3 on the surface reduces oxygen/metal contact initially until the coating breaks down. SEM top surface image (Figure 10) of a Y_2O_3-coated specimen oxidized for only 24 minutes illustrates this limited blocking behavior. Figure 10(a) shows the nonuniform distribution of Y_2O_3 on the surface after the short oxidation time, and provides an understanding of the sequences involved during initial oxide growth on the coated surfaces. In the area shown on the left hand side of Fig.10(a), the denser Y_2O_3 prevented most CoO growth, while in area a, fast growing CoO grains began to develop through areas of the coat which might have had less Y_2O_3 present. Finally, continued outward and lateral growth of the CoO grains eventually covers all the applied Y_2O_3 in areas that probably had the least Y_2O_3 present, as indicated by area b.

4.1.2 Salt Deposition on Co-25Cr

Kinetics

The effects of the surface applied oxides on the oxidation rate of the Co-25Cr alloy is very sensitive to the total coverage of the applied salt. Figure 11 shows the rate curves for specimens coated with increasing amounts of La_2O_3, and Table 4 summarizes the final weight gain and oxide spallation of the tested specimens. It is possible that La_2O_3 only has an effect on the oxidation rate and scale adhesion when the surface coverage reaches a certain value. After this coverage has been achieved, heavier coatings offer no further improvement. Similar behavior was also observed with CeO_2-coated specimens. Examination of the specimen surface with SEM revealed that even with the thinnest coating, La_2O_3 particles were found covering the entire specimen surface. However, an apparently continuous dense La_2O_3 cover was not developed until the application was heavier. When the coat became too heavy, deep cracks were often found, and this could account for the faster initial oxidation rate observed with the most heavily coated specimen.

The effects of all the surface oxides deposited to a similar thickness on the oxidation rate of this alloy are compared in Figure 12. An HfO_2 coating is seen to increase the oxidation rate, showing a breakaway type of oxidation behavior after the initial five hours. However, the oxidation rate recovered after about 25 hours, and subsequent weight gain of the HfO_2-treated specimens was only slightly less than that of the untreated. Heavier coats of HfO_2 gave rise to a larger final weight gain and a longer breakaway period. A Cr_2O_3 coating is seen to initially reduce the oxidation rate to a very low level. However, this period ended after 1-2 hours of oxidation and the subsequent weight gain of the specimen was only slightly influenced by the presence of the initially deposited Cr_2O_3 coat. Heavier Cr_2O_3 deposits showed a tendency to prolong the initial slow growth period, but again showed no effect on the overall long-term oxidation kinetics. The rest of the surface-coated oxides reduce the oxidation rate to different degrees with Ca being the most effective, and Y and La better than Ce and Zr. Those surface coated with Y, La and Ca oxides were also significantly more resistant to spallation as shown in Table 5, and it is noted that the more beneficial surface coats are those oxides that deposit to form the dense, non-flaky morphologies. (Fig. 2)

At the higher oxidation temperature (1100°C, see Table 6), CaO increased the oxidation rate. This increased rate is due to the formation of a low-temperature eutectic between CaO and Cr_2O_3 at 1022°C.[99] The resulting scale was very adherent, probably as a result of the presence of minor amounts of a liquid phase in the scale at temperature. In general, the surface-applied reactive element oxides became less effective at the higher temperature. This trend is opposite to that observed with bulk additions of the reactive elements or their oxides.[1]

Scale Morphologies

The oxidized Co-25Cr alloy developed a duplex structure similar to that observed on the Co-15Cr alloy, but the scale/alloy interface was extremely ragged (Fig. 13a). Along the interface, there is a thin (2-6 μm), discontinuous Cr_2O_3 layer as shown on the magnified scale in Figure 13(b). This layer was usually more complete in thinner scale regions, where the scale consisted of mainly a $CoCr_2O_4$ spinel layer above the Cr_2O_3 and a CoO layer decorated with Co_3O_4 at the

scale/gas interface. This kind of structure, shown in Figure 13(c), is similar to that observed by Wright and Wood[98] on a Co-30Cr alloy. The fraction of surface covered by these Cr-rich protective scales was very low on specimens oxidized for longer times (i.e. 24 hours, as the scale shown in Fig. 13a), but was much higher on specimens oxidized for only 3 hours as shown in Figure 13(d).

The HfO_2-treated specimens (Fig. 14a) showed an overall increase in scale thickness. The scale was found everywhere to be duplex with only limited regions with the Cr_2O_3 healing layer after 24 hours of oxidation, but after 50 hours, some occasional thin, noncontinuous areas with a Cr_2O_3 layer at the scale/alloy interface similar to that observed on the untreated alloy could be found. In contrast, the ZrO_2 or CeO_2 treated specimens had an overall scale thickness less than that of the untreated but with a very similar scale structure, as shown in Figure 14(b). The originally applied HfO_2, ZrO_2 or CeO_2 remained as the oxides after oxidation as indicated by X-ray diffraction. Most of them were found near the inner/outer scale interface while some scattered within the outer CoO layer.

After oxidation, the only detectable La or Y containing compounds in the scales formed on La_2O_3 or Y_2O_3 treated specimens using XRD were $LaCrO_3$ and $YCrO_3$ respectively. Localized chromium-rich regions were found randomly scattered on the oxide surface as shown in Figure 15(a) near area p. These regions were also very rich in La or Y and were locally promoted Cr_2O_3 scales. Other areas on these oxidized specimens showed oxide morphologies similar to the untreated alloy, except that the Cr-rich protective scale found occasionally on the untreated specimens was now more abundant and the Co-rich duplex scale was generally thinner (Fig. 15b). With longer oxidation time (i.e. 50 hours), more Co-rich duplex structures were found at the expense of the Cr-rich protective scales and the very localized Cr_2O_3 scales. La or Y were found concentrated near the inner/outer scale interface when the scale developed a duplex structure.

Scales formed on the CaO-treated specimens resembled those found on La_2O_3 or Y_2O_3 treated ones, except that the scales were almost entirely the Cr-rich protective type. Only occasionally, the Co-rich duplex scale was found. Figure 16(a) shows the structure of the Cr-rich protective scale. This structure and that of the scale on the untreated specimen, shown in Fig. 13(b),

appeared identical in morphology and thickness. Ca concentrated in the spinel layer right beneath the outer CoO layer, and deposited CaO was found after the oxidation to have reacted to form $CaCrO_4$. The CaO-treated specimens also showed a higher percentage of the locally promoted Cr_2O_3 scales. Near the bottom of the specimen, where coverage had been the thickest due to the wetting effect of the CaO, the bulk of the scale was found to be purely Cr_2O_3. Figure 17 shows the morphology of this scale and the distribution of components. Ca is now seen to concentrate on the scale/gas interface where the presence of some 30 at% Co was also detected.

4.1.3 Ion-implantation on Co-25Cr Alloy

Kinetics

On all of the implanted specimens, there was an appreciable amount of surface area that was shielded from the ion beam and therefore was not implanted. The oxidation kinetics of the implanted surface must be corrected from the knowledge of the implanted area (A_1), the unimplanted area (A_2) and a comparison of the weight change of the implanted specimen to the unimplanted specimens oxidized under the same condition. Thus

$$w_2 = \frac{\Delta w - w' A_1}{A_2}$$

Where: w_2 = weight gain per unit area due to the implanted surface
Δw = total weight gain from the implanted specimen
w' = average weight gain per unit area from the unimplanted specimen.

Figure 18 shows a plot of w_2 as a function of time for various ion-implanted Co-25Cr alloy oxidized under 1 atm. O_2 at 1000°C. Annealing of the implanted specimens generally did not alter the oxidation kinetics. Also on Figure 18 is presented the oxidation kinetics of the unimplanted Co-25Cr alloy and the yttrium containing Co-25Cr-1Y alloy for comparisons. Perfect parabolic behavior was observed for the Co-25Cr-1Y and the Co-25Cr($1x10^{18}$ Y^+/cm^2) specimens after the initial five hours of oxidation. The others showed a near parabolic behavior after about 8 hours. Approximate parabolic rate constants were determined using $(\Delta m/A)^2 = f(t)$ linear plots. The constants are given in Table 7 where spallation behavior of these specimens are also described. From these results, a very strong dosage dependence was obvious. When the implanted Y^+ dosage

was as high as $1x10^{18}$ atoms/cm^2 (peak concentration equals 20-25 at%), the growth rate became significantly reduced and the resulting scale was very adherent. However, this slow growth behavior was only temporary. After longer oxidation times the weight gain began to increase as shown in Figure 19 and the scale again spalled upon cooling. Annealing this high dosage specimen did not have any effect on subsequent oxidation behavior or on the adherence of the scale formed. Other implanted specimens showed progressively less effect in reducing the growth rate with less implanted dosages. Furthermore, the scales formed on these implanted surfaces spalled more easily than that formed on the unimplanted surfaces. An example is shown in Figure 20. Annealing of these specimens did not alter the oxide growth behavior, but eliminated the excess spallation tendency associated with the implantation. Specimens implanted with lanthanum or yttrium ions showed similar oxidation behavior, except that the lanthanum ions caused a faster initial weight gain of the specimen, which may be related to the higher degree of radiation damage produced by the heavier lanthanum ions.

Scale Morphology and Composition

The scales formed on the unimplanted Co-25Cr alloy under these oxidizing conditions are described in section 4.1.2 and the scale morphology is shown in Figure 13. Typical scale morphology developed on the Co-25Cr-1Y alloy after 24 hours at 1000°C is shown in Figure 21. The scale consisted of a complete inner layer of Cr_2O_3 and an outer layer of CoO mixed with Co_3O_4. Yttrium was internally oxidized at the front of the scale/alloy interface. Small particles were found on alloy grain boundaries where the added yttrium had segregated before oxidation. The penetration depth of the internal oxidation zone was in general 5 times larger than the scale thickness.

With implantation dosages less than 10^{18}/cm^2, whether using La^{2+} or Y^+ as the source, the scales formed showed little difference from that of an unimplanted specimen. There was generally a higher percentage of the Cr-rich protective scale on the implanted surfaces. This percentage increased with increasing implantation dosage. Figure 22 shows the scale formed on the Co-25Cr($1x10^{16}$ Y^+) specimen. The thin protective scale as shown in Figure 22(a) had a healing Cr_2O_3

layer at the scale/alloy interface between 2 and 6 μm thick. This type of structure consisted of approximately 50% of the scale formed on the implanted surfaces. Other areas developed the Co-rich duplex scale as shown in Fig. 22(b) and (c). The thickness of these duplex scales varied quite noticeably. Some had a thin Cr_2O_3 healing layer near the alloy, some did not. The scale developed on the more highly implanted specimen ($3x10^{17}$ Y^+) is shown in Figure 23. The scale was almost entirely the thin Cr-rich protective type with varying thickness as shown in Fig. 23(a). The Cr_2O_3 healing layer was found to be nearly continuous along the scale/metal interface, except for a few locations where the Co-rich duplex nodules were found. One of these large nodules is shown in Fig. 23(b). Also shown on Fig. 23(b) are small fragments of what appears to be single layered Cr_2O_3 scale. Indeed, SEM observation of scale top surfaces varified that on very rare and localized areas the oxide formed was only Cr_2O_3. Occasionally, this Cr_2O_3 layer could also be found beneath some Co-containing oxides as shown in Fig. 23(c).

The scale morphology on the most heavily implanted Co-25Cr alloy (1×10^{18} Y^+) after 24 hours of oxidation is shown in Figure 24. The unimplanted area showed the usual Co-rich oxide grains and large areas of spallation. The implanted side developed a very fine grained Cr_2O_3 scale, confirmed by XRD, with an average grain size < 150 nm which contained ~ 12 at% Y as detected using EDX. Most of the Y was present as Y_2O_3 after 4 hours of oxidation. Some had reacted to form $YCrO_3$, but the amount of this was comparatively small, as indicated by the relative intensities of YO^+ and $YCrO^+$ peaks in SIMS. With continued oxidation (after 24 hours) most of the Y was probably present as the chromite since XRD of the scale scraped off the implanted surface showed faint lines corresponding to $YCrO_3$ only, not Y_2O_3. The Co content observed with EDX was primarily due to substrate contribution since only very little CoO phase was observed using XRD. Numerous individual Cr_2O_3 grains and Cr_2O_3 clusters can be seen growing out of the fine grained oxide. The Cr_2O_3 clusters grew along the original 600 grid scratch marks on the specimen surface. Cracks were often found in these Cr_2O_3 clusters and occasional spallation of them was observed. Examination of these spalled areas usually showed a number of pores near the scale/alloy interface. Figure 25 shows a 40 degree tapered cross-section of the scale. Comparison

between scales formed near the unimplanted/implanted interface showed a dramatic difference between the scale morphologies. On the implanted side, the scale is seen to be single layered with occasional small nodules. The thin oxide has an approximate average thickness of 1.5 μm. BSE imaging (Fig. 25b and c) indicated that the Y is present near the scale/gas interface. Many individual Cr_2O_3 grains extending from the scale can be seen delineated within the alloy matrix. Large internal oxides of Cr_2O_3 were also abundant ahead of the scale.

In order to obtain a distribution profile of the Y in the scale, SIMS depth profiling was used and the result is shown in Figure 26. The analysis was obtained from a 1x1 rastered area sputtered with high purity Ar. The sputtering rate was approximately 0.025 μm/min. Intensities of Cr, Y and Co were measured at different intervals. Occasionally, the rastering mechanism was turned off for a very short period so that the intensities due to the center of the SIMS crater could be obtained. This method corrects for much of the cratering effect which leads to extended tailing. The curves drawn on Figure 26 were corrected by this method. Form the sputtering rate, the scale is calculated to be 1.4 μm thick. Y is no longer concentrated near the first 0.1 μm from the surface as in the case of the unoxidized specimen, but peaked about 0.5 μm away from the scale/gas interface. The scale formed behind the Y peak contained mainly Cr, but before the Y peak, an appreciable amount of Co was detected.

When specimens with this high dosage were oxidized for only 4 hours at 1000°C, extremely fine-grained oxide could be found on localized areas on the specimen surface. One of these areas is shown on the lower left hand side of Figure 27(a). Again, along the 600 grid polish marks, Cr_2O_3 grains can be seen growing out of areas of this fine-grained scale. Occasionally, large nodular growth was also detected, as indicated by the three nodules shown in the figure. Figure 27(b) is a BSE image using Auger electrons. Areas that appeared brighter were richer in Y and they were closely associated with the extremely fine grained areas. SAM O, Y, Cr and Co mapping of this area also shows that the Y-rich region is totally free of cobalt but heavily associated with oxygen. Figure 27(c) and (d) are Auger depth profiles of points 1 and 2 marked on Figure 27(b) respectively. The relatively high noise of the Auger peaks were due to charging of the oxide scale. It is

seen that the very fine oxides were thin Cr_2O_3 layers with a Y profile unchanged from that of the unoxidized specimen, indicating that the growth of this thin scale was totally due to oxygen inward diffusion. The scale thickness is between 0.3 and 0.4 μm which is about three times that of the original implantation depth. On the other hand, the profile on pt. 2 showed an inward shift of Y as a consequence of the outward transport of Cr and Co through the originally-developed thin scale, and a scale more than twice as thick as that found in pt. 1 was observed. The scale composition detected at point 2 is very similar to the SIMS profile reported on scales formed after 24 hours of oxidation.

As indicated by kinetics studies, after oxidation longer than 24 hours the protective scale formed on the $1x10^{18}$ Y^+ implanted specimen started to break down. Figure 28(a) shows the implanted/unimplanted interface of the Co-25Cr ($1x10^{18}$ Y^+) specimen oxidized for 50 hours. The scales formed on the implanted area now appeared similar to that on the unimplanted side and a great deal of spallation occurred. However, occasionally, small areas with the protective fine-grained Cr_2O_3 scale could still be found on the specimen surface mixed with large CoO grains as seen in Figure 28(b).

4.1.4 Internal Oxidation of Co-25Cr(Y^+) and Co-25Cr-1Y

The internal oxidation (I.O.) treatment was an attempt to convert the implanted yttrium to its oxide since bulk alloying of the reactive element oxides had been found to be more effective in promoting Cr_2O_3 scale formation than wer the corresponding elements.[34] Implanted Co-25Cr alloy specimens with two different dosages ($1x10^{16}$, $3x10^{17}$) of Y^+ were internally oxidized. Coupons of Co-25Cr and Co-25Cr-1Y alloys were treated simultaneously with the implanted Co-25Cr so that subsequent oxidation behavior of the untreated Co-25Cr alloy would serve as a base-line figure for the comparison of the effect of the implantation; likewise, the oxidation of the I.O. pretreated Co-25Cr-1Y could be used as a comparison of effects of alloying addition to those of surface implantations.

Characterization of Internal Oxidation Treated Specimens

Characterization of the specimens after the internal oxidation pretreatment was carried out using Auger analysis and SIMS. Figure 29(a) shows the surface composition of the implanted surface before internal oxidation treatment. The usual surface contaminants such as O, C, Cl, S, Ca and N were present. After a 15 second sputtering with an approximate sputtering rate of 2500 nm/min (removing a total of $\sim$ 6250 nm), most of the surface contaminants were removed as seen in Figure 29(b). Some O was still found present and there was also a relatively large carbon signal. The high carbon signal was not a surprise since characterization of the implantation process using AES depth profiling had shown that carbon was implanted with the Y^+. The small Ar peak in Fig. 29(b) came from the sputtering source which in this case is Ar. No yttrium was detected. Figure 30(a) shows the AES survey of the implanted surface after the 2 hour I.O. pretreatment at 1000°C. Comparing Figure 29(a) and 30(a), it is seen that the I.O.-treatment did not introduce a large amount of contaminants on the specimen surface except some extra Si which presumably came from the quartz tube the specimens were sealed in. Si is an unique element for AES analysis because elemental Si and Si bonded in SiO_2 show characteristic Auger peaks at different kinetic energies. The Si observed here corresponded to Si associated with SiO_2. Not only was this Si present on the surface, it was also found penetrated into the alloy during the I.O. pretreatment. In Figure 30(b), an even more pronounced Si signal was present after all the other surface contaminants were eliminated by the removal of about 1250 nm from the surface. Also in Figure 30(b), a large O peak was present as a consequence of the oxygen inward diffusion. Much less carbon was found within the implantation zone, probably due to oxidation by the oxygen. More Y was found here than in the as-implanted surface. This could be either due to an outward diffusion of the Y as a result of the I.O. treatment, or due to the surface nonhomogeneity of the implantation process: that is, the point analyzed here had a higher Y content from the implantation process. It is also noted from comparing Figures 29(b) and 30(b) that a higher Cr/Co ratio was found on the I.O.-treated specimen indicating a transfer of Cr from the Cr/Cr_2O_3 pack, which had higher Cr activity than the base alloy.

Continuous SIMS depth profiles of Y^+, YO^+, and O^- were determined on the implanted sur-

faces before and after the I.O. pretreatment. The purpose for analyzing the YO^+ signal was to be sure that the implanted yttrium had indeed been oxidized as a result of the I.O. process. Figure 31 shows the depth profiles obtained using a 2500 nm/min Ar sputtering source. Before the internal oxidation, both O^- and YO^+ were only present on the very surface of the specimen most likely due to oxidation of the surface Y from the atmosphere. After the internal oxidation, both of these profiles extended into the alloy with the YO^+ profile closely resembling that of Y^+. Some diffusion of the Y^+ had occurred as indicated by the spreading of the Y^+ peak after I.O. However, due to the very nonquantitative nature of the SIMS technique, no meaningful estimates of diffusion coefficients could be obtained.

Cross sections of Co-25Cr-1Y alloys after the two internal oxidation pretreatment times (i.e. 2 hours and 100 hours) were observed using an optical microscope. The depths of the internal oxidation zone on these two specimens were approximately 15 μm and 60 μm respectively, which compares well with those calculated from oxygen diffusivities.[34] Most internal oxides were found along alloy grain boundaries where the initially alloyed Y was concentrated.

Kinetics and Scale Morphology

The effect of the internal oxidation treatment on the oxidation kinetics of Co-25Cr, Co-25Cr-1Y and Co-25Cr($3x10^{17}$ Y^+) alloys is shown in Figure 32. Parabolic rate constants obtained from the usual $(\Delta m/A)^2$ vs. time plots are given in Table 8. These results indicated that the internal oxidation treatment did not affect significantly the subsequent oxidation behavior of the implanted Co-25Cr alloy. This is true regardless of the implantation dosage. With the higher dosage implanted specimen, the oxidation rate was only reduced during the first hour of oxidation as shown in Figure 33(a). After approximately 50 minutes, fast growth began and subsequent kinetics behavior resembled that of the non-I.O.-treated specimen. The resulting scales also showed no improved adhesion. If one assumes that the initially formed, slow grown scale was fully dense Cr_2O_3 with a density of 5.21 g/cm^3,[100] after 50 minutes the scale would be 0.2 μm thick which is comparable to the $\sim$ 0.17 μm implantation depth of this specimen. Indeed, the oxide scale formed on the implanted, I.O.-treated specimen after 30 minutes of oxidation was found to

be very fine-grained ($< 0.07\ \mu m$) Cr_2O_3 enriched with Y as shown in Figure 33(b). Larger-grained Cr_2O_3 islands were also observed scattered randomly and growing out of the fine-grained scale surface. At this stage, the scales formed was very adherent compared to that on the unimplanted surfaces. However, metallographic observation of the scales formed after 24 hours of oxidation showed no apparent morphological differences between the I.O.-treated and the untreated Co-25Cr($3x10^{17}$ Y^+) specimens.

The internal oxidation treatment on the Co-25Cr-1Y was found to reduce the initial stage of oxidation as seen in Figure 32. Prefect parabolic behavior was observed after less than two hours. The growth rate of the scale after the initial oxidation was unaltered from that of the uninternally oxidized Co-25Cr-1Y alloy. Specimens treated with longer I.O. times which had a deeper I.O. zone did not show any difference in the subsequent oxidation behavior from those treated with the shorter I.O. time. Figure 34 shows the typical scale developed on the I.O.-treated specimen after 24 hours at 1000°C. Cr and Co maps using EDX showed that the scale contained mainly a complete layer of Cr_2O_3 above which is a very thin layer of CoO at the scale/gas interface. A large Y_2O_3 internally oxidized zone ahead of the scale was also observed. Occasionally areas with scales resembling that found on the non I.O.-treated Co-25Cr-1Y could be found, and these scale had a much pronounced outer Co rich layer above the Cr_2O_3 scale. None of the scales formed on the Co-25Cr-1Y alloys whether I.O.-treated or not spalled upon cooling.

The oxidation behavior of Co-25Cr after undergoing the I.O. treatment is also presented in Figure 32. Although the partial pressure of oxygen in the quartz tube encapsule was not high enough to cause any internal oxidation, the pretreatment which at least involved the penetration of oxygen and Si into the alloy and the deposition of Cr on the alloy surface altered the subsequent oxidation behavior of this alloy quite noticeably. Furthermore, the effects were different with different I.O. pretreatment times. The Co-25Cr alloy I.O.-treated for 2 hours showed a perfect parabolic behavior after the first 8 hours of oxidation. The 100 hour treated one showed a slight, continuously positive deviation from parabolic behavior. The approximate k_p is recorded in Table 8.

More than half of the scale formed on the Co-25Cr alloys (I.O.-treated or not) spalled upon cooling. Metallographic observation of the remaining scales showed no significant difference in scale morphology. Like those formed on the untreated Co-25Cr alloy, The scales formed can be Co-rich duplexed or Cr-rich protective as described in section 4.1.2. The specimen which had undergone 2 hours of I.O. showed a much higher percentage of the Cr-rich type scale on its surface while the specimen with 100 hours of I.O. had almost everywhere this Cr-rich type scale on the surface.

4.2 Discussion

4.2.1 Oxidation of the Untreated Co-25Cr

Although the oxidation of the Co-Cr binary system has been studied by numerous authors[35],[97],[98],[101]–[107] and the composition Co-25wt%Cr has been particularly studied by Kofstad and Hed,[35] it is still necessary to briefly discuss the oxidation behavior of the Co-25Cr alloy used in this study. This is because the composition of this alloy makes it a borderline Cr_2O_3 former and its oxidation behavior usually is not very reproducible but depends greatly on the purity of the alloy.[108] The parabolic rate constant obtained from the Co-25Cr alloy used in this study was lower than that found by Kofstad and Hed,[35] or by Wright and Wood;[98] however, the discrepancy is no greater than a factor of 10.

The oxidation kinetics normally show three stages (refer to the kinetics curve in Figure 12). The first stage is the transient stage where all nuclei grow until a thin duplex scale is established with an outer CoO layer and a inner $Cr_2O_3/CoO/CoCr_2O_4$ mixed layer. Underneath the duplex structure is a thin Cr_2O_3 healing layer. However, this layer is never continuously present on the specimen surface. The first stage usually takes only 1-2 hours, after which, a slow growth second stage follows. This stage involves mainly the growth of the thin healing layer of Cr_2O_3. Nevertheless, since the coverage of the Cr_2O_3 scale is not complete, the growth rate observed is not as slow as that found with the normal growth rate of Cr_2O_3. This second stage may only last for about an hour before the thin scale breaks down to form a Co-rich duplex scale similar to that observed by other investigators.[35],[98] The initial protective thin scale is probably broken down because the

oxide formed on other regions which did not have the protective Cr_2O_3 healing layer continued to grow rapidly to form the Co-rich structure; lateral growth of these oxides can disrupt the neighboring Cr_2O_3 layer, increasing the area of fast growth regions until all of the initially formed protective scale is distroyed.

Previous studies[35],[98] have suggested that the growth of the steady-state Co-rich scales is controlled by the diffusion of Co^{2+} ions through the few interconnecting CoO paths in the very spinel-rich inner layer. Furthermore, it was demonstrated[35] that the oxidation behavior of this alloy is sensitively dependent upon the oxygen pressure. At 1000°C, for example, rapid oxidation at 760 Torr oxygen pressure led to the formation of a Co-rich duplex scale, but an order of magnitude reduction in the rate occurred at 100 Torr pressure where the scale is a continuous layer of Cr_2O_3. Such behavior was also observed for the Co-25Cr alloy used in this study. When the partial pressure of oxygen was kept between 10 and 30 Torr with a total gas pressure of 1 atm., a continuous Cr_2O_3 scale was promoted at 1000°C. However, this scale was very nonadherent. In Figure 35(a), it is seen that more than half of the scale spalled upon cooling. The spalled area, 35(b), showed numerous interfacial pores and areas with no scale/alloy contact. The remaining unspalled scale as seen in Fig. 35(c) and (d) is single layered Cr_2O_3 with a very convoluted morphology, suggesting little scale/metal contact.

After an 'internal oxidation' pretreatment, the oxidation rate of this alloy was slightly reduced. A higher degree of reduction was found with longer pretreatment time. Both of the I.O.-treated alloys (after 2 hours. or 100 hours.) had a higher degree of the thin protective scale on the surface than the untreated. This accounted for the reduction in growth rate. Jones and Stringer[108] have shown that the oxidation behavior of this alloy is particular sensitive to impurities, especially Si associated with O. Their results demonstrated that as little as 0.05 wt% Si can promote protective oxidation of Co-25wt%Cr provided the alloy has a sufficient oxygen content. The Si present as a dispersion of SiO_2 probably acted as nucleation sites to facilitate the development of a continuous Cr_2O_3 scale. Since the I.O. pretreatment was carried out in a quartz tube using Cr/Cr_2O_3 mixed powders to establish the P_{O_2}, its effect on the Co-25Cr alloy was found to

(i) introduce oxygen into a certain depth into the alloy in solid solution, (ii) to deposit some chromium on the alloy surface and (iii) to introduce Si into the alloy (present as SiO_2) along with the oxygen. More Si with deeper penetration was introduced into the alloy with longer I.O. pre-treatment times. This factor and the enrichment of the surface region of the alloy with Cr both can contribute to the observed reduction in oxidation rate by forming a higher area fraction covered with the protective scale on the specimen surface.

4.2.2 Influence of Surface-Deposited Oxide Coats

None of the surface-applied reactive element oxides showed any significant influenes on the oxidation behavior of the Co-15Cr alloy. The scale formed had its usual duplex morphology with the applied oxides concentrated at the inner/outer scale interface which in many cases, particularly with dilute alloys of this kind, corresponds to the original specimen surface.[35],[98] The inability of the surface oxides to promote a continuous Cr_2O_3 scale will be discussed in a later section.

The surface-coated Co-25Cr alloys usually exhibit a variety of oxidation behavior over each specimen. Therefore, it is important to regard the recorded oxidation rate as an integration of all the local processes taking place over the entire specimen surface. The morphology of the scale developed with the different oxide-treated specimens can be characterized into two groups: those that developed with the flaky, "mud-cracked" oxide coatings (i.e. Hf, Ce and Zr), and those with denser coatings like La, Y and Ca. The oxide scale developed on the specimens with the flaky coatings show the typical duplex morphology of the uncoated alloy, and these scales spall upon cooling. With the denser coatings, the scales formed usually have several morphologies varying from area to area: they can either have the Co-rich duplex structure, or the Cr-rich protective type, or can be singly layered Cr_2O_3. These scales usually spall much less upon cooling. All the duplex layer structures have the deposited reactive elements concentrated at the inner/outer scale interface, while they are located at the scale outer surface on the single layer Cr_2O_3 scales.

These experimental results suggest that the influence of the surface oxide coats is strongly dependent on the morphology of the applied oxide layer. This idea is supported by the effect of decreased amount of applied La_2O_3 on the specimen surface. Smaller amounts of the La_2O_3 result

in a less uniform coverage on the surface. The scale adhesion is not improved and the overall oxidation rate is not significantly changed. Higher resolution observation of the deposit indicates that even for this thinner deposit the surface is actually completely covered with La_2O_3. It is therefore evident that the La_2O_3 has to be present as a continuous layer of dense oxide for it to show any beneficial effect on this alloy.

Since the oxidation behavior of this alloy is sensitively dependent upon the oxygen partial pressure, it is reasonable to conclude that the primary effect of the surface deposited oxides was to act as a barrier layer. Initially, when the deposited layer was dense enough, as on parts of the surfaces of the CaO, La_2O_3 and Y_2O_3 coated specimens, Cr_2O_3 was formed beneath the applied oxide. This fact would suggest that the applied coating decreased oxidant ingress, consequently reducing the oxygen potential beneath the coating to a sufficiently low value to promote the Cr_2O_3 formation. Subsequently, the surface La_2O_3, Y_2O_3 or CaO reacted with the Cr_2O_3 to form the corresponding chromite or chromate, which can act as a more effective diffusion barrier to allow the continued growth of the Cr_2O_3 layer. Diffusion studies[109] have shown that chromium diffuses 40 times slower in $LaCrO_3$ than in Cr_2O_3. The ability of the deposited surface oxides to react to form a chromite or chromate seems essential in stabilizing the Cr_2O_3 scale. Very thick applications of the flaky type of oxides (CeO_2, ZrO_2 and HfO_2) can also initially induce Cr_2O_3 formation, but since they do not react with the Cr_2O_3 to form chromites, the scale soon cracked and flaked to give way to normal duplex oxide formation. Regions on the La_2O_3, Y_2O_3 or CaO treated specimens which have thinner coatings that were not able to reduce the oxygen partial pressure sufficiently to promote Cr_2O_3 growth exhibited slow unaffected normal growth, developing a duplex oxide scale rich in Co. As growth of this Co-rich oxide continues outwardly and laterally, the thin Cr_2O_3 layer associated with thicker coatings could be disrupted and become embedded in the growing oxide. As a consequence, the fraction of the surface covered with the locally-promoted Cr_2O_3 scales diminishes with increasing oxidation time.

After cracking and flaking, the initially deposited ZrO_2, CeO_2 or HfO_2 oxides became embedded in the growing duplex scale, concentrated at the inner/outer scale interface. Their presence

there also has a slight effect in reducing the oxidation rate, possibly by reducing the effective diffusion area through the scale. The HfO_2 flakes behaved like the CeO_2 or the ZrO_2 for the first five hours of oxidation, forming a slightly Cr enriched scale with HfO_2 embedded in it. However, the most easily detached HfO_2 flakes probably caused the scale to crack after this initial period, exposing the underlying Cr-depleted alloy and giving rise to the considerable increase in the oxidation rate. Eventually, the oxidation resumes its normal behavior with a slightly reduced rate.

Several investigators[39],[40],[51],[68] working with bulk alloying additions of the reactive elements or their oxides have suggested that an REO accumulates in one form or another in the oxide scale or in the alloy ahead of the oxide and acts as a diffusion barrier to the diffusing species and therefore reduces the oxidation rate. However, such a hypothesis is questionable[2] since relatively small additions of an REO in the alloy can produce significant reductions in the oxidation rate, more than can be expected from the reduction in cross-sectional diffusion area. For surface added oxide coats, the situation may be different. First of all, the surface oxides have to be present in a significant amount before reduction of growth rate can be observed. Secondly, these oxides are applied as 2-4 μm thick continuous coats. Even if they are broken up by the growth of the scale, they are still present in an appreciable amount in the scale and may act as an effective barrier layer.

Bennett *et al.*[29] suggested that a chemical vapor deposited silica layer acts as a diffusion barrier when deposited on a preoxidized steel surface. An effect on corrosion rate becomes apparent with 2 μm thick coatings and progressively increases with increasing coating thickness up to $\sim$ 10 μm. The beneficial effect of thinly-applied ceria coatings using the sol-gel method was also explained by a possible barrier-film formation.[29] However, direct identification or observation of such a film was not reported. Rehn[110] observed a complete layer of spinel to form on chromate-treated stainless steel tubes between the inner and outer scale interface after the chromate treatment. This spinel layer then apparently acts as a barrier layer and reduces oxide growth rate by a factor of 3-4.

One interesting difference between the barrier behavior of these examples and that of the

nitrate-converted oxides on the Co-25Cr alloy lies in the intrinsic oxidation behavior of this alloy. Initially, the deposited oxides act as a physical barrier between the oxidant and the alloy, promoting locally Cr_2O_3-rich regions. Subsequently, after being embedded into the growing scale, they become a diffusion barrier similar to those found in the earlier studies.[29],[110]

4.2.3 Influence of Ion-Implanted Reactive Elements

The oxidation behavior of the Co-25Cr alloy after Y^+ ion-implantation showed a strong dosage dependence. With an implantation dosage between 10^{16}- 10^{17} ions/cm^2 which corresponds to a peak concentration of 2-7 at%, the oxidation rate was reduced by a factor of 3-5. However, in no cases did the scale develop a continuous layer of protective Cr_2O_3 like that induced by the alloying addition of Y in Co-25Cr-1Y. The oxidation rate of the bulk alloyed Co-25Cr-1Y was nearly 17 times lower than that of the Co-25Cr alloy.

These implanted specimens usually show a fast initial growth rate, sometimes even faster than that of the untreated alloy. Reduced steady state growth is normally not observed until after about 2 hours of oxidation, by which time the weight gain of the specimen is already $\sim$ 1.2 mg/cm^2 which corresponds to metal removal far beyond the initial implantation depth, which if the scale formed is a mixture of CoO, Cr_2O_3 and some spinel is of < 0.2 μm. All of the implanted species is then incorporated in this initially developed scale.

Metallographic observation of the scales formed on these implanted specimens showed that the scales are usually thinner than scales formed without implantation, with a more complete Cr_2O_3 healing layer at the scale/alloy interface. The area fraction of this Cr_2O_3 layer increases with higher implantation dosage. It seems probable then that the effect of yttrium incorporated in the oxide scale is to retard Co^{2+} outward transport. The resultant reduction in rate of CoO formation would facilitate the development of the slower-growing but thermodynamically more stable Cr_2O_3 layer at the scale/alloy interface.

The mechanism by which the Y_2O_3 particles retard Co^{2+} transport requires more detailed studies. Since all of the implanted species is concentrated in a relative narrow layer of $\sim$ 0.2 μm thickness in the scale, it is possible that the thin yttrium-modified layer may act as a barrier; this

layer becomes more effective as the implanted dosage increases. Alternatively Y_2O_3 particles may be concentrated at dislocations or grain boundaries in the scale and retard the transport of the diffusing species by these short-circuit diffusion paths.

Internal oxidation pretreatment of the $3x10^{17}$ Y^+/cm^2 implanted specimen, converting the yttrium to its oxide prior to oxidation, did affect the oxidation behavior in the very initial stage. A very fine grained, continuous Cr_2O_3 scale developed on the surface. Nevertheless, this layer soon broke down after its thickness has exceeded the implantation depth. Similarly, the Co-25Cr($1x10^{18}$ Y^+/cm^2) implanted specimens also developed a continuous but unstable Cr_2O_3 scale. This scale lasted longer and grew to a thickness at least 5 times that of the implantation depth before breaking down. The development of this Cr_2O_3 scale was observed using SAM and SIMS. Initially, an extremely fine-grained Cr_2O_3 layer formed. The fact that Y was present at the oxide/gas interface suggests that this thin Cr_2O_3 scale was grown inwardly. Subsequent growth however, involves the outward diffusion of Cr and Co through the thin yttrium-rich layer ($\sim$ 0.3 μm in thickness). The scale at this stage is still mainly Cr_2O_3 until the fast growing CoO finally disrupts it. The instability of the Cr_2O_3 scales formed on these implanted surfaces is discussed in the next section.

4.2.4 The Inability of Surface Additions of RE or REO to promote Cr_2O_3 Scale

One important effect of minor alloying additions of reactive elements or their oxides on Cr_2O_3-forming alloys is to reduce the Cr level in the alloy necessary to form a continuous Cr_2O_3 protective scale. For this purpose, a dispersion of the reactive element oxide is found to be generally much more effective than the corresponding reactive elements in the alloy. For the Co-Cr system, protective Cr_2O_3 can be formed on alloys containing as low as 10 wt% Cr with 1 wt% Hf, Ti or Zr internally oxidized prior to the oxidation.[34] Stringer and Wright[32] observed formation of a continuous Cr_2O_3 layer on Co-21wt%Cr with 3 vol% Y_2O_3 addition, and Wright *et al.*[111] also reported similar observations on a Co-13wt%Cr-3vol%Y_2O_3 alloy. In all cases, the dispersoid particles, whether mechanically added or interally formed in the alloy, were responsible for the selective oxidation of Cr to form a continuous Cr_2O_3 layer. This Cr_2O_3 layer developed across the

entire specimen surface except at dispersion free areas. Furthermore, there was usually little overgrowth of the base metal oxides. This ability to promote Cr_2O_3 scale formation at lower chromium levels was regarded by Stringer *et al.*[2] as due to the preferential nucleation of oxide at the sites of emergent reactive metal oxides at the metal surface.

The Co-25Cr-1Y alloy tested in this study behaved in accordance with previous observations. Initially, the oxidation was fast with the formation of a CoO-rich scale at the scale/gas interface. During this time, the Y in the alloy is internally oxidized to Y_2O_3 ahead of the scale. These Y_2O_3 particles can act as nucleation sites within the alloy. Wagner[56] has proposed that the transition from internal oxide formation to redevelopment of a continuous external scale should occur when the volume fraction of internal oxide precipitates at the reaction front reaches a critical value. These internal oxide precipitates block inward oxygen diffusion into the alloy thus allowing outward transport of the oxide-forming element (eg. Cr) to result in lateral growth of the oxide to form a complete layer. The effect of the Y_2O_3 particles is by increasing the number of internal oxide nuclei to decrease the amount of lateral growth required and thus promote a continuous stable Cr_2O_3 subscale on an otherwise non-Cr_2O_3 forming Co-25Cr alloy. After the internal oxidation pretreatment, the Y is present as the oxide. The oxide particles emerging to the alloy surface may act as preferential nucleation sites on the onset of oxidation, resulting in a much reduced initial stage: a much thinner outer CoO layer and a earlier development of a continuous Cr_2O_3 scale.

None of the nitrate-converted surface oxides deposited on the Co-15Cr or the Co-25Cr alloy assisted in the development of a continuous Cr_2O_3 scale. Although in the case of the Co-25Cr alloy, La_2O_3, Y_2O_3, and CaO were effective in locally promoting Cr_2O_3 scale formation, the effects were mainly due to the applied surface oxide coats acting as semi-blocking layers.

Landkof *et al.*[30] also studied the effect of these nitrate-converted oxides on the oxidation behavior of a borderline Cr_2O_3 former, namely Type 304 stainless steel (Fe-18Cr-10Ni), at 1000°C. Although the application of a Y_2O_3 coat on the surface in some cases promoted a continuous Cr_2O_3 scale, the effect was strongly related to the presence of Si in the alloy. If there was no Si present, the Y_2O_3 addition was ineffective. The reason for such behavior is not known. However,

their results definitely indicate that the presence of Y_2O_3 on the surface of Type 304 steel, unless Si is present in the alloy, does not promote continuous Cr_2O_3 scale formation.

With ion-implantation of the reactive elements, one finds the development of a more complete Cr_2O_3 healing layer at the scale/alloy interface with higher implantation dosage. Such development of the Cr_2O_3 layer is different from what has been observed with alloying additions of the reactive elements which promote selective oxidation of Cr, in that a continuous Cr_2O_3 layer is established very early and consequently without the development of very much cobalt-containing oxide. Only when the implantation dosage was higher than a nominal $3x10^{17}$ ions/cm^2, which corresponds to an actual dosage of 10^{16}-10^{17} ions/cm^2 as indicated by RBS, was a single layered Cr_2O_3 scale formed like those observed with bulk alloying additions. Other results like those made with alloying additions are the observations that i) oxide dispersions of the reactive elements are more effective in promoting the Cr_2O_3 scale than the reactive elements and ii) the so-formed Cr_2O_3 scale has grain sizes much smaller than those formed on the dispersion free areas. However, significant differences are also apparent: i) much higher concentrations of the reactive elements were needed for the ion-implantation process to induce selective oxidation of Cr and ii) these so-formed Cr_2O_3 scale was not stable and gave way to normal oxide growth after a short period of time. The length of this period is depended upon the implantation dosage. The higher the dose, the longer was the period before normal growth was observed.

The fact that the reactive elements are ineffective in promoting an external Cr_2O_3 scale on the Co-25Cr alloy except when the implantation dosage was as high as 10^{18} ions/cm^2 suggests that the mechanism proposed by Stringer *et al.*[2] is not correct, or at least is not complete. The implanted dosage of $1x10^{18}$/cm^2 produces a peak concentration of about 20 at% which is much higher than the usual alloying additions of the reactive elements, only 1-2 wt%. The formation of a temporarily stable Cr_2O_3 external scale after implantation may have an entirely different origin. One possible explanation is that a high dose of Y essentially modifies the composition of the alloy near its surface, so that the alloy initially behaves as a ternary Co-Cr-Y system with an average Y concentration of approximately 10 at%. This may give rise to the development of a Cr_2O_3 scale

enriched with Y_2O_3. When the scale grows into regions without any Y present, it may become unstable. Subsequently, the oxide scale developed begins to resemble those formed on the Co-25Cr binary alloy. Although the 'nucleation model' may not be enough to explain the enhanced Cr_2O_3 scale formation caused by the additions of the reactive elements, it is not proved entirely incorrect either by the present study. The experimental results can also be explained under the assumption that this model is correct. The following discussions are made with this assumption in mind.

If the reason for the promoted Cr_2O_3 scale is indeed a consequence of the dispersoid particles present in the alloy acting as nucleation sites for the initially-formed oxides, then one would expect the externally applied particles on the surface of the alloy also to nucleate a Cr_2O_3 scale. However, effective service as nucleation sites would only be possible if the externally applied particles are fine, present in high enough concentrations to result in small interparticle spacings, and dispersed rather than formed into a somewhat continuous layer. Present studies indicate that the coatings formed by the nitrate deposition method do not generaly have the required morphology to serve as dispersed nucleation sites. Instead, the applied oxides appear in the form of thin layers on the surface. When the quantity of applied salt was small, localized areas with apparently discrete reactive element oxide particles were present, approximately 0.1-0.2 μm in diameter and spaced on an average of $\sim$ 0.1 μm apart as revealed by SEM micrographs. However, the particles so deposited may be too large to be effective nucleants for an alloy with such a low Cr_2O_3 forming tendency. A previous study[44] using bulk alloying addition of Al_2O_3 demonstrated that coarse and widely separated Al_2O_3 particles were ineffective while a fine and closely spaced Al_2O_3 dispersoid at the same volume fraction showed all the usual beneficial effects of the reactive elements for Ni-20wt%Cr.

The minimum implantation dosage in this study which showed selective oxidation of Cr was (a nominal) $3x10^{17}$ Y^+/cm^2 after the implanted Y had been converted to its oxide. RBS analysis showed that the penetration depth of the implanted specie was $\sim$ 0.16 μm with a maximum concentration of 6.7 at% at approximately 0.076 μm. The average concentration of Y within the implantation depth was therefore 3.5 at%. This amount is more than three times higher than in

the Co-10wt%Cr-1wt%Hf, Ti or Zr systems studied by Whittle *et al.*.[34] It is reasonable to find that a higher concentration of the reactive element oxides is needed to act as nucleation sites for the selective oxidation of Cr when the oxide dispersions are only present within the first 0.2 μm of the surface. Since there is no oxide dispersions beyond the immediate surface region, the initially formed Cr_2O_3 nuclei cannot tolerate any undermining growth of the base metal oxide nuclei. Therefore, a higher concentration and thus a higher density of Cr_2O_3 nuclei are necessary for the development of a continuous protective scale before these individual nuclei are lifted away from the alloy surface by the fast-growing Co oxides.

It is rather surprising, however, that these developed Cr_2O_3 scales failed to grow continuously or to remain protective as one always finds with bulk alloying additions. The scale could not have been broken down chemically by the Cr content at the scale/alloy interface falling below the level where the oxide is thermodynamically stable. Calculations have shown[112] that this level is generaly less than 0.1 at%. Although the actual concentration of Cr at the scale/alloy interface before the scale breakdown was not measured experimentally, it is reasonable to suppose that a drop from 27 at% to 0.1 at % in less than 2 hours at 1000°C is kinetically not possible. It is also unlikely that the scale broke down by cracking or lifting at temperature as often observed on Fe-Cr alloys,[113] since the scale was found to be dense, nonconvoluted, very adherent to the underlying alloy and showed negligible spallation upon cooling.

Examination of the initially formed Cr_2O_3 scale under SEM, SIMS, and SAM indicated that the scale first grew by inward transport of oxygen, giving rise to an extremely fine grained Cr_2O_3 layer which was very adherent. However, subsequent growth involved outward transport of Cr as well as Co through localized areas on the initially formed Cr_2O_3 layer. This process produced clusters of larger-grained oxides which were less adherent, and a number of interfacial voids could be found at the base of these clusters. The continued outward growth of these clusters seemed to be the cause of the final breakdown of the initially promoted Cr_2O_3 layer.

Stringer and Wright[32] reported scale morphologies similar to those described above on a Co-21wt%Cr-3vol%Y_2O_3 alloy. In their study they found two types of scales on the alloy surface:

a thin oxide consisting essentially of Cr_2O_3 grown by inward oxygen transport and a thick oxide (in the form of clusters or nodules) which contained Cr_2O_3 and $CoCr_2O_4$. The thick oxide grew at the oxide-oxygen interface and it spalled upon cooling. The major difference between their Cr_2O_3 scale and that formed on the surface implanted specimen studied here is the stability of the scales. Their scale remained protective for more than 70 hours even at 1200°C while the ones formed with surface implantation lasted less than 30 hours at 1000°C before breakaway oxidation took over.

It is possible that the breakdown of the Cr_2O_3 scale formed on surface implanted alloys was due to a lack of internal oxide dispersions present to act as vacancy sinks.[46],[71] As some parts of the scale begin to grow by outward metal transport, a higher flux of vacancies would accompany the growth. When the alloy was only surface implanted, the reactive element oxide particles had been already incorporated into the scale and were unable to trap the injecting vacancies. As a consequence, vacancies could condense at the interface to generate voids which give rise to weak spots in the oxide and lead to final scale breakdown.

CHAPTER FIVE

The Effect of Surface-Applied REO and RE on a Cr_2O_3 Forming Alloy: Ni-25Cr

The nickel-based binary alloy was chosen to be the model Cr_2O_3 former for easier comparison with previous studies carried out on the REO effects due to bulk alloying additions. However, before these results are presented and discussed in this chapter, the effect of a surface applied oxide coat on a cobalt-based binary Cr_2O_3 former will be briefly mentioned since the non-Cr_2O_3 forming alloys used in this study involved only the Co-Cr binary system.

In Table 9 is shown the effect of a CeO_2 coat on the isothermal oxidation behavior of a Co-40wt%Cr alloy at 1000°C. The CeO_2 coat was chosen because it had negligible effect on the non-Cr_2O_3 forming Co-25Cr alloy under these oxidizing conditions, but it is seen here to be very effective in reducing the oxide growth rate and enhancing the scale adherence. The morphology of the resulting adherent scale was similar to those formed on the Ni-25Cr alloy which will be discussed in detail in this chapter.

5.1 Results

5.1.1 Effect of the Nitrate-Converted Oxide Coats

Kinetics

Kinetics curves for the oxidation at 1000°C of the Ni-25Cr alloy coated with all the oxides studied is shown in Figure 36, and in Table 10 spallation of the oxidized scales upon cooling is recorded. An obvious difference between the effects of these salts on this alloy and on the Co-25Cr alloy is the change in relative effectiveness of Ce and Ca oxide coats. While the applied CeO_2 still has its mud-cracked appearance, it is now as effective as the Y and La oxides. On the other hand, CaO with its usual dense morphology shows a less beneficial effect.

Surface addition of Cr_2O_3 only slightly reduces the oxidation rate found for an untreated alloy (marked - on the Figure). Deposited HfO_2 is again seen to increase the rate as well as the degree of spallation. The large weight increase occurred after the first 6-7 hours of oxidation, after

which the weight gain behavior becomes similar to that of the untreated specimen.

Cyclic oxidation of a cerium oxide-treated and an untreated specimen was carried out at 1000°C in 1 atm O_2 in the horizontal furnace. Results of overall weight gain and the weight loss due to spallation are shown in Figure 37. The presence of CeO_2 on the surface did improve scale adherence under these oxidizing conditions. Similar runs which lasted 300 hours also showed the same degree of protection. Even more impressive is that the applied CeO_2 was no more than 0.2 μm thick. The bulk of the coating had been removed by an ultrasonic wash prior to the cyclic oxidation.

Table 11 shows the isothermal oxidation results at 1100°C. Again, presumably due to the formation of the low-temperature eutectic between CaO and Cr_2O_3, the oxidation rate was enhanced and scale adhesion was improved by the presence of the surface CaO. The effect of the other applied oxides were essentially similar to their effect at 1000°C. Results of cyclic oxidation at 1100°C of CeO_2 and Y_2O_3 coated specimens are presented in Figure 38. A high degree of protection was still present. However, slight spallation usually occurred toward the end of the testing period, with more spallation associated with thinner coatings. There was no significant differences between the two types of salt coating being studied. The rate of weight gain and especially the degree of spallation were both somewhat greater than that obtained with bulk alloying additions (see for example Michels[45]).

Scale Morphology and Composition

The untreated Ni-25Cr alloy oxidized to a single layer Cr_2O_3 scale with some NiO present on the outer surface in the form of nodules. Most of the NiO growth occurred not at the onset of oxidation as with the Ni-20Cr alloy, but developed after a thin layer of Cr_2O_3 scale had formed. The time of appearance and the position on the surface of these fast-growing NiO nodules protruding out of the originally formed Cr_2O_3 scale were quite random. Since the process was a gradual one, breakaway type of kinetics was not observed. Figure 39 shows the typical steady-state scale morphology of the untreated Ni-25Cr. Occasional internal oxide fingers were observed penetrating into the alloy. The CaO and ZrO_2 treated specimens oxidized to develop similar scale

morphologies except that the scale was thinner. In most cases, NiO formation was prevented. The deposited oxides either remained on the outer surface or became embedded in the scale.

Figure 40 shows the scale formed on a HfO_2-treated, oxidized specimen. Unlike the untreated Ni-25Cr, this specimen oxidized to a two layer scale. The top layer consisted of NiO, Cr_2O_3, and some $NiCr_2O_4$ as well as some HfO_2 as indicated by X-ray diffraction, while the inner scale is purely Cr_2O_3. Although in this field, X-ray maps only reveal the large HfO_2 flake on the surface, backscattered electron (BSE) image (Fig. 40e) showed that HfO_2 is actually physically distributed throughout the entire outer scale in relatively large fragments with the original flaky type of morphology.

Kinetics results have shown that the most effective surface-deposited oxides for this alloy were those of La, Y and Ce. The oxide formed was a single layer Cr_2O_3 scale. CeO_2 remained as the oxide, but La_2O_3 and Y_2O_3 reacted to form $LaCrO_3$ and $YCrO_3$ respectively. The morphologies of the scales formed on these specimens were very similar. Figure 41 shows the SEM image and X-ray maps of a typical scale formed on a Y_2O_3-treated specimen. Oxide grains of the Cr_2O_3 scale are clearly delineated within the alloy matrix, and Y seems to be concentrated at the outer surface of the oxide. Occasional nodules of Cr_2O_3 can be seen protruding from the surface, as at A. No internal oxides were found anywhere across the cross-sectioned specimen, and NiO was also not found on top of the Cr_2O_3 scale.

In order to better study the distribution of the originally deposited oxides in this type of structure, the CeO_2-coated specimen was examined using backscattered electrons. Figure 42(a) shows such an image of the scale. Ce appeared lighter under this imaging mode and small CeO_2 particles (0.1-0.15 μm in diameter) were found concentrated along the alloy/gas interface, for example at A. Most of the oxide lay beneath the CeO_2 particles, but occasionally there were also grains growing above the CeO_2, as at B. The small amount of CeO_2 found in the scales shown in Fig. 42(a) were only those particles that had become embedded in the growing scale. Most of the applied CeO_2 remained as a loosely attached layer on the surface of the specimen, and this CeO_2 layer detached during polishing as shown in Figure 42(b). X-ray analysis of the detached CeO_2 in

Figur 42(b) shows only the presence of Ce, indicating that there had not been any interaction between the bulk of the coating and the underlying Cr_2O_3 scale. Similar detachment of Y_2O_3 and La_2O_3 coats were not found since these coats were more adherent to the underlying alloy.

Depth profiling using SIMS was done on a CeO_2-treated specimen oxidized isothermally for 50 hours at 1000°C. Figure 43(a) shows the morphology of the grains at the outer surface of the oxide and Figure 43(b) is the same area imaged using backscattered electrons. Numerous small CeO_2 particles (bright) can be seen to be present on the surface of the scale. Figure 43(c) is the SIMS depth profile of Cr, Ni, and Ce starting from the oxide top surface to the scale/alloy interface. The sputtering rate was approximately 0.1 μm/min and the sputtering area had a Gaussian distribution with a center $\sim$ 100 μm in diameter with a long extended tail. The analysis showed that the scale contains predominantly Cr. A very small amount of Ni is present within the scale. The concentration of Ni is slightly enriched near the outer surface. This higher Ni content near the surface could be due to the small amount of NiO formed upon initial exposure of the specimen to the oxidizing environment. The SIMS measurement showed the Ce to concentrate near the outer surface and to decrease in concentration progressively towards the interface. But due to a large cratering effect of the SIMS and the irregularity of the metal/oxide interface, it is impossible to determine whether the amount of Ce detected near the interface is real or is it due to a contribution from the high surface intensity. Therefore, a similar profile starting from the underside of the scale to its outer surface is necessary. Figure 44(a) shows the morphology of the underside of the scale. The oxide grains are fine and uniform. When viewed using backscattered electrons, very small and brighter particles can be seen on some grains. A few examples of them are indicated by arrows on the micrograph. EDX analysis showed the areas containing these particles to be slightly Ce rich. A continuous SIMS trace of mass 140 from the underside of the scale to the scale top surface is shown in Figure 44(c). The analysis indicates that a small amount of Ce is present near the interface within a very narrow region of only 0.05 μm width. The amount of Ce then quickly drops to a baseline level for the next $\sim$ 0.1 μm of scale, after which the amount of Ce increases slowly towards the outer interface, as expected. A similar trace starting from a thin

piece of unetched metal through the interface to the outer surface failed to detect the slight enrichment of Ce at the interface. This however, could be due to an instrumental limitation; Because of the roughness of the interface, a concentrated Ce signal at the interface may have been smeared out. It is also possible that the slight amount of surface mass 140 peak (Ce) detected on the underside of the scale was due to contaminants. No detectable amount of Ce was found within the metal.

The underside of a ZrO_2-treated Ni-25Cr was also examined. Figure 45 shows the grain morphology which appeared very different from that observed on the CeO_2-treated specimen. Fine grains of oxide appeared in nodules throughout the underside of the scale. Zr-rich particles as indicated by arrows were found randomly distributed on this surface by EDX as well as by BSE imaging.

At 1100°C, the scale morphologies showed no significant changes from those developed at 1000°C. The scale on the Y_2O_3-treated specimen, which was one-seventh the thickness of that on an untreated specimen, contained no Ni and the Y concentrated within the outer part. Successive deep etching of the alloy beneath this scale using Br_2/MeOH revealed oxide grains extending into the metal, as shown in Figure 46, but nothing that resembles the pegging reported in earlier work[46],[49],[60],[74] for alloy addition of reactive elements or their oxides. No Y was detected by EDX near the interfacial area.

Figure 47 compares the fracture cross-section of scales formed on the Y_2O_3-treated and the untreated specimens. The untreated showed a uniform, equiaxed oxide grain structure which seems to be porous. The Y_2O_3-treated on the other hand had very fine grains near the top and underside of the scale, but was very coarse-grained between these layers, with a single grain extending across the intermediate layer. The scale seemed denser and nonporous. Y_2O_3 particles were occasionally found within the coarse-grained layer, but the large majority of them were still concentrated on the outer surface.

Marker Experiment

Liquid platinum was deposited in two different ways as described in the experimental section. Figure 48 shows the oxide scales formed on Y_2O_3-treated specimens with the Pt markers. With the specimen shown in Figure 48(a), Pt was deposited onto the surface-applied thin Y_2O_3 coat. On this specimen, Pt markers were often found lying on top of the Y_2O_3 layer where the coating was thick. However, some Pt which had penetrated through thin regions of the Y_2O_3 coat can be seen under the BSE mode to be located on the outer surface of the scale. When the Pt was deposited between the alloy surface and the Y_2O_3 coat, preventing a direct interaction between the Y_2O_3 particles and the substrate, the resulting scale became much less adherent. This was demonstrated by a high degree of spallation found within the Pt strips. Figure 48(b) shows a piece of unspalled scale with the Pt markers. The markers are again located near the outer surface. However, the scale is slightly thicker than that in (a) and has usually more outwardly grown nodules.

Pt markers were also put on ZrO_2-treated specimens. With these specimens, the smaller markers could be found distributed everywhere within the scale while the larger ones stayed near the scale/metal interface. This kind of distribution is similar to that found on specimens without any reactive element oxide deposits. Therefore, the growth direction of the Cr_2O_3 scale formed on the ZrO_2-treated specimens was probably not changed.

5.1.2 Effects of Ion-Implantation

Kinetics

The implantation process was carried out using the superHILAC facility at LBL as described in the experimental section. Yttrium was chosen from the limited available sources as the reactive element for the study, and a range of yttrium dosage was implanted. Figure 49 shows the weight gain of various ion-implanted specimens as a function of oxidation time at 1000°C in 1 atm O_2. Kinetics curves for the unimplanted Ni-25Cr fell within the shaded area. On the same figure is also presented the weight gain behavior of an Xe^+-implanted specimen and that of a specimen with yttrium implanted onto a preoxidized surface. The preoxidation was carried out at 1000°C in 1 atm. O_2 for 15 minutes. This treatment produced a continuous scale of Cr_2O_3 with occasional small NiO nodules. Its thickness was approximately 1 μm as indicated by SIMS and SEM. The

implantation process caused a discoloration of this preoxidized oxide from dark green to black. However, no noticeable morphological changes was observed under SEM. SIMS analyses indicated that the implanted yttrium concentrated near the outer surface of this thin oxide with a usual range of about 0.2 μm. At least some, if not all, of the implanted yttrium had reacted to form Y_2O_3, as indicated by the relative intensity of the mass 105 (YO^+) signal before and after the implantation.

Table 12 summarizes the oxidation data and presents the scale spallation behavior as an indication of scale adherence. Not all specimens oxidized according to perfect parabolic behavior. As Figure 49 shows, the specimen with $5x10^{16}$ Y^+/cm^2 dosage oxidized almost asymptotically. The "parabolic rate constants" are presented in Table 12 only for easy comparisons between specimens and with results obtained from other studies.

As seen from Figure 49 and Table 12, the implanted Xe caused very little effect on the oxidation rate but increased scale spallation. Only the $5x10^{16}$ Y^+-implanted specimen showed a reduction in the initial oxidation rate, but Y^+ implantation usually reduced the growth rate after 4-5 hours of oxidation. As the implantation dosage decreased, this reduction in growth rate also decreased with the lowest dosage ($1x10^{15}/cm^2$) being almost ineffective. Similarly, none of the Y-implanted specimens showed an increased scale adherence except the one implanted with the highest dosage. The same degree of scale adhesion was also observed on this specimen after 100 hours of isothermal oxidation at 1000°C. The preoxidized, Y^+-implanted specimen showed a much reduced growth rate after an initial period. This reduction in growth rate was comparable to that found with the same dosage of yttrium implanted onto unoxidized surfaces. However, this scale showed no improved adhesion while the scale formed on the specimen with the same dosage of Y^+ implanted directly onto the alloy surface was adherent.

Further examination of the adherence of scales was carried out using cyclic oxidation at 1000°C and at 1100°C on $1x10^{16}$ and $5x10^{16}$ Y^+-implanted specimens. The usual 20-hour cycle was used and the total oxidation time was 100 hours. Figure 50 shows the cyclic oxidation kinetics and the scale spallation of these implanted specimens at 1100°C. Results from six different unim-

planted Ni-25Cr specimens are also presented. The upper and lower limits of these data form the boundaries of the shaded areas. Since the data points for the implanted specimens had to be corrected for oxidation and spallation due to unimplanted areas on the specimens, there is at least 15% error associated with them. Nevertheless, the general trend they present should be reliable. From comparison of Figure 50 to a similar plot for salt coated Ni-25Cr in Figure 38, it is seen that the implanted specimens showed less protectiveness than the salt coated ones, especially those with a heavier coating. Random spallation from the $5x10^{16}$ Y^+-implanted specimen was barely visible after the second cycle. The areas of spallation became more apparent with subsequent cycling. The scales formed on the $1x10^{16}$ Y^+-implanted specimen spalled after the first cycle, as anticipated from the isothermal oxidation results. More spallation was always observed on this specimen than on the more heavily implanted one. As a consequence of the relatively heavy spallation, the scale growth rate of the $1x10^{16}$ Y^+-implanted specimen starts to approach that of the unimplanted specimen after the 4th cycle. At the lower oxidation temperature, the scales were more adherent, especially those formed on the higher dosage specimen. There was only slight spallation towards the end of the testing period.

Annealing of the implanted specimens did not cause any significant difference in the subsequent cyclic oxidation behavior. Figure 51 shows the appearance of an annealed specimen half implanted with $1x10^{16}$ Y^+ and half with $5x10^{16}$ Y^+ after each thermal cycle at 1100°C. The unimplanted area showed very apparent spallation after the end of the first thermal cycle; very localized, fine areas of spallation was observed at this time on the $1x10^{16}$ Y^+-implanted surface. Most of the scale formed on the $5x10^{16}$ Y^+-implanted surface consisted of very fine oxides which showed no spallation. Due to the nonuniformity of the implantation process, various degrees of protectiveness were observed within each implanted area. The more protective areas were probably those which had higher dosages. As oxidation continues, more spallation was observed from the implanted surfaces. By the end of the 5th cycle, all of the implanted areas began to show noticeable spallation.

Scale Morphology and Composition

Initial observations of the surface oxides which developed on various implanted specimens after 50 hours of oxidation at 1000°C were carried out using SEM. Figure 52(a) shows the boundary area between the unimplanted region and the region implanted with $5x10^{16}$ Y^+ on a preoxidized surface. The unimplanted Ni-25Cr developed a thin NiO layer on top of a Cr_2O_3 scale as described earlier (see Figure 39). The top view of the scales shows these NiO grains as seen in Figure 52(b). Although not shown in this field, random spallation was usually observed on the unimplanted surface. The spallations showed areas without scale/alloy contact and a small number of voids. A similar type of spallation was found on the implanted area as indicated by arrows for some parts of Figure 52(c). EDX analysis as well as XRD showed that the scale formed on the implanted side was almost entirely Cr_2O_3.

Surface topography of scale formed on the $5x10^{16}$ Xe^+-implanted specimen is shown in figure 52. The surface oxides were entirely NiO, similar to those formed on the unimplanted Ni-25Cr. The scale as seen from a fractured piece in Figure 53(c) seemed to be porous. Larger and more spalled areas were found on the implanted regions. Spallation often occurred at the scale/alloy interface. Interfacial voids were numerous and there were areas which showed no scale/alloy contact.

The surface oxides developed on specimens subjected to different dosages of yttrium implantation are shown in Figure 54. A very fine grained ($<$ 500 nm) Cr_2O_3 scale with randomly protruding large Cr_2O_3 grains covered the surface of the $5x10^{16}$ Y^+-implanted regions. The diameter of these large grains varied from 1-7 μm. Occasionally they formed clusters. A fractured piece of the scale (Fig. 54b) showed that it consisted of a very fine-grained layer on the outer surface, beneath which was a single-grained layer penetrating into the alloy. This type of scale morphology was very similar to that observed on Y_2O_3, La_2O_3 or CeO_2 salt-coated specimens. Very small spalled areas could occasionally be found on this implanted specimen. However, unlike those on the unimplanted specimen, these areas neither showed a lack of scale/alloy contact nor any interfacial voids.

Figure 54(c) and (d) shows the surface oxides formed on $5x10^{15}$ Y^+- and $1x10^{15}$ Y^+-implanted

specimens respectively. The scale formed on the $1x10^{16}$ Y^+-implanted specimen was very similar to that found on the $5x10^{15}$ Y^+-implanted one. Both showed clusters of Cr_2O_3 grains on the surface. The very fine-grained oxide layer found on the most heavily implanted specimen (as in Fig. 54a) was no longer present. Spalled areas appeared similar to those on the unimplanted except with fewer interfacial voids. The $1x10^{15}$ Y^+-implanted specimen developed a scale that was mostly Cr_2O_3 with randomly distributed small NiO nodules. The spalled areas appeared very similar to those found on the unimplanted specimens.

The undersides of the scale from the various implanted specimens were examined after polishing and deep etching away the underlying alloy using Br_2/MeOH. As seen in Figure 55, all of the nonprotective scales developed nodular oxides at the underside similar to those observed on ZrO_2-coated Ni-25Cr. The nodules varied slightly in size and distribution with different specimens. The largest nodular formation was observed on the most nonprotective scale formed on the Xe^+-implanted specimen. The underside of the protective scale formed on the $5x10^{16}$ Y^+-implanted specimen showed a dramatic difference from the nodular morphology. The appearance was almost identical to that of the underside of the scale found on the CeO_2-coated specimen; the oxide grains appeared uniform and the scale was smooth rather than nodular. The average grain size of this uniform scale was actually larger than that of the nodular scale, as shown in Figure 56.

Cross sections of scales formed on these ion-implanted specimens are shown in Figure 57. The Xe^+-implanted specimen resembled the unimplanted specimen, which had an NiO overgrowth layer. All the other specimens developed single-layered Cr_2O_3. The thickness of this Cr_2O_3 layer decreased with increasing dosage of implanted yttrium in accordance with the kinetics results. The scale observed on the $5x10^{16}$ Y^+-implanted specimen resembled closely that on the La_2O_3, Y_2O_3 or CeO_2 salt-coated specimens where oxide grains of the scale can be seen delineated within the alloy.

After the underlying alloy was deep etched, the cross-sectioned scales were observed under SEM. None of the implanted specimens had developed pegs which extended into the alloy. The protective scale formed on the $5x10^{16}$ Y^+-implanted specimen showed singular oxide grains grow-

ing into the alloy as seen in Figure 58(a). The scales formed on all the other implanted specimens appeared similar to that shown on Figure 58(b) except with varying thickness. A magnified view of a fractured section of the scale shown in Fig. 58(b) indicated that the scale consisted of small, equiaxed grains and it was somewhat porous. The difference in morphology of the protective scale, as in (a), and the nonprotective scale, as in (b) and (c), was dramatic and resembled closely the difference in morphology of the scales formed on the Y_2O_3-coated and the untreated Ni-25Cr specimens respectively as shown in Figure 47.

Sequential development of the oxide scales formed on $1x10^{16}$ Y^+- and $5x10^{16}$ Y^+-implanted Ni-25Cr was studied by oxidizing for various time intervlas specimens implanted with the two dosages on different areas of their surfaces. Figure 59 shows the morphology of surface oxides after 15 minutes, 30 minutes and 300 minutes of oxidation on the unimplanted and the two Y^+-implanted regions. Initially, both the implanted surfaces developed oxides with very fine grains, grains 6-7 times smaller in cross section than those found on the unimplanted surface. These fine grained oxides were much more uniform in size and appeared much smoother on the implanted regions, while grains on the unimplanted regions appeared in clusters of varying sizes. After 30 minutes of oxidation, the morphology of oxides formed on the three surfaces did not change appreciably except that there was some grain growth. With still longer oxidation time, the $1x10^{16}$ Y^+-implanted surface began to develop oxide clusters which grew out of the originally formed fine-grained scale. The oxides on the unimplanted area began to spall, but the scale on the $5x10^{16}$ Y^+-implanted area remained smooth and uniformly fine-grained with only occasional large single grains of Cr_2O_3 growing above the scale. This type of fine-grained morphology persisted for much longer oxidation times. It was observed on specimens oxidized isothermally for 100 hours.

SIMS Depth Profiling of the Scales

SIMS depth profiling starting from the top side of the scales formed on the various implanted surfaces was used to determine the distribution of Y in the scales. The analysis was done using a sputtering rate of approximately 0.1 μm/min with Ar as the ion source. The bombarding ions had a Gaussian distribution with a center of about 100 μm diameter and an extented

tail which give rise to the cratering effect associated with the analysis. Periodic measurements of peak intensities at masses 52 for Cr, 58 for Ni and 89 for Y, or 109 for Xe, were made though the scale into the metal. However, due to the nature of the sputtering mechanism, the scale/metal interface was not sharp and became less so with thicker scales. Figure 60 shows the depth profiles of the different implanted specimens. All of the scales analyzed were rich in Cr. The relative thicknesses of the scales as determined from the sputtering times correlate excellently with the kinetics studies. The Ni content in the scale and especially at the scale/gas interface increased with decreasing implanted dosage of yttrium. There were also higher Ni contents in the scales on the Xe-implanted and on the Y-implanted (preoxidized) specimens. A sharp, high intensity of Y was present in a very narrow region at the scale/gas interface on all of the Y-implanted specimens. Beneath this high surface concentration, the Y intensity decreased rather quickly toward the scale/metal interface on the $5x10^{16}$-implanted surface, but varied much less across the scales formed on the surfaces with lower dosages. A second Y peak was observed near the scale/metal interface on the specimen implanted with Y on a preoxidized surface. Note the difference between this profile and that found on the $5x10^{16}$ Y-implanted specimen even though both received the same dosage of yttrium implant prior to oxidation. The mass 109 peak for Xe is also seen to decrease gradually across the scale. This decrease could be an artifact which arises from a large contribution of the neighboring mass 110 peak ($NiCr^+$), which decreased progressively towards the scale/metal interface.

5.2 Discussion

The most effective surface oxides deposited as salts on the Ni-25Cr, Cr_2O_3-forming alloy prior to oxidation were the oxides of Ce, Y and La. Their effects on the oxidation behavior can be summarized as follows:

1. The oxide growth rate at 1000°C in terms of a gravimetric parabolic rate constant is reduced by nearly a factor of ten.

2. Scale adhesion is greatly enhanced.

3. Formation of a thin NiO layer above the Cr_2O_3 scale is totally eliminated by selective oxidation of the chromium.

4. Except for some occasional small nodules, the growth direction of the scale seems to be altered from outward-growing to inward-growing as indicated by the position of the Pt markers after oxidation, and the general appearance of the scale morphology.

These are essentially the same as the previously reported effects of reactive elements or their oxides present within the alloy. The effectiveness of La, Y and Ce surface oxides relative to the rest of the deposited oxides confirms the result reported by Landkof *et al.*[30] The general effects of these oxides also agree with previous studies on Cr_2O_3 forming alloys.[28],[30]

Surface addition of the reactive elements using ion-implantation showed a dosage dependence similar to that found by Pivin *et al.*[13] and Bennett *et al.*[14] With enough yttrium present in the implantation region, which amounts to an actual dosage of about 10^{16} ions/cm^2 with a maximum peak concentration of 1.2 at% and an average concentration within the implanted region of 0.7 at%, all of the beneficial effects found with the Y_2O_3, La_2O_3 or CeO_2 surface oxide deposits were observed. When the implanted dosage was below this limit, a slight reduction in growth rate and some suppression of base metal oxidation could be found; but the resulting scale showed no improved adhesion and the scale growth direction appeared not to be altered. Similar behavior was observed when yttrium was implanted into a preformed oxide approximately 1 μm thick. The subsequent oxidation rate was greatly reduced, but the scale adhesion was not improved and the scale growth direction was not altered.

In the following subsections, the selective oxidation of chromium, the reduced scale growth and the improved scale adhesion produced by these surface applications of reactive elements will be discussed. Also, a brief section is included to address the detrimental effect of surface-applied HfO_2.

5.2.1 Selective Oxidation of Chromium

The primary effect of surface-deposited oxides on the broaderline Cr_2O_3-former Co-25Cr alloy was to act as a semi-blocking layer. This layer promoted formation of localized Cr_2O_3-rich

regions on the alloy surface by reducing the effective oxygen pressure at the metal suface. These surface oxides, particularly those of La, Y and Ce, however, do not appear to act as a semi-blocking layer on the Cr_2O_3-forming Ni-25Cr alloy. For this alloy fine-grained Cr_2O_3 scale developed everywhere across the salt-treated surface, even on regions with the thinnest deposits of oxides. Although deposited CeO_2 did not have the dense morphology of the Y_2O_3 or La_2O_3 deposits and did not react to form a chromite as they did, the CeO_2 deposit showed the same degree of effectiveness. Furthermore, most of the applied CeO_2 coating formed a loose deposit on the oxide surface and could be easily detached by tapping the specimen. When a cross-section of the scale on a CeO_2-coated specimen was prepared for metallographic study, the CeO_2 coat also detached from the oxide, indicating negligible interaction between the coat and the underlying oxide. While most of the coating was only loosely attached to the oxide surface, small particles of the applied CeO_2 are present within the top surface of the oxide. These particles, which were present throughout the entire coated surface, may be responsible for the observed beneficial effects.

In order to better understand the effects due to these small CeO_2 dispersions, a very thin CeO_2 surface deposit was developed by ultrasonically removing the excess CeO_2 flakes. The morphology of such a deposit is shown in Figure 3. Auger depth profile analysis showed that the average thickness of this kind of a deposit is only 0.1 μm, which is 20-40 times thinner than the usual deposit. Nevertheless, when oxidized, specimens with this thin coverage of CeO_2 proved to be as effective as the usual 2-4 μm thick deposits. The cyclic oxidation data shown in Figure 37 were obtained from a specimen coated with this kind of thin coverage.

Surface-deposited Zr and Ca oxides were found not to be as beneficial as the La, Y and Ce oxides, probably because ZrO_2 and CaO do not form evenly deposited fine dispersions on the alloy surface. For example, after the ZrO_2 coats were treated by an ultrasonic wash, not fine particles of ZrO_2, but thinner ZrO_2 flakes were left on the substrate surface. Oxidation of specimens covered with these thin ZrO_2 flakes showed considerably faster initial rates than those found with thicker ZrO_2 coatings.

The fact that some of these surface-deposited oxides can reduce the transient stage of the

Ni-25Cr alloy, a good Cr_2O_3-former, but cannot promote external Cr_2O_3 scale formation on non-Cr_2O_3 formers is interesting, especially because the deposited oxides sometimes have exactly the same morphologies. This observation appears inconsistent with the suggestion[2] that reactive element oxide dispersions promote an earlier development of the Cr_2O_3 scale is by acting as preferential nucleation sites on the alloy surface, but experimental results from this study do not yet offer other possible explanations for this effect. Detailed study of the oxide nucleation process in these alloy systems is definately needed to elucidate the exact mechanism involved.

5.2.2 Reduced Growth Rate

Reductions of steady-state scale growth rates by yttrium implants increased with dosages. The specimen with the highest dosage showed scale growth rates similar to those produced by the Y_2O_3, La_2O_3 or CeO_2 surface treatments.

The development of Cr_2O_3 scales on yttrium-implanted surfaces was observed after different durations of oxidation time. The initially-formed oxide grains on the implanted surfaces were much finer and grew much slower than on unimplanted specimens. However, when implantation dosages were relatively low, these fine-grained oxides soon gave way to outwardly growing clusters of larger Cr_2O_3 grains. As these outwardly-growing Cr_2O_3 clusters developed, the initially formed fine-grained, Y-rich scale became disrupted. Since the breakdown of this thin Y-rich scale is at localized areas on the Cr_2O_3 scale surface, a fraction of the Y-rich material would remain at the outer surface while fragments became enbedded in the growing Cr_2O_3 scale. Consequently, the SIMS depth analyses, which covered a large circular area of 100 μm diameter showed a sharp Y peak at the scale surface with a rather flat Y profile across the remainder of the scale. Only the specimen implanted with the highest dosage continued to preserve the initially developed fine-grained oxide on the surface for the duration of the testing period (100 hours). The position of the Y peak detected by SIMS depth profiling through this scale indicated that this is the only specimen among those Y-implanted with various dosages on which the scale grew with a change in growth direction.

Pt marker experiments with Y_2O_3-treated specimens verified the change in scale growth direction to inward growth. Due to the similarities in oxidation kinetics and scale morphologies of the Y_2O_3-treated, CeO_2-treated, La_2O_3-treated, and $5x10^{16}$ Y^+-implanted specimens, one can draw the same conclusion that the scales developed on all these specimens also grew by transport of oxygen inward. On the other hand, Pt markers placed on ZrO_2-treated Ni-25Cr showed that the scale growth direction was the same as on the untreated alloy. These scales developed much different morphologies than those mentioned above, but the scale formed on the ZrO_2-treated, the lower dosage Y^+-implanted and the untreated alloy resembled each other closely.

The specimen with a nominal $5x10^{16}$ ions/cm^2 Y^+-implanted into a preformed oxide surface showed a reduced steady state growth rate. The rate was comparable to that found on the specimen with the same dosage of Y^+ implanted into clean alloy surfaces. A SIMS depth profile through this scale showed a large Y peak near the scale/alloy interface. It therefore appears that the growth direction of this scale was not changed since the originally implanted Y remained near the scale/alloy interface. However, it is also possible that chromium diffusion through the originally formed, Y-implanted oxide layer was fast enough to establish a chromium activity at this oxide surface which was high enough so that this oxide surface acted as the "alloy" surface. If so, subsequent scale growth could still result from oxygen inward transport. Figure 61 clarifies these possibilities with schematic illustrations. Both cases (I) and (III) of this figure could give rise to a Y peak concentrated near the scale/alloy interface. However, the morphology of the scale developed on this specimen had a close resemblance to those found on the ZrO_2-treated, the lower dosage Y^+-implanted and the untreated specimens. In other words, the scale morphology indicated that the scale was not formed by a change in growth direction, and case (I) in Fig. 61 should be the correct mechanism.

Mechanisms suggested to explain the reduction in scale growth rate and modification to the transport process brought about by metallic or oxide additions had relied on the relative diffusivities of chromium and oxygen through the Cr_2O_3 scale. From the results of Linder and Akerstrom,[114] Hagel and Seybolt,[67] Hagel[115] and Walters and Grace,[116] O-diffusivity in Cr_2O_3

was found to be 2-3 orders of magnitude lower than the Cr-diffusivity. Therefore, the effect of the reactive element oxides incorporated into the growing oxide scale must have been to reduce chromium diffusion and allow the scale to grow by predominately oxygen transport.

Exactly how the Cr-diffusion was reduced or eliminated to allow for the slower diffusing oxygen to become the rate controlling species is however still an unknown. Stringer *et al.*[2] postulated that the transport of chromium through Cr_2O_3 in the growth of scales on dispersion-free alloys occurs by a short-circuit process, with the most likely short-circuit path being dislocation cores, since according to Laurent and Benard[69] grain boundaries in ionic solids are short-circuit paths for anions, but not for cations. When the grain size of the scale is reduced below a level corresponding to the interdislocation distance in a pileup, a single dislocation is not stable within the grain and will move to grain boundaries. On the other hand, the smaller grains would increase oxygen diffusion by increasing the grain boundary areas. Thus, Cr-diffusion is greatly reduced and O-diffusion enhanced.

Golightly *et al.*[3] suggested that the large Y_2O_3 second phase particles segregate to oxide grain boundaries or other defects and subsequently suppress the outward diffusion of cations, allowing the scale growth to be controlled by the inward transport of oxygen. However, recent TEM studies[18],[21] did not show a preferential segregation of Y_2O_3 to the grain boundaries of the Cr_2O_3 scale.

At present, it is not possible to fully understand the mechanisms involved in producing the reduced growth rate and the change in growth direction, because the transport paths for chromium in the scale are not really known. Chromium ions may diffuse via dislocations,[2] grain boundaries,[117],[118] or via interstitial sites or cation vacancies in the bulk lattice,[119] as various investigators have suggested. Nevertheless, it is an established fact that the Y or other reactive elements, whether originally present in the bulk alloy, ion-implanted, or surface applied as salts, do become incorporated in the Cr_2O_3 scale as second phase particles. Their presence in the scale brought about the reduced growth rate whether it is a consequence of the changed growth direction or not.

The results from this study have shown the same. Initially, a fine-grained thin oxide containing all of the surface-applied reactive elements is formed on the specimen surface. Chromium diffusion must be greatly reduced in this scale, leading to subsequent growth due primarily to oxygen inward transport. When the amount of the reactive element oxide particles were low in the initially formed scale, the scale quickly broke down by allowing the faster chromium outward transport to take over. The specimen with a high yttrium implant onto a preformed oxide surface oxidized by scale outward growth, but the steady state growth rate was very low. Going back to the schematic illustration in Figure 61, case (I), the scale growth can be seen to be controlled by two chromium transport processes connected in series. The first, diffusion through the Y_2O_3-containing initially formed oxide layer, is a very slow one, hence rate limiting. (The transport through this layer could also be predominately oxygen diffusion). The second is a much faster process with chromium diffusing through regions without much Y_2O_3 present.

During a cyclic oxidation test, some of the slow-growing scales formed on the implanted or salt-treated specimens would undoubtedly spall with each cycle no matter how small the spalled areas may be. Since the reactive element oxides are concentrated near the scale/gas interface, spallation usually eliminates all of the REO present in the scale. Subsequently formed oxide scales therefore contained no REO since there is no reactive element present in the underlying alloy. This leads to the faster eventual growth rate observed on specimens with surface-applied reactive metals or their oxides as compared to those with bulk alloying additions. Nevertheless, an appreciable degree of protection was still found with these surface additions.

5.2.3 Improved Scale Adherence

The effect of some of the surface-applied oxides on improving the scale adhesion for the Cr_2O_3 forming alloy is quite surprising. The implanted specimens showed less protection under cyclic oxidation tests than those with the surface oxide deposition. This difference may be due to the presence of implanted carbon impurity which reduce the adhesion of the scale/alloy interface.[120] It may also be due to the nonuniform implantation on the specimen surface, so that areas with less dosage show spallation at an earlier stage, as indicated by experimental results. With the

surface salt deposition process, one also finds a higher degree of protection on more heavily coated specimens. This however, is not a consequence of the thickness of the oxide coat applied, but of a more even coverage of REO on the entire specimen surface, which the heavier coatings usually were able to produce. Thinner coatings on the other hand, leave very small areas uncoated. The scale grown on these uncoated areas would undoubtedly spall more easily.

Whatever protectiveness these surface applied reactive elements may offer, it is reasonable to expect that the protection would eventually break down since there is a lack of replenishing reactive elements in the alloy to heal the spalled oxide scales. Bennett *et al.*[11] and Antill *el al.*[9] who performed long term cyclic testing on yttrium-implanted 15%Cr-4%Al Fecralloy steel at 1100°C in air have found that the Al_2O_3 scale formed was very protective for a maximum of 800 hours at which time the scale thickness was 4 μm. Then, breakaway type of behavior occurred. On the other hand, the same alloy with a 0.86 wt% bulk yttrium addition showed excellent protection throughout the testing period of 4000 hours. Similarly, Landkof *et al.*[30] demonstrated with their preliminary results that the protectiveness offered by surface-applied oxide coats could be recovered by depositing more surface oxides on the existing scale formed on 304 stainless steel specimens. Apparently, the effect of the redeposition process was to cover the spalled areas with replenished reactive metal oxides, allowing the subsequent development of new scales to incorporate these deposited oxides.

Although the surface-applied reactive elements may not offer very long term protection in actual component service, they do exhibit a striking improvement in scale adhesion compared to the untreated alloys for at least 100 hours or more at temperatures as high as 1100°C. Such effects have important implications about the mechanisms which improve the scale adhesion. Earlier explanations in the case of alloys containing the reactive elements or dispersions of their oxide have included:[1]

(a) The internal oxide particles act as vacancy sinks, preventing vacancies from condensing at the oxide metal interface to generate voids.

(b) The internal oxide particles initiate the growth of oxide intrusions - "pegs" - into the metal.

(c) The change in the scale's growth mechanism associated with the presence of the reactive elements prevents lateral oxide growth within the scale and thus prevents scale convolution, resulting in the maintenance of a continuous scale/alloy contact.

(d) The reactive element collects at the oxide/metal interface and modifies the binding energy[4],[5] or getters impurities diffusing from the interior of the alloy to the alloy/scale interface which weaken the interfacial bonds.[6],[7]

Since the reactive element oxide is not present within the alloy, it is difficult to see how the first two of the above mechanisms can be effective. Furthermore, examination of the underside of the scale formed on the salt treated specimens or the ion-implanted ones showed no peg formation while the scale remained adherent.

It is possible that the reactive element oxides may getter surface impurities present as a result of specimen preparation or may getter impurities that diffuse to the surface during heating of the specimen, since surface segregation of sulfur at these high temperatures can be very rapid. For example, Smeggil *et al.*[7] observed a steady state sulfur concentration on specimen surfaces in vacuum in less than 10 minutes at temperatures $>$ 800°C. However, if this initial scavenging of surface and near surface impurities were responsible for the improved adhesion, one would expect the ZrO_2-coated specimens to develop adherent scales as well, especially since Zr and La added in the alloy were found equally effective in improving grain boundary strength by trapping sulfur.[121]

As the oxide scale thickens with time, the surface-applied reactive element becomes concentrated at the scale/gas interface as a result of scale growth. Some small amounts of CeO_2 were found at the scale/alloy interface which could be capable of scavenging impurities diffusing from the bulk of the alloy to the interface. However, in ZrO_2-treated specimens, Zr was also found present at the scale/alloy interface, but this scale was not adherent: the same degree of spallation was found as on the untreated alloy. Furthermore, the scale formed on the $5x10^{16}$ Y^+-implanted surface had the yttrium concentrated at the outer scale surface but the scale continued to be

adherent. On the other hand, the scale formed on the surface with the same dosage of yttrium implanted onto a preformed thin oxide layer had the yttrium concentrated very close to the scale/alloy interface but this scale was not adherent. Nagai *et al.*[122] have shown that the addition of Al to Ni-20wt%Cr greatly improved the scale adherence at 1373K. The beneficial effect of Al was even better than that of La or Y additions. However, Mulford[123] reported that the addition of Al to Ni was not as effective as a Cr addition in preventing sulfur segregation to grain boundaries between 900-1300K. The results of these two studies clearly indicate that the effectiveness of Al in a Ni-Cr alloy in improving the scale adhesion can not be simply due to sulfur scavenging by the Al. Nagai *et al.*[122] attributed the effectiveness of Al to the formation of internal oxide pegs of Al_2O_3. Although results obtained from this study and some of the previous investigations cited above do not support the 'impurity gettering' mechanism, recent experiments carried out on alloys forming Al_2O_3 scales by Smialek[124] showed convincing evidence for it. Further investigation in this area is needed before one can draw a conclusion about this newly proposed mechanism.

From the results of this study, scale adherence seems most likely to be related to the change in scale growth mechanism associated with the presence of the reactive element oxides whether they were applied on the surface as salts or were ion-implanted. Microscopic observations showed that all of the adherent scales developed very similar morphologies. Each adherent scale showed a very fine-grained, reactive element-rich outer layer, a nonporous almost single grained scale and a very smooth, uniform grain-sized underside at the scale/alloy interface. All of these scales were grown by predominately oxygen inward transport. The nonadherent scales on the other hand, all developed much larger uneven grains on the surface (sometimes with a high concentration of NiO present); the nonadherent scales contained equiaxed grains and were porous. At the scale/alloy interface, the scale was very nodular and these scales grew by predominately chromium outward transport.

These differences observed between the adherent and the nonadherent scales all seem to suggest that the enhanced adherence could be related to the way the scale is developed. It seems critical that the reactive elements are present and are initially in contact with the alloy surface. This

conclusion is supported by the fact that when Pt strips were sandwiched between the deposited oxide and the alloy surface, the scale showed faster, more outward growth and poorer adherence. Furthermore, when implanted yttrium was only present within a preformed oxide layer, not in direct contact with the metal surface, the resulting scale was slow-growing but showed no improved scale adhesion nor a change in scale growth direction. The result of the initial contact with the alloy surface was to develop a very fine-grained, reactive element-rich thin oxide layer. This layer is possibly responsible for the change in scale growth direction in subsequent scale formation. Golightly *et al.*[3] have suggested that the suppression of any outward transport of chromium through the scale eliminates lateral oxide growth, which generates stresses causing large areas to grow out of contact with the alloy. It is not certain, however, from the results of this work that this is indeed the process involved. Rather, it seems possible that the inwardly-growing scale was more adherent because such a growth process leads to structurally more coherent scale/alloy interfaces, as seen from the uniform smooth scale at the underside of the adherent oxides. Such interfaces would undoubtedly be stronger and therefore lead to less scale spallation.

5.2.4 The Influence of Surface Applied HfO_2

Among all the surface deposited oxides the most non-precipitate-like and nonadherent one was that of Hf. Usually after an ultrasonic wash, there would only be very few HfO_2 flakes left on the substrate surface. The effects due to surface HfO_2 proved to be detrimental, even though bulk addition of HfO_2 particles were reported to be as effective as other reactive element dispersoids.[34],[35] A possible mechanism by which these surface HfO_2 flakes enhanced oxidation is explained by the schematic illustration shown in Figure 62. The kinetics curve clearly shows three stages of oxidation. During stage I, normal growth takes place and the behavior approximates to that observed with ZrO_2 or CaO deposits on the surface. Occasionally, when the density of the deposited HfO_2 was reduced, this first stage growth would continue without the subsequent breakaway behavior. However, the resulting scale was found to be very nonadherent to the substrate, developed many cracks and spalled almost entirely upon cooling. Deposited HfO_2 flakes were found lifted and embedded in this scale. The presence of these thin flakes either greatly reduced

scale/alloy adhesion, or enhanced local cracking once they had become embedded in the scales. Both situations would result in cracking of the scale at temperature, exposing the underlying Cr-depleted alloy to the oxidant. Stage II then represents the fast oxidation of the Cr-depleted zone until a healing Cr_2O_3 layer is developed. In stage III, the growth rate resumes a slow normal rate after the development of a continuous Cr_2O_3 layer free of the deposited HfO_2.

CHAPTER SIX

Summary and Conclusions

This study is the first which investigates the effect of surface-applied reactive elements and their oxides on the oxidation of alloys that normally do not have enough Cr to form a continuous Cr_2O_3 external scale. Additions of 1-2 vol% of reactive element oxides in several non-Cr_2O_3 forming Co-Cr alloys have been shown to be effective in promoting the Cr_2O_3 scale formation. Nevertheless, none of the ion-implanted reactive elements or of the surface-deposited reactive element oxides showed any effect on the subsequent oxidation behavior of the Co-15Cr alloy at 1000°C or 1100°C in 1 atm. O_2.

The Co-25Cr alloy is a borderline Cr_2O_3 former: forming a cobalt rich oxide scale when oxidized under high P_{O_2}, but a continuous Cr_2O_3 scale under low oxygen potentials. Again, none of the surface-treated specimens developed a continuous Cr_2O_3 external scale as they would with the reactive elements being present within the alloys. Surface-deposited La_2O_3, Y_2O_3 and CaO were able to locally promote some Cr_2O_3 scale formation at 1000°C, but lost their effectiveness at 1100°C. This ability to locally promote the Cr_2O_3 scale or to increase the Cr content in the oxide depends largely on the morphology of the deposited oxide coats. Furthermore, in order to produce such effects, the presence of a relatively large quantity of the surface-deposited oxide is necessary. It is concluded that the primary effect of these surface-deposited oxide coats is to act as a blocking layer which decreases the initial oxygen to alloy contact.

Ion-implantation of Y or La had little effect on the oxidation of the Co-25Cr alloy. Scales developed on the implanted surfaces even showed a higher degree of spallation. Annealing of these specimens eliminated the excess tendency of spallation by removing the radiation damage associated with the implantation process. Only when the implantation dosage is very high (i.e. $1x10^{18}$ ions/cm^2) can a continuous Cr_2O_3 scale be promoted and this scale is very adherent. Internal oxidation of the implanted yttrium, converting it to its oxides prior to the oxidation, can facilitate the development of this Cr_2O_3 external scale. However, unlike the case of reactive element alloying additions, these developed Cr_2O_3 scales cannot remain protective but break down after a short

time of oxidation. The period before scale breakdown is longer with higher implantation dosage.

The more rapid development of a continuous external Cr_2O_3 scale on dispersion-containing alloys was previously proposed to be due to the dispersoids acting as preferential nucleation sites on the alloy surface. The fact that the presence of these dispersions on the surfaces alone did not show a similar effect seems to suggest that the model is incorrect, or is at least incomplete. In the case of the specimen with a very high dosage of implanted yttrium, reactive elements in the surface region were able to promote a continuous external Cr_2O_3 scale. However, this scale is not stable. It is suggested that an added effect wich gives the Cr_2O_3 scale formed on normally non-Cr_2O_3 formers its stability may be the alloying reactive elements continuously acting as vacancy sinks, thus preventing vacancy condensation and void formation at the critical scale/alloy interface.

With the good Cr_2O_3-forming alloy: Ni-25Cr, surface-deposited La_2O_3, Y_2O_3 and CeO_2 as well as ion-implanted La and Y all affect the oxidation behavior in the same way as with alloying additions. Furthermore, the effectiveness of the surface oxide coats is no longer dependent upon their morphology. Coatings that are 20-40 times thinner than the usual deposit are equally effective. All of these beneficial surface additives caused the selective oxidation of Cr and totally eliminated any base metal oxide formation; they significantly reduced the growth rate of the Cr_2O_3 scale and changed the scale growth mechanism from predominately metal transport to predominately oxygen transport; they also reduced the oxide grain size and greatly improved the scale adherence. The morphology of scales developed on the treated specimens are very different from that on the untreated, in that the scale is less porous, singly layered and has finer and much more uniform grains at the scale/gas and the scale/alloy interfaces. Most of the applied reactive elements are present at the scale/gas interface after oxidation, but some are also found within the scale and at the scale/alloy interface.

The improved scale adhesion is not related to the selective oxidation of chromium nor is it related to the slower growth of the Cr_2O_3 scale, since both of these effects were observed on a Y-implanted specimen whose scale was not adherent. There is also no peg formation which can

mechanically key the scale to the underlying alloy to give a better scale to alloy contact. Furthermore, the enhanced scale adherence could not be attributed to the 'vacancy sink' model, since the added reactive elements or their oxides were not present in the alloy. Although results from this study do not support the recently proposed mechanism concerning impurity gettering by the reactive element additions, more detailed study is called for to further investigate its vilidity. From the morphological differences observed on the adherent and the nonadherent scales, it is suggested that the improved scale adherence caused by the reactive element addition is related to the modified growth and early development of the oxide scale.

Possible physical effects arising form the implantation process itself are minimal. Implanted Xe showed no influence on the oxidation behavior except that the scale formed was less adherent. On the Y or La implanted specimens the decreased scale adhesion caused by the radiation damage was outweighed by the effects produced by the reactive element. A minimum dosage is necessary in orders for the implanted reactive metal to exert significant effects. This dosage is 1.5 order of magnitude lower than that required for the Co-25Cr, and corresponds to a peak concentration of approximately 1-2 at%, which is comparable to that required in the case of alloying additions.

Not all of the surface-deposited reactive element oxides were beneficial. ZrO_2 and CaO showed little effect on the oxidation behavior of Ni-25Cr. The oxidation rate was only slightly reduced and the scale adherence was not improved. Often there was no suppression of base metal oxide formation and the scale growth direction was not altered. The surface-deposited HfO_2 even caused a breakaway behavior at the early stage of the oxidation process. The initial scale developed on the HfO_2-treated specimen was very convoluted and fractured at the oxidation temperature. This fracture leads to a higher degree of base metal oxidation until a healing layer of Cr_2O_3 is formed which is free of the deposited HfO_2. The relative effectiveness of the different surface-applied oxides possibly arose from their relative ability to form small particles in contact with the alloy surface. This initial good contact seems to be important in producing the subsequently observed beneficial effects.

References

1. D. P. Whittle, and J. Stringer, *Phil. Trans. Roy. Soc. London* **A27(56)**, 309, (1979)

2. J. Stringer, B. A. Wilcox and R. I. Jaffee, *Oxid. of Metals* **5**, 11, (1972)

3. F. A. Golightly, F. H. Stott and G. C. Wood, *Oxid. of Metals* **10**, 163, (1976)

4. A. B. Anderson, S. P. Mehendru and J. L. Smialek, *J. Electrochem. Soc.* **132**, 1695, (1985)

5. J. L. Smialek and R. Browning, Pro. of the Symp. on High Temperature Materials Chemistry III, ed. by Z. A. Munir and D. Cubiciotti, **86-2**, 258, 168th ECS Fall meeting, Las Vegas, Oct. 1985

6. A. W. Fundenbusch, J. G. Smeggil and N. S. Bornstein, *Met. Trans.* **16A**, 1164, (1985);

7. J. G. Smeggil, A. W. Funkenbusch and N. S. Bornstein, *Met. Trans.* **17A**, (1986) in press

8. L. B. Pfeil, 1945 U. K. Patent No. 574088

9. J. E. Antill, M. J. Bennett, R. F. A. Carney, G. Dearnaley, F. H. Fern, P. D. Goode, G. L. Myatt, J. F. Turnaer and J. B. Warburton, *Corr. Sci.* **10**, 729, (1976)

10. U. Bernabai, M. Cavallini and G. Bombara, *Corr. Sci.* **20**, 19, (1980)

11. M. J. Bennett, M. R. Houlton and G. Dearnaley, *Corr. Sci.* **20**, 69, (1980)

12. M. J. Bennett, G. Dearnaley, M.R. Houlton, R. W. M. Hawes, P.D. Goode and M. A. Wilkins, *Corr. Sci.* **20**, 73, (1980)

13. J. Pivin, C. Roques-Carmes, J. Chaumont and H. Bernas, *Corr. Sci.* **20**, 947, (1980)

14. M. J. Bennett, G. Dearnaley, M. R. Houlton and R. W. M. Hawes, "*Ion implantation Into Metals*", p.264, Pergamon Press Pub., 1981

15. F. H. Stott, J. S. Punni, G. C. Wood and G. Dearnaley, "*Ion Implantaion Into Metals*", p.245, Pergamon Press Pub., 1981

16. J. A. Sprague, G. R. Johnston, F. A. Smidt, Jr., S. Y. Hwang, G. H. Meier and F. S. Pettit, "*High Temperature Protective Coatings*", ed. by S. C. Singhal, Proc. 112th AIME meeting, p.93, March, 1983

17. M. J. Bennett, B. A. Bellamy, B. Dearnaley and M. R. Houlton, Proceedings of the 9th ICMC Conf., Toronto, **2**, 416, 1984

18. F. H. Stott, J. S. Punni, G. C. Wood and G. Dearnaley, Conf. Proc. on "*Transport in Non-Stoichiometric Compounds*", Pennsylvania State Univ., 1984

19. S. K. Lau, R. R. Jensen, R. Kossowsky and S. C. Singhal, "*Surface Engineering*", p.496, ed. by R. Kossowsky and S. C. Singhal, NATO ASI Series, Martinus Nijhoff pub., 1984

20. F. A. Smidt, G. R. Johnston, J. A. Sprague, V. Prorenzano, S. Y. Hwang, G. H. Meier and F. S. Pettit, *ibid* p.507, (1984)

21. C. H. Yang, G. E. Welsch and T. E. Mitchell, *Mat. Sci. and Eng.* **69**, 351, (1985)

22. M. J. Bennett, B. A. Bellamy, C. F. Knights and Nicola Meadows, *Mat. Sci. and Eng.* **69**, 359, (1985)

23. M. J. Bennett, J. A. Desport and P. A. Labun, Presented at the 43rd EMSA meeting, Luisville, Kentucky, August 1985

24. C. H. Yang, P. A. Labun, G. Welsch, T. E. Mitchell and M. J. Bennett, HARWELL Report No. AERE-R12088, January 1986

25. C. Tyzack, H. C. Cowen, M. Farrow and P. B. Longton, Proc. of the B.N.E.S. International Conf. on Corrosion of Steels in CO_2, p.359, September 1974

26. A. T. Chadwick, HARWELL Report No. ARER R-10352, January 1982

27. M. J. Bennett, M.R. Houlton and R. W. M. Hawes, *Corr. Sci.* **22**, 111, (1982)

28. G. M. Ecer, R. B. Singh and G. H. Meier, *Oxid. of Metals* **18**, 55, (1982)

29. M. J. Bennett, "*Coatings for High Temperature Applications*" ed. by E. Lang, Elsevier Scientific Publishing Co. p.109, (1983)

30. M. Landkof, A. V. Levy, D. H. Boone, R. Gray, and E. Yaniv, *Corrosion* **41**, 344, (1985)

31. H. H. Davis, H. C. Graham and I. A. Kvernes, *Oxid. of Metals* **3**, 431, (1971)

32. J. Stringer and I. G. Wright, *Oxid. of Metals* **5**, 59, (1972)

33. I. G. Wright and B. A. Wilcox, *Oxid. Met.* **8**, 283, (1974)

34. D. P. Whittle, M. E. El Dahshan and J. Stringer, *Corros. Sci.* **17**, 879, (1977)

35. P. K. Kofstad and A. Z. Hed, *J. Electrochem. Soc.* **116**, 1542, (1969)

36. G. C. Wood and T. Hodgkiess, *J. of Electrochem. Soc.* **113**, 319, (1966)

37. L. B. Pfeil, 1937 U. K. Patent No. 459848

38. J. M. Francis and W. H. Whitlow, *Corr. Sci.* **5**, 701, (1965)

39. A. M. Beltran, *Cobalt* **46**, 3, (1970)

40. C. S. Giggins and F. S. Pettit, *Met. Trans.* **2**, 1071, (1971)

41. G. R. Wallwork and A. Z. Hed, *Oxid. Met.* **3**, 229, (1971)

42. J. E. Antill, and K. A. Peakall, *J. Iron Steel Inst.* **205**, 1136, (1967)

43. J. M. Francis and W. H. Whitlow, *J. Iron Steel Inst.* **204**, 355, (1966)

44. I. G. Wright, B. A. Wilcox and R. I. Jaffee, *Oxid. Met.* **9**, 275, (1975)

45. H. T. Michels, *Met. Trans.* **7A**, 379, (1976)

46. J. K. Tien and F. S. Pettit, *Met. Trans.* **3**, 1587, (1972)

47. K. P. R. Reddy, J. C. Smialek and A. R. Cooper, *Oxid. of Metals* **17**, 429, (1982)

48. J. Stringer, I. M. Allam and D. P. Whittle, *Thin Solid Films* **45**, 377, (1977)

49. I. A. Allam, D. P. Whittle and J. Stringer, *Oxid. Met.* **12**, 35, (1978); **13**, 381, (1979)

50. I. A. Kvernes, *Oxid. Met.* **6**, 45, (1973)

51. A. Kumar, M. Hasrallah and D. L. Douglass, *Oxid. Met.* **8**, 227, (1974)

52. J. D. Kuenzly and D. L. Douglass, *Oxid. Met.* **8**, 139, (1974)

53. C. S. Giggins and F. S. Pettit, Final Report to Aerospace Research Laboratories, Wright-Petterson Air Force Base, Contract F 33615-72-C-1702 (1975)

54. M. J. Fleetwood, *J. Inst. Met.* **94**, 218, (1966)

55. B. Wenderott, *Z. Metallk.* **56**, 63, (1965)

56. C. Wagner, *Z. Elecktrochem.* **63**, 772, (1959)

57. M. S. Seltzer, B. A. Wilcox and J. Stringer, *Met. Trans.* **3**, 2391, (1972)

58. M. S. Seltzer, *ibid* **3**, 2357, (1972)

59. C. S. Giggins and F. S. Pettit, *Trans. TMS-TIME* **245**, 2509, (1969)

60. P. Nanni, C. T. H. Stoddart and E. D. Hondros, *Mat. Chem.* **1**, 297, (1976)

61. O. T. Goncel, J. Stringer and D. P. Whittle, *Corr. Sci.* **18**, 701, (1978)

62. H. M. Flower and B. A. Wilcox, *Corr. Sci.* **17**, 253, (1977)

63. D. A. Braski, P. D. Goodell, J. V. Cathcart and R. H. Kane, *Oxid. of Met.* **25**, 29, (1986)

64. P. Kofstad, "*Nonstoichiometry, Diffusion and Electrical Conductivity in Binary Metal Oxides*" Pub. Wiley-Interscience, 1972

65. K. Hauffe and J. Block, *Z. Phys. Chem.* **198**, 233, (1951)

66. G. Lorenz and W. A. Fischer, *Z. Phys. Chem. Nene Floge* **18**, 265, (1958)

67. W. C. Hagel and A. U. Seybolt, *J. Electrochem. Soc.* **108**, 1146, (1961)

68. G. C. Wood and J. Boustead, *Corr. Sci.* **8**, 719, (1968)

69. J. F. Laurant and J. Benard, *Phys. Chem. Solids* **7**, 218 (1958)

70. H. Pfeiffer, *Werk. u. Korr.* **8**, 574, (1957)

71. J. Stringer, *Met. Rev.* **11**, 113, (1966)

72. B. Lustman, *Trans. TMS-AIME* **188**, 995, (1950)

73. C. S. Wukusick and J. F. Collins, *Mat. Res. Stand.* **4**, 637, (1964)

74. H. Hindam and D. P. Whittle, *J. Electrochem. Soc.* **129**, 1147, (1982)

75. H. Hindam and D. P. Whittle, Pro. JIMIS-3: High Temperature Corrosion, *Trans. of the Japan Inst. of Metals, Suppl.* p.261, (1983)

76. J. C. Pivin, D. Delaunary, C. Roques-Carmes, A. M. Huntz and P. Lacombe, *Corr. Sci.* **20**, 351, (1980)

77. J. M. Francis, and J. A. Jutson, *Corr. Sce.* **8**, 445, (1968)

78. D. Delaunay, A. M. Huntz and P. Lacombe, *Corr. Sci.* **20**, 1109, (1980)

79. D. Delaunay, A. M. Huntz and P. Lacombe, *J. less-common Metals* **70**, 115, (1980)

80. G. W. Hollenberg and R. S. Gordon, *J. Amer. Ceram. Soc.* **56**, 140, (1973)

81. J. E. McDonald, ad J. B. Eberhart, *Trans. TMS-AIME* **233**, 512, (1965)

82. S. V. Pepper, *J. Appl. Phys.* **47**, 801, (1976)

83. Lori McConnell Kingsley, "*Al_2O_3 adherence on CoCrAl Alloys*" M. S. Thesis, U. C. Berkeley, April 1980

84. C. L. Briant and R. A. Mulford, *Met. Trans.* **13A** , 745, (1982)

85. R. P. Messmer and C. L. Briant, *Acta. Met.* **30**, 457, (1982)

86. G. Dearnaley and N. E. W. Hartley, *Thin Solid Films* **54**, 215, (1978)

87. G. Dearnaley, *Nuclear Inst. and Methods* **182/183**, 899, (1981)

88. M. J. Bennett, Presented at the NACE International Conferance on High Temperature Corrosion, San Diego, March, 1981

89. M. Caillet, Presented at the 164rd ECS meeting, Washington DC, October, 1983

90. A. Galerie, M. Caillet and M. Pons, *Mat. Sci. and Eng.* **69**, 329, (1985)

91. J. Lindhard, M. Scharff and H. E. Schiott, *Mat-Fys. Medd. K. Dan. Vidensk. Selsk.*, **33**, 14 (1963)

92. P. Haymann and C. Waldburger, "*Ionic Bombardment, Theory and Applications*" C.N.R.S. Symposium Science Publ. Inc. 1964

93. O. Almen and G. Bruce, *Nucl. Instr. Methords* **11**, 279, (1961); **11**, 257, (1961)

94. H. Nagai, M. Okabayashi and H. Mitani, *Tran. Japan Inst. of Metals,* **21**, 341 (1980)

95. R. Brueckner, *J. Non-Cryst. Solids,* **5(2)**, 123 (1970); **5(3)**, 177, (1970-71)

96. P. Y. Hou, M. S. Thesis, University of California, Berkeley, May 1983

97. P. K. Kofstad and A. Z. Hed, *J. Electrochem. Soc.* **116**, 224, (1969); **116**, 229, (1969)

98. I. G. Wright and G. C. Wood, *Oxid. of Metals* **11**, 163, (1977)

99. W. F. Ford and J. White, *Trans. Brit. Ceram. Soc.* **48**, 423 (1949)

100. "*The Oxide Handbook*", 2nd edition, Ed. by G. V. Samsonov, IFI/Plenum publication, 1982.

101. A. Preece and J. Lucas, *J. Inst. Met.* **81**, 219, (1952)

102. C. A. Phalnikar, E. B. Evans and W. M. Baldwin, *J. Electrochem. Soc.* **103**, 429 (1956)

103. A. Davin, D. Coutsouradis, and L. Habraken, *Cobalt* **35**, 69 (1967)

104. F. R. Billman, *J. Electrochem. Soc.* **119**, 1198 (1972)

105. G. C. Wood, I. G. Wright, T. Hodgkiess and D. P. Whittle, *Werkst. Korros.* **21**, 900 (1970)

106. I. G. Wright, "*Oxidation of Iron- Nickel- and Cobalt- Base Alloys*", Metals and Ceramics Information Center, Batelle-Columbus Laboratories, Rep. MCIC-72-07 (June 1972)

107. F. H. Stott, I. G. Wright, T. Hodgkiess and G. C. Wood, *Oxid. of Metals* **11**, 141 (1977)

108. D. E. Jones and J. Stringer, *Oxid. of Metals* **9**, 409 (1975)

109. B. P. Buliya, F. N. Tavadze, O. I. Mikadze, A. D. Neuimin and S. F. Palguev, *Soobshch. Akad. Nauk GSSR* **105**, 317 (1982)

110. I. M. Rehn, EPRI Report No. CS-1811, April (1981)

111. I. G. Wright, B. A. Wilcox and R. I. Jaffee, Final Report on Naval Air Systems Command Contract No. WOO 19-72-C-0190, January 1973.

112. D. P. Whittle, D. J. Evans, D. B. Scully and G. C. Wood, *Acta Met.* **15**, 1421 (1967)

113. G. C. Wood and D. P. Whittle, *Corro. Sci.* **4**, 263 (1964)

114. R. Lindner and A. Akerstrom, *Z. Phys. Chem. N. F.* **6**, 162 (1956)

115. W. C. Hagel, *J. Am. Cer. Soc.* **48**, 70 (1965)

116. L. C. Walters and R. E. Grace, *J. Appl. Phys.* **8**, 2331 (1968)

117. D. Caplan and G. I. Sproule, *Oxid. of Metals* **9**, 459 (1975)

118. A. Atkinson and R. I. Taylor, Harwell Report: AERE-R 11314, June 1984.

119. F. A. Kruger, in "*High-Temperature Corrosion*", ed. by R. A. Rapp, NACE-6:89 (1983)

120. M. J. Bennett, private communication (1986)

121. J. E. Doherty, B. H. Kear, A. F. Giamei and C. W. Steinke, "*Grain Boundaries in Engineering Materials*", Proc. of the 4th Bolton Landing Conference, June 1974, ed. by J. L. Walter, J. H. Westbrook and D. A. Woodford

122. H. Nagai, M. Okabayashi and H. Mitani, *Trans. Japan Inst. of Metals,* **21**, 341, (1980)

123. R. A. Mulford, *Met. Tran. A,* **14A**, 865 (1983)

124. J. L. Smialek, to be published.

125. O. T. Goncel, D. P. Whittle and J. Stringer, *Oxid. of Metals* **15**, 287 (1981)

TABLE 1: Chemical analysis of the alloys

Alloy Type	Chemical Composition in Weight Percent							
	Cr	Mn	Fe	Ni	Co	Si	S	Y
Co-15Cr	15.9	.003	.098	.108	bal	.017	.004	
Co-25Cr	25.1	.005	.031	.116	bal	.020	.019	
Co-25Cr-1Y	24.41				bal		.002	0.98
Ni-25Cr	25.7	.001	.023	bal	.021	.016	.008	

TABLE 2: Distribution of implanted ions using 400 keV voltage

			Calculated by the LSS Procedure			Experimental Measurement by RBS			
substrate	ion implanted	dosage (atoms/cm^2)	max.con. (at%)	depth(A) of max. con.	depth(A) of implantation	dosage (atoms/cm^2)	max.con. (at%)	depth(A) of max. con.	depth(A) of implantation
Co-25Cr	Y^+	$1x10^{16}$	1.73	679	1478				
		$5x10^{16}$	8.63	679	1478				
		$3x10^{17}$*				10^{16}-10^{17}	6.73	760±90	1595
		$1x10^{18}$	>100	679	1478	$4x10^{17}$	23.54	510±70	1430
	La^{2+}	$1x10^{16}$	2.48	494	1049	$3x10^{15}$	0.65	440±60	1120
Ni-25Cr	Y^+	$1x10^{15}$	0.17	691	1504				
		$5x10^{15}$	0.84	691	1504				
		$1x10^{16}$	1.67	691	1504				
		$5x10^{16}$	8.37	691	1504				
	La^{2+}	$1x10^{16}$	2.42	502	1064	$7.5x10^{15}$	1.35	450±40	1190
	Xe^+	$5x10^{16}$	11.37	520	1118				

* Implanted with three different voltages: 400 keV, 800 keV and 1800 keV, with $1x10^{17}/cm^2$ dosage per voltage.

TABLE 3: Oxidation data for Co-15Cr and Co-15Cr coated with different surface oxides after 24 hours at 1000°C.

Deposited Oxide	Weight gain from oxidation
Untreated	40.4
Cr(0.3)	41.6
Ca(0.5)	42.0
Ce(0.8)	42.0
Hf(0.4)	41.7
La(0.3)	42.2
Y(0.7)	39.9
Zr(0.7)	43.4

All figures are in units of mg/cm^2. Numbers in parentheses are the weight of deposited oxide.

TABLE 4: Oxidation data for Co-25Cr and the same alloy coated with different amounts of La_2O_3 after 24 hours at 1000°C.

Deposited Oxide	Wt. gained from oxidation	Wt. spalled from cooling
Untreated	5.11	7.72
La(0.04)	4.76	7.81
La(0.2)	2.12	0.19
La(0.8)	2.90	0.13

All figures are in units of mg/cm^2. Numbers in parentheses are the weight of deposited oxide.

TABLE 5: Oxidation data for Co-25Cr and Co-25Cr coated with different surface oxides after 24 hours at 1000°C.

Deposited oxide	Weight gained from oxidation	Weight spalled from cooling
Untreated	5.11	7.72
Hf(0.3)	6.64	10.34
Cr(0.4)	5.26	4.97
Ce(0.4)	3.65	2.89
Zr(0.3)	3.14	3.27
Y(0.4)	2.42	0.38
La(0.2)	2.12	0.19
Ca(0.5)	1.46	0.18

All figures are in units of mg/cm^2. Numbers in parentheses are the weight of deposited oxide.

TABLE 6: Oxidation data for Co-25Cr and Co-25Cr(coated oxide) after 50 hours at 1100°C.

Deposited Oxide	Weight gained from oxidation	Weight spalled from cooling
Co-25Cr	9.17 ± 0.12	7.49 ± 1.31
Co-25Cr(Hf)	9.89	12.09
Co-25Cr(Cr)	8.24	8.24
Co-25Cr(Ce)	9.87	8.76
Co-25Cr(Zr)	10.19	5.07
Co-25Cr(La)	7.17	8.30
Co-25Cr(Y)	6.23	8.65
Co-25Cr(Ca)	10.48 ± 0.42	1.07 ± 0.07

All figures are in units of mg/cm^2.

TABLE 7: Summary of oxidation of Co-25Cr, Co-25Cr-1Y and Co-25Cr(ion-implanted) alloys after 24 hours in oxygen at 1000°C.

Alloy	k_p ($mg^2cm^{-4}hr^{-1}$)	Spallation Behavior
Co-25Cr	1.34 ± 0.21	General spallation detected after cooling
Co-25Cr-1Y	0.08	no spallation
Co-25Cr(La^{2+}, $1x10^{16}$)	0.49	Implanted area showed higher degree of spallation
Co-25Cr(La^{2+}, $1x10^{16}$) annealed	0.51	Implanted area spalled to the same degree as the unimplanted area
Co-25Cr(Y^{+}, $1x10^{16}$)	0.44	Implanted area showed higher degree of spallation
Co-25Cr(Y^{+}, $5x10^{16}$)	0.34	Implanted area showed higher degree of spallation
Co-25Cr(Y^{+}, $3x10^{17}$)	0.26	Implanted area showed higher degree of spallation
Co-25Cr(Y^{+}, $1x10^{18}$)	0.02	Implanted area showed no spallation
Co-25Cr(Y^{+}, $1x10^{18}$) annealed	0.02	Implanted area showed no spallation

TABLE 8: Parabolic rate constants of internal oxidation treated Co-25Cr, Co-25Cr-1Y and Co-25Cr(Y^+-implanted) alloys after oxidation at 1000°C in O_2.

Alloy	Duration of Internal Oxidation Treatment at 1000°C	k_p ($mg^2cm^{-4}hr^{-1}$)	Spallation Behavior
Co-25Cr	0	1.34 ± 0.21	Amount of spallation decreased with decreasing weight gain
Co-25Cr	2 hours	0.49	
Co-25Cr	100 hours	0.20	
Co-25Cr-1Y	0	0.08	None of these showed measurable spallation
Co-25Cr-1Y	2 hours	0.09	
Co-25Cr-1Y	100 hours	0.06	
Co-25Cr($1x10^{16}$ Y^+/cm^2)	0	0.44	All the implanted surfaces showed slightly more spallation than the untreated. I.O. treatment renders no further effect
Co-25Cr($1x10^{16}$ Y^+/cm^2)	2	0.46	
Co-25Cr($3x10^{17}$ Y^+/cm^2)	0	0.26	
Co-25Cr($3x10^{17}$ Y^+/cm^2)	2 hours	0.23	

TABLE 9: Oxidation data for Co-40Cr and Co-40Cr(CeO_2-coated) after 24 hours at 1000°C.

Specimen	Weight gained from oxidation (mg/cm^2)	Weight spalled from cooling (mg/cm^2)	Approximate k_p ($mg^2\ cm^{-4}\ hr^{-1}$)
Co-40Cr	1.35	3.86	$6.43x10^{-2}$
Co-40Cr(Ce)	0.31	0.07*	$2.19x10^{-3}$

* All spallation came from specimen sides which were not coated by the CeO_2.

TABLE 10: Oxidation data for Ni-25Cr and Ni-25Cr(coated oxide) after 45 hours at 1000°C.

Deposited oxide	Weight gained from oxidation	Weight spalled from cooling
Untreated	1.31	0.14
Hf(0.8)	1.65	1.80
Cr(0.2)	1.14	0.14
Ca(0.4)	0.72	0.35
Zr(0.5)	0.61	0.11
Y(0.4)	0.36	0
La (0.2)	0.35	0
Ce(0.6)	0.26	0

All figures are in units of mg/cm^2. Numbers in parentheses are the weight of deposited oxide.

TABLE 11: Oxidation data for Ni-25Cr and Ni-25Cr(coated oxide) after 100 hours at 1100°C.

Deposited Oxide	Weight gained from oxidation	Weight spalled from cooling
Ni-25Cr	2.89	1.74
Ni-25Cr(Hf)	3.14	3.11
Ni-25Cr(Cr)	2.30	1.87
Ni-25Cr(Ca)	4.09	0.89
Ni-25Cr(Zr)	2.31	2.68
Ni-25Cr(La)	0.63	0.20*
Ni-25Cr(Y)	0.60	0.23*
Ni-25Cr(Ce)	0.94	0.38*

* Spallation came entirely from the sides of the specimen which were not coated with the reactive element oxide.
All figures are in units of mg/cm^2.

TABLE 12: Summary of oxidation data for Ni-25Cr and Ni-25Cr(ion-implanted) after 50 hours at 1000°C in 1 atm. O_2.

Specimen	Weight gained from oxidation (mg/cm^2)	Weight spalled from cooling (mg/cm^2)	Approximate k_p ($mg^2\ cm^{-4}\ sec^{-1}$)
Ni-25Cr	1.61 ± 0.14	0.05 ± 0.01	$(1.6 \pm 0.3)\times10^{-5}$
Ni-25Cr(1×10^{15} Y^+)	1.33	0.17	1.2×10^{-5}
Ni-25Cr(5×10^{15} Y^+)	1.03	0.14	5.0×10^{-6}
Ni-25Cr(1×10^{16} Y^+)	1.04	0.10	4.7×10^{-6}
Ni-25Cr(5×10^{16} Y^+)	0.46	0	6.9×10^{-7}
Ni-25Cr(5×10^{16} Y^+ preox.)	0.59	0.08	6.7×10^{-7}
Ni-25Cr(5×10^{16} Xe^+)	1.94	0.43	1.0×10^{-5}

Figure Captions

Figure 1 - Schematic illustration of how dispersoid oxide particles, by acting as nucleation sites for the first-formed oxide, accelerate the approach to steady-state and reduce the amount of Nickel-containing oxides formed: a) without and b) with dispersed oxide particles.

Figure 2 - Surface topography of various nitrate converted oxide coats.

Figure 3 - Morphology of deposited thin cerium oxide prior to oxidation (viewed by BSE mode).

Figure 4 - Simplified schematic illustration of the injector and beam line used for ion-implantation.

Figure 5 - Schematic illustration of the specimen holder assembly. Ion beam travels through the collimator, perpendicular to the plane of the drawing.

Figure 6 - Rutherford backscattering analysis of three different areas on a La^{2+} implanted ($1x10^{16}/cm^2$) Ni-25Cr surface.

Figure 7 - Auger depth profile of a Y^{+} implanted ($1x10^{18}/cm^2$) Co-25Cr alloy prior to any oxidation treatments. Sputtering rate is approximately 2500 nm/min.

Figure 8 - Kinetics curves showing the effect of Y_2O_3 coatings on the oxidation behavior of a Co-15Cr alloy at 1000°C in 1 atm O_2. The numbers in parentheses are the amounts of Y_2O_3 in mg/cm^2 applied prior to oxidation.

Figure 9 - A backscattered electron image of a fractured cross-section of scales formed on a) an untreated Co-15Cr alloy and b) a HfO_2-treated Co-15Cr alloy oxidized at 1000°C in 1 atm O_2. Since the tilt angles were different for the two specimens, direct comparison of scale thickness from these micrographs should not be made.

Figure 10 - a) SEM image showing the top surface of a Y_2O_3-treated Co-15Cr alloy oxidized at 1000°C for 24 minutes. b) and c) are magnified views of areas a and b in (a) respectively.

Figure 11 - Kinetics curves for the uncoated Co-25Cr alloy and for the same alloy coated with different amounts of La_2O_3 prior to oxidation in 1 atm. O_2 at 1000°C. The numbers in parentheses are the weight of the deposited La_2O_3 in mg/cm^2.

Figure 12 - The effect of different surface-applied oxides at a surface coverage of approximately 0.3 mg/cm^2 on the oxidation kinetics of the Co-25Cr alloy oxidized at 1000°C in 1 atm. O_2.

Figure 13 - Optical micrographs of the scale developed on the untreated Co-25Cr alloy. a) General scale appearance after 24 hours at 1000°C in 1 atm. O_2. b) Magnified view from part of (a), showing areas with a more complete Cr_2O_3 healing layer at the scale/alloy interface. c) Regions of protective thin scales. d) Scale appearance after 3 hours at 1000°C showing a higher percentage of the protective thin scale.

Figure 14 - Optical micrographs of scales formed on a) HfO_2-treated and b) ZrO_2-treated Co-25Cr alloys after 24 hours at 1000°C. The CeO_2-treated specimens appeared very similar to the ZrO_2-treated ones.

Figure 15 - a) SEM image of the surface oxide formed on a Y_2O_3-treated Co-25Cr alloy oxidized at 1000°C for 24 hours. EDX analysis of the thin oxide showed that it is rich in Y and Cr. b) an optical micrograph of a cross-section of the scale on the same specimen.

Figure 16 - Morphology of the Cr-rich protective scale which almost entirely covered the CaO-treated Co-25Cr alloy. a) Optical micrograph of the scale. b)-e) SEM image and component distribution within this thin protective scale.

Figure 17 - SEM image and X-ray maps of the cross-section of an area of scale formed on the bottom of a CaO-treated Co-25Cr alloy oxidized at 1000°C for 24 hours.

Figure 18 - Corrected weight gain vs. time plot for various ion-implanted Co-25Cr alloys oxidized in 1 atm. O_2 at 1000°C. The kinetics of unimplanted Co-25Cr and the yttrium bulk alloyed Co-25Cr-1Y are included for comparison. The numbers in parentheses

are the implantation dosage in ions/cm^2.

Figure 19 - Kinetics behavior of Co-25Cr ($1x10^{18}$ Y^+/cm^2) after a longer oxidation time (50 hours) at 1000°C.

Figure 20 - An example showing the excess spallation from the implanted surface after oxidation. a) Schematic drawing of the relative areas of implanted vs. unimplanted surfaces before oxidation. b) The appearance of the specimen: Co-25Cr ($1x10^{16}$ Y^+) after 50 hours at 1000°C.

Figure 21 - Typical scale morphology developed on the Co-25Cr-1Y alloy after 24 hours at 1000°C. a) an optical micrograph of the cross sectioned scale. b) and c) are SEM image and corresponding EDX line scans of Cr, Co and Y across the scale.

Figure 22 - Different scale morphologies observed on the Co-25Cr ($1x10^{16}$ Y^+) specimen after 24 hours at 1000°C. a) Thin protective scale with a healing Cr_2O_3 layer. b) and c) Large nodular Co-rich scales.

Figure 23 - Morphology of the scale formed on the Co-25Cr ($3x10^{17}$ Y^+) specimen after 24 hours at 1000°C. a) Cr-rich protective type scale. b) A large nodule growing through single layer Cr_2O_3. c) an area with continuous Cr_2O_3 scale formation with overgrowth of cobalt oxides.

Figure 24 - Surface topography of Co-25Cr ($1x10^{18}$ Y^+) after 24 hours at 1000°C. a) Interfacial area between implanted and unimplanted regions. b) Magnified view of the implanted region. c) EDX analysis of the scale formed on the implanted region.

Figure 25 - Tapered cross section (40 degrees) of the scale formed on the same specimen as that shown in Figure 24. a) Optical micrograph showing the implanted/unimplanted interface. b) SEM image of the scale formed on the implanted region using backscattered electrons. c) Magnified view of the scale shown in (b).

Figure 26 - SIMS depth profiles of Cr, Co and Y through the scale formed on the same specimen as that shown in Figure 24.

Figure 27 - a) Surface oxides formed on Co-25Cr implanted with $1x10^{18}$ Y^+ after 4 hours of oxidation at 1000°C. b) Magnified area of (a) viewed with backscattered Auger electrons. c) and d) are Auger depth profiles of O, Cr, Co and Y form points 1 and 2 marked in (b) respectively. The sputtering rate was approximately 2500 nm/min.

Figure 28 - Surface topography of scales formed on Co-25Cr ($1x10^{18}$ Y^+) after 50 hours of oxidation at 1000°C. a) Interfacial area between implanted and nonimplanted regions. b) Magnified view of grains on the implanted region.

Figure 29 - Auger surface survey of the implanted ($3x10^{17}$ Y^+) Co-25Cr before internal oxidation pretreatment. a) As-implanted surface. b) Surface after 15 second sputtering. The sputtering rate was approximately 2500 nm/min.

Figure 30 - An Auger analysis similar to that of Figure 29 except that the specimen had undergone an internal oxidation pretreatment for 2 hours at 1000°C. a) Surface survey after internal oxidation pretreatment. b) Surface survey after 30 seconds sputtering using Ar.

Figure 31 - Continuous SIMS depth profiles of Y^+, YO^+, and O^- on implanted Co-25Cr ($1x10^{17}$ Y^+) before and after internal oxidation pretreatment. Sputtering was carried out using Ar with an approximate rate of 2500 nm/min.

Figure 32 - The effect of internal oxidation pretreatment on the oxidation kinetics of Co-25Cr, Co-25Cr-1Y and Co-25Cr ($3x10^{17}$ Y^+). The numbers in parentheses indicate the duration of internal oxidation treatment in hours.

Figure 33 - a) Weight gain vs. time behavior for the first hour of oxidation of the Co-25Cr ($3x10^{17}$ Y^+) specimen before and after the internal oxidation pretreatment. b) Surface topography of the scale formed on the I.O. pretreated Co-25Cr ($3x10^{17}$ Y^+) after 30 minutes at 1000°C.

Figure 34 - Morphology of the scale developed on the I.O. pretreated Co-25Cr-1Y alloy after 24 hours at 1000°C. a) Optical micrograph showing the internal oxidation of Y ahead

of the scale. b) Magnified area of scale in (a) viewed under SEM. c) and d) are EDX Cr and Co maps respectively.

Figure 35 - SEM micrograph of oxide scale formed on Co-25Cr alloy oxidized in 10-30 torr O_2 for 15 hours. a) shows the high degree of spallation of the scale after cooling. b) Magnified view of the spalled area. c) and d) show the morphology of the unspalled oxide which is highly convoluted.

Figure 36 - Kinetics curves for Ni-25Cr alloys coated with various reactive element oxides oxidized at 1000°C in 1 atm. O_2. The curve indicated by (-) represents the untreated Ni-25Cr.

Figure 37 - Influence of deposited thin CeO_2 coating upon a) the kinetics of oxidation and b) the oxide spallation from thermal cycling of the Ni-25Cr alloy at 1000°C in 1 atm. O_2.

Figure 38 - Influence of deposited CeO_2 and Y_2O_3 upon a) the kinetics of oxidation and b) the oxide spallation from thermal cycling (20-hour cycles) of the Ni-25Cr at 1100°C in 1 atm. O_2.

Figure 39 - SEM image and Ni and Cr maps of the cross-sectioned scale formed on an untreated Ni-25Cr alloy oxidized at 1000°C for 24 hours.

Figure 40 - a) SEM image of the scale formed on a HfO_2-treated Ni-25Cr alloy oxidized at 1000°C for 100 hours. b)-d) are Cr, Ni and Hf X-ray maps respectively. e) Backscattered electron image of the scale formed on the same specimen.

Figure 41 - SEM image and X-ray maps showing the morphology and component distribution of the scale formed on a Y_2O_3-treated Ni-25Cr alloy oxidized at 1000°C for 100 hours. A is an oxide nodule growing out of the original Y_2O_3 deposit.

Figure 42 - a) Backscattered electron image of a CeO_2-treated scale formed on the Ni-25Cr alloy oxidized at 1000°C for 100 hours. A are CeO_2 particles and B are Cr_2O_3 grains growing above the deposited CeO_2. b) Backscattered electron image showing the detached CeO_2 coat on the polished scale.

Figure 43 - a) SEM image of surface oxide grains formed on a CeO_2-treated Ni-25Cr alloy after 50 hours at 1000°C. b) the same area as in (a), imaged under BSE mode. c) SIMS depth profile through the oxide scale, starting from the scale outer surface.

Figure 44 - a) Morphology of oxide grains at the underside of the scale formed on the specimen shown in Figure 43. b) Similar grains viewed under BSE mode. Arrows point to brighter particles which are CeO_2. c) Continuous SIMS mass 140 trace through the scale, starting from the oxide underside.

Figure 45 - Morphology of oxide at the underside of the scale formed on a ZrO_2-treated Ni-25Cr oxidized at 1000°C for 50 hours. Arrows point to Zr rich particles identified by EDX.

Figure 46 - The scale formed on a Y_2O_3-treated Ni-25Cr after 100 hours at 1100°C. Alloy substrate had been etched away with Br_2/MeOH.

Figure 47 - A fracture cross section of the scale from a) Ni-25Cr oxidized at 1100°C for 100 hours. b) Y_2O_3-treated Ni-25Cr oxidized under the same conditions. Some Y rich particles are seen within the scale as indicated by EDX.

Figure 48 - SEM-BSE photographs of cross sectioned scales on Y_2O_3-treated Ni-25Cr specimens with Pt markers. In a) the Pt was deposited onto the Y_2O_3 coat and in b) the Pt was deposited unto the Ni-25Cr alloy, laying between the alloy and the subsequently deposited surface Y_2O_3. Both specimens were oxidized at 1000°C for 50 hours.

Figure 49 - The weight gain behavior of various ion-implanted Ni-25Cr specimens as a function of time at 1000°C.

Figure 50 - Influence of two different dosages of yttrium-implantation on a) the kinetics of oxidation and b) the oxide spallation from thermal cycling of the Ni-25Cr alloy at 1100°C.

Figure 51 - Appearance of an annealed specimen which contains an unimplanted area, a $1x10^{16}$ Y^+-implanted area and a $5x10^{16}$ Y^+-implanted area after each thermal cycle (20 h)

at 1100°C. Annealing was carried out at 700°C in vacuum for 5 hours.

Figure 52 - Surface topography of oxide formed on the Ni-25Cr specimen implanted with $5x10^{16}$ yttrium on a preformed oxide surface after 50 hours of subsequent oxidation at 1000°C. a) shows the interface between the implanted and the unimplanted surfaces. b) and c) are magnified views of the unimplanted and the implanted surfaces respectively along with EDX analysis of these surface oxides.

Figure 53 - a) Surface topography of the Xe^+-implanted surface after 50 hours at 1000°C. b) Magnified view of a spalled area showing many interfacial voids and areas of no scale/metal contact. c) A piece of fratured scale showing the porous nature of the scale.

Figure 54 - a) Morphology of surface oxide grains formed on the $5x10^{16}$ yttrium-implanted specimen. b) Scale structure shown by a piece of fractured scale. c) and d) are surface topography of scales formed on $5x10^{15}$ and $1x10^{15}$ yttrium implanted specimens respectively.

Figure 55 - Underside of the scales formed after 50 hours of isothermal oxidation at 1000°C on a) $5x10^{16}$, b) $5x10^{15}$, c) $1x10^{15}$ yttrium-implanted, d) unimplanted, e) $5x10^{16}$ Y^+-implanted onto a preformed oxide and f) $5x10^{16}$ Xe^+-implanted surfaces.

Figure 56 - Comparison of grain sizes found on the underside of scales formed on a) $5x10^{16}$ Y^+ and b) $5x10^{15}$ Y^+-implanted specimens after 50 hours of oxidation at 1000°C.

Figure 57 - Optical micrographs of cross sectioned scales formed on a) Xe^+-implanted b) $1x10^{15}$ c) $1x10^{16}$ d) $5x10^{16}$ Y^+-implanted and e) $5x10^{16}$ Y^+-implanted on preoxidied surface after 50 hours at 1000°C.

Figure 58 - SEM micrographs of the same cross sectioned scales shown in Figure 57 after the underlying alloy had been deep etched by Br_2/MeOH. a) and b) are scales formed with $5x10^{16}$ Y^+-implantion on untreated Ni-25Cr alloy surface and on preoxidized alloy surface respectively. c) is the magnified view of the fractured section of the

scale shown in (b).

Figure 59 - Surface topography of oxides formed on three surfaces: $1x10^{16}$ Y^+-implanted, unimplanted and $5x10^{16}$ Y^+-implanted after a) 15 minutes c) 60 minutes and d) 300 minutes of oxidation at 1000°C. b) is a magnified view of the interface between unimplanted and $5x10^{16}$ Y^+-implanted regions after 15 minutes of oxidation.

Figure 60 - SIMS depth profiles starting from scale top surfaces to the alloy on various ion-implanted specimens after 50 hours at 1000°C.

Figure 61 - Schematic illustration of possible scale growth processes on the specimen with $5x10^{16}$ Y^+-implanted on a preoxidized surface.

Figure 62 - Schematic illustration of the possible mechanism involved with HfO_2 surface deposits on the oxidation behavior of the Ni-25Cr alloy.

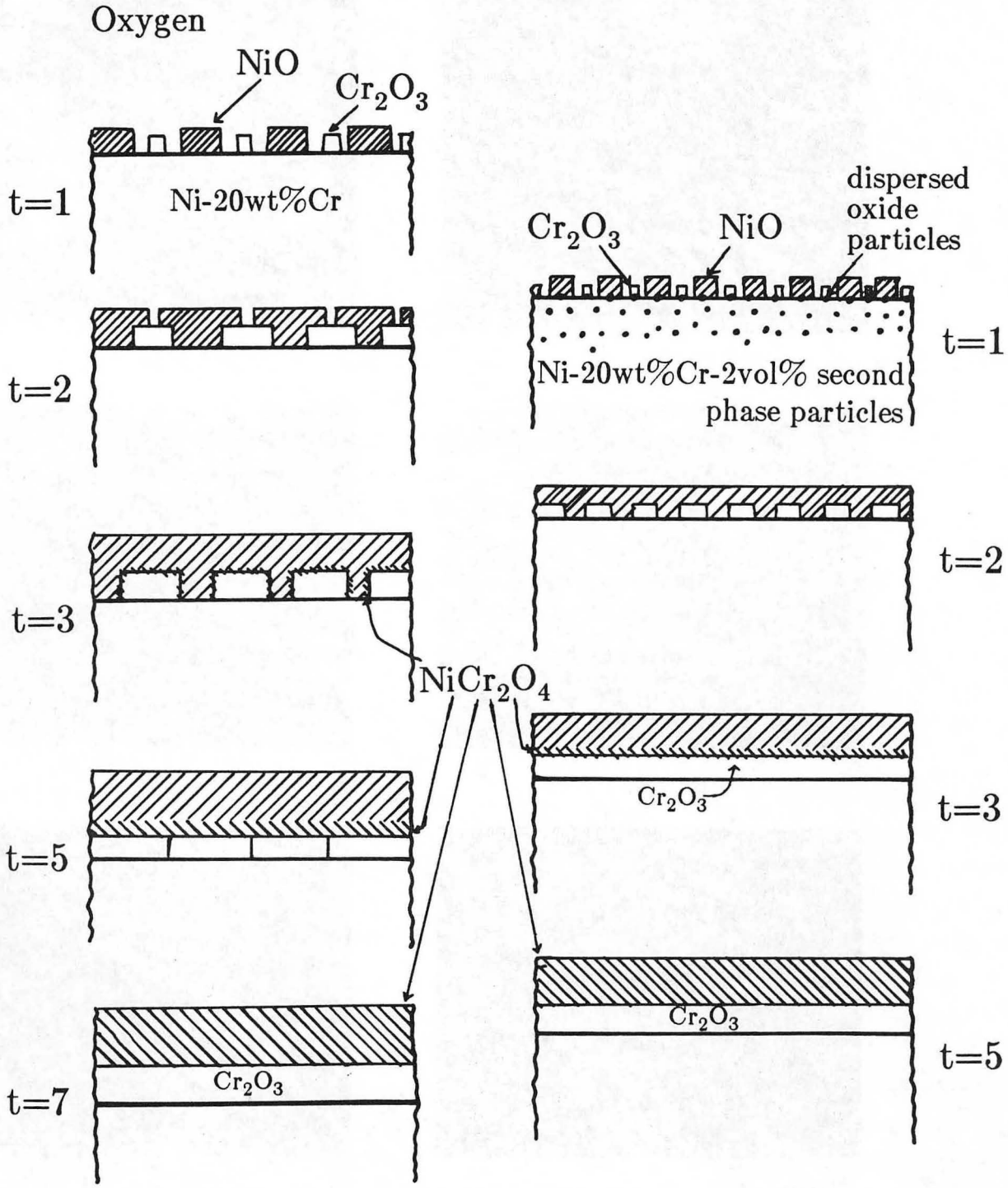

(a) without particles (b) with particles

Figure 1

XBL 8612-4795

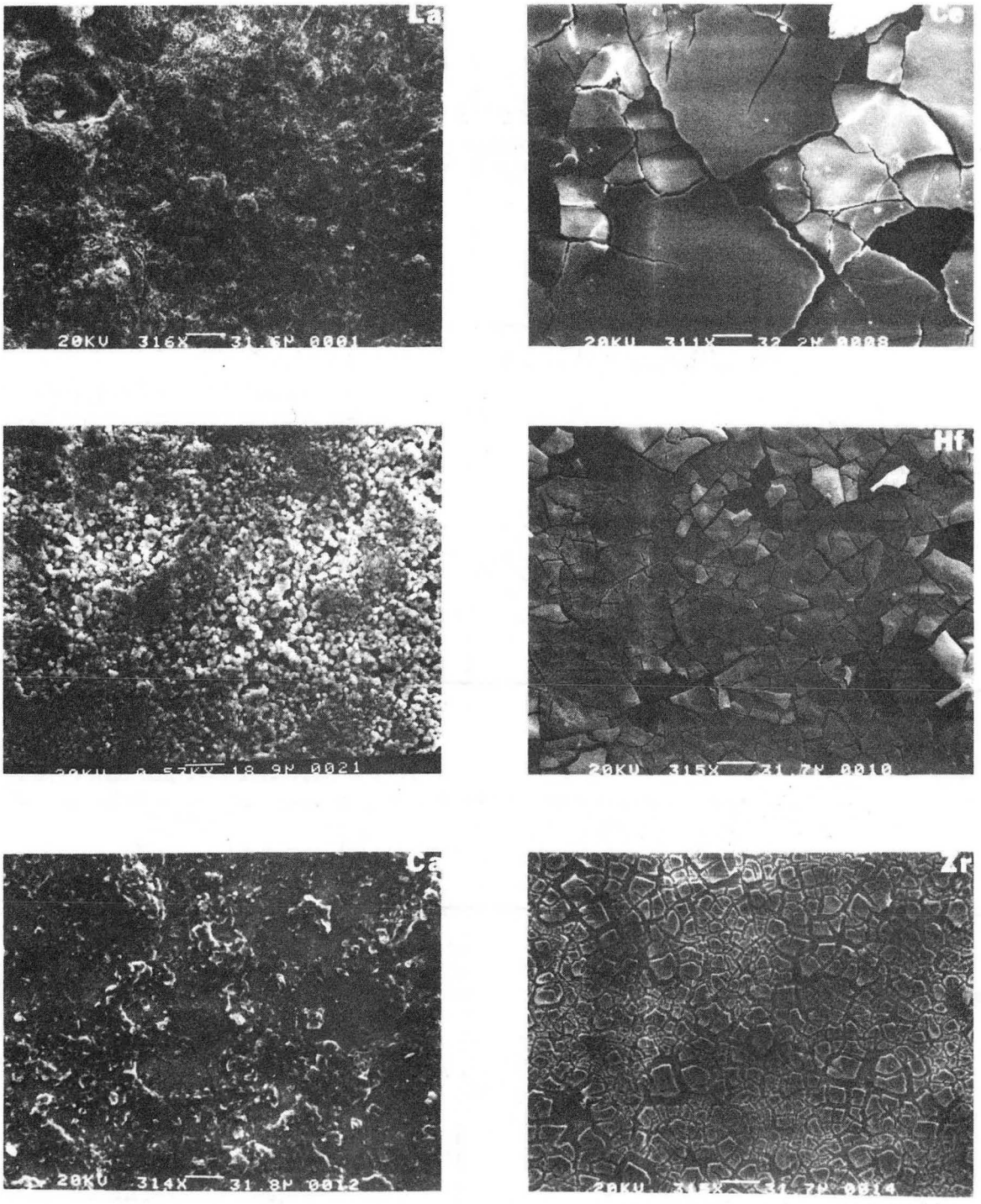

Figure 2

XBB 854-2644A

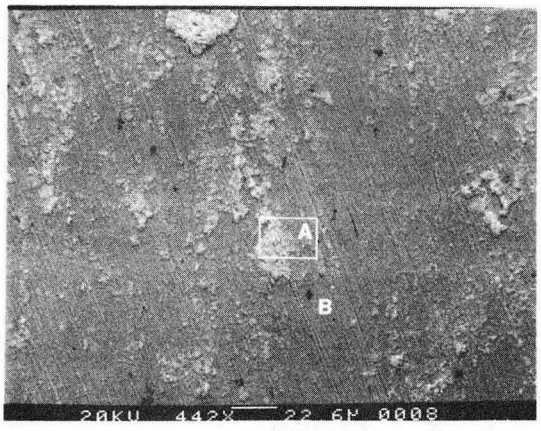

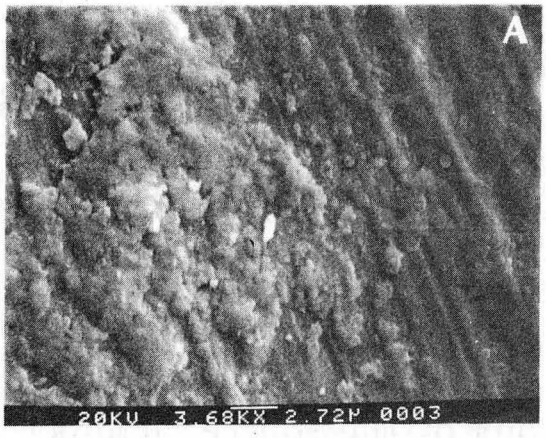

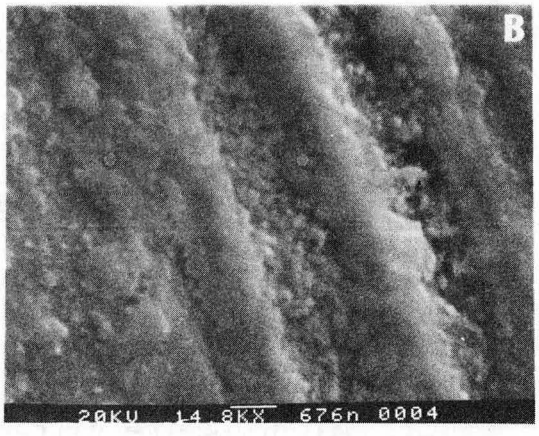

Figure 3

XBB 854-2894

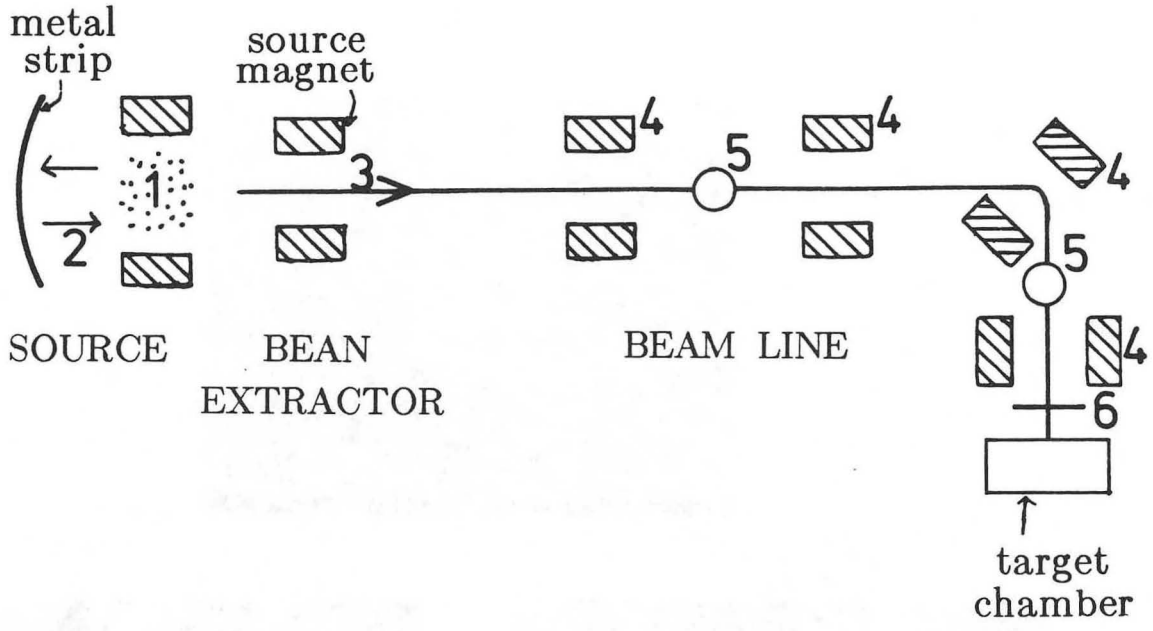

XBL 8612-4796

1. A plasma of inert gas is created by the source magnets.
2. Ionized gas sputters the metal source to release metal ions into the plasma.
3. All ions are attracted out of the source chamber to the beam line.
4. Four sets of quadrupoles focus the beam and select the desired ions.
5. Faraday cups along the line to read the beam current
6. An adjustable TV panel for visual observation of the beam

Figure 4

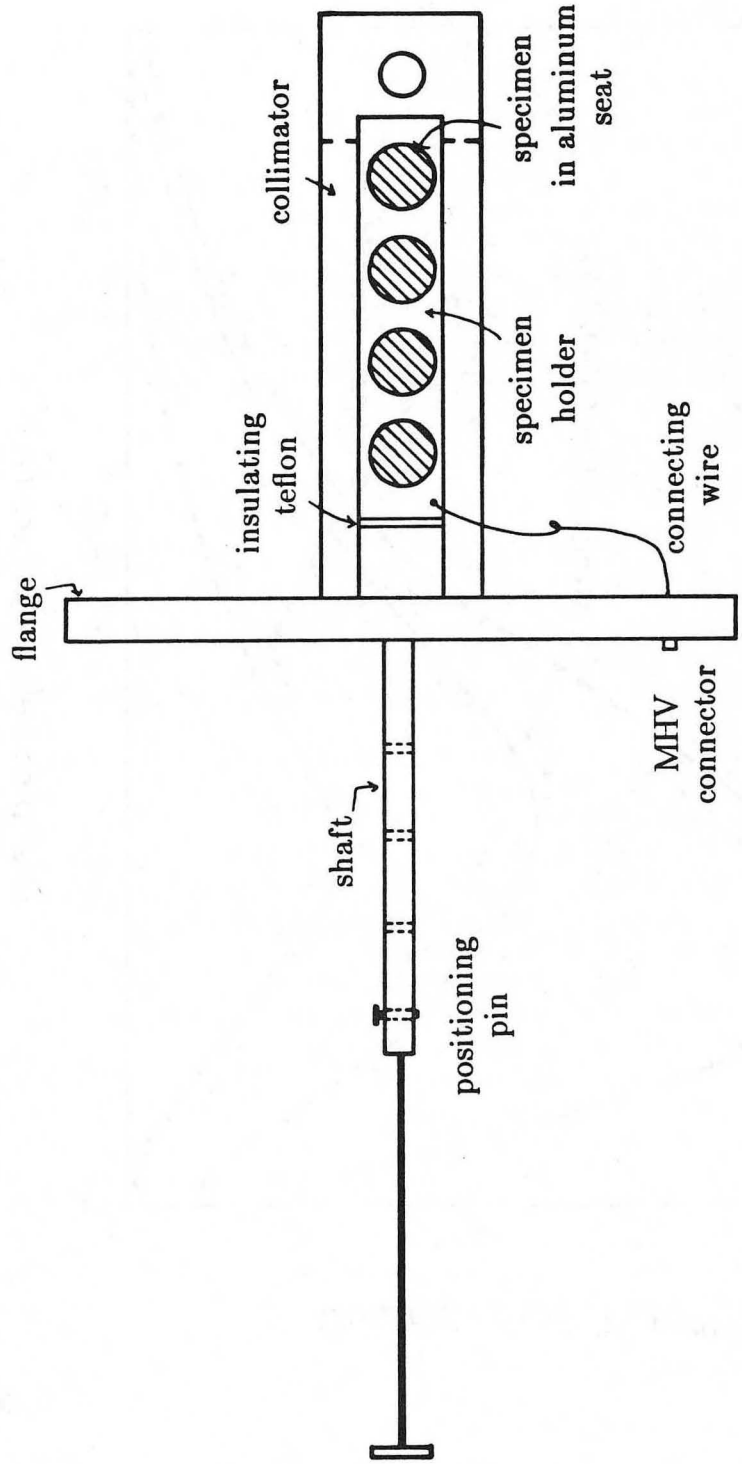

Figure 5

XBL 8612-4797

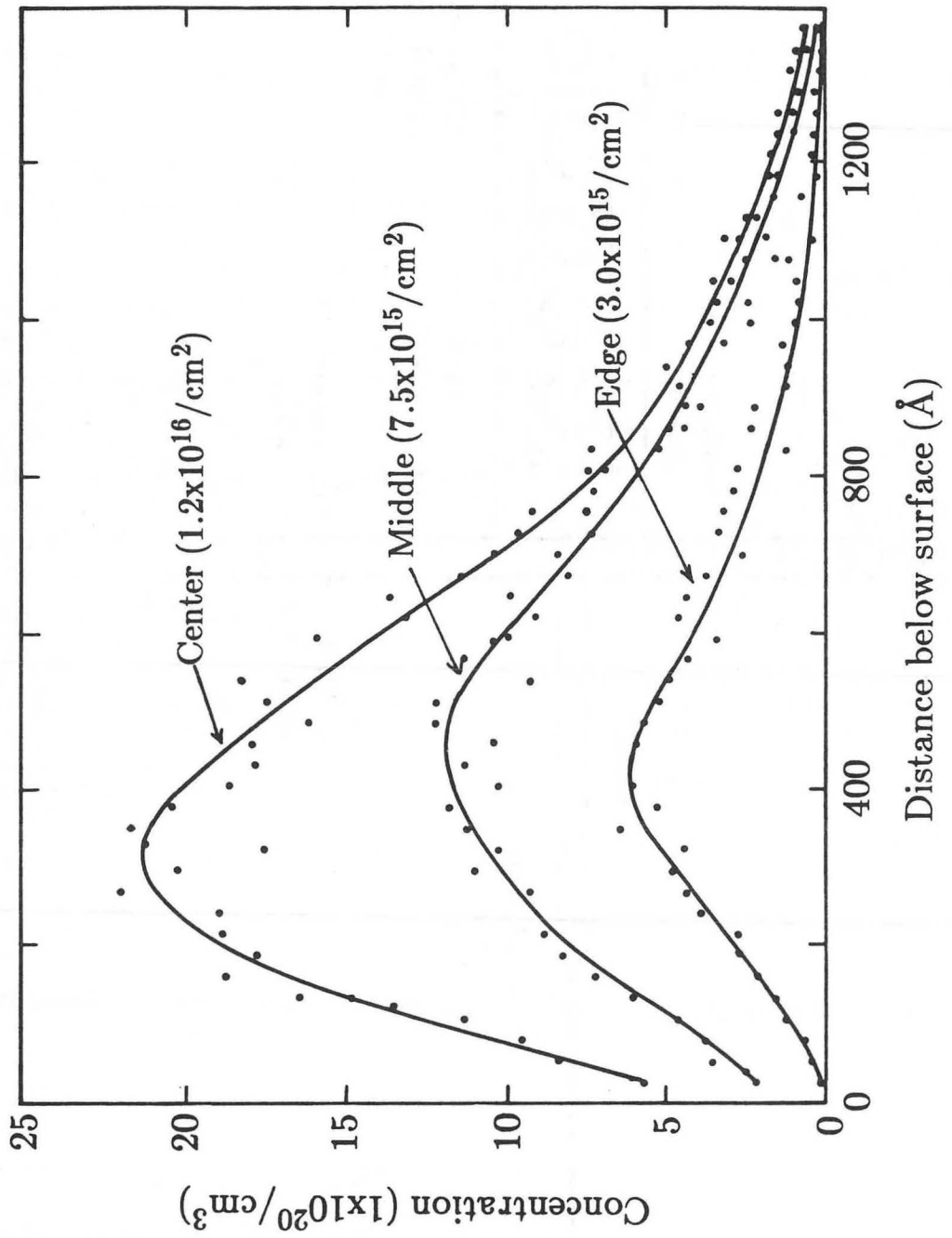

Figure 6

XBL 8612-4798

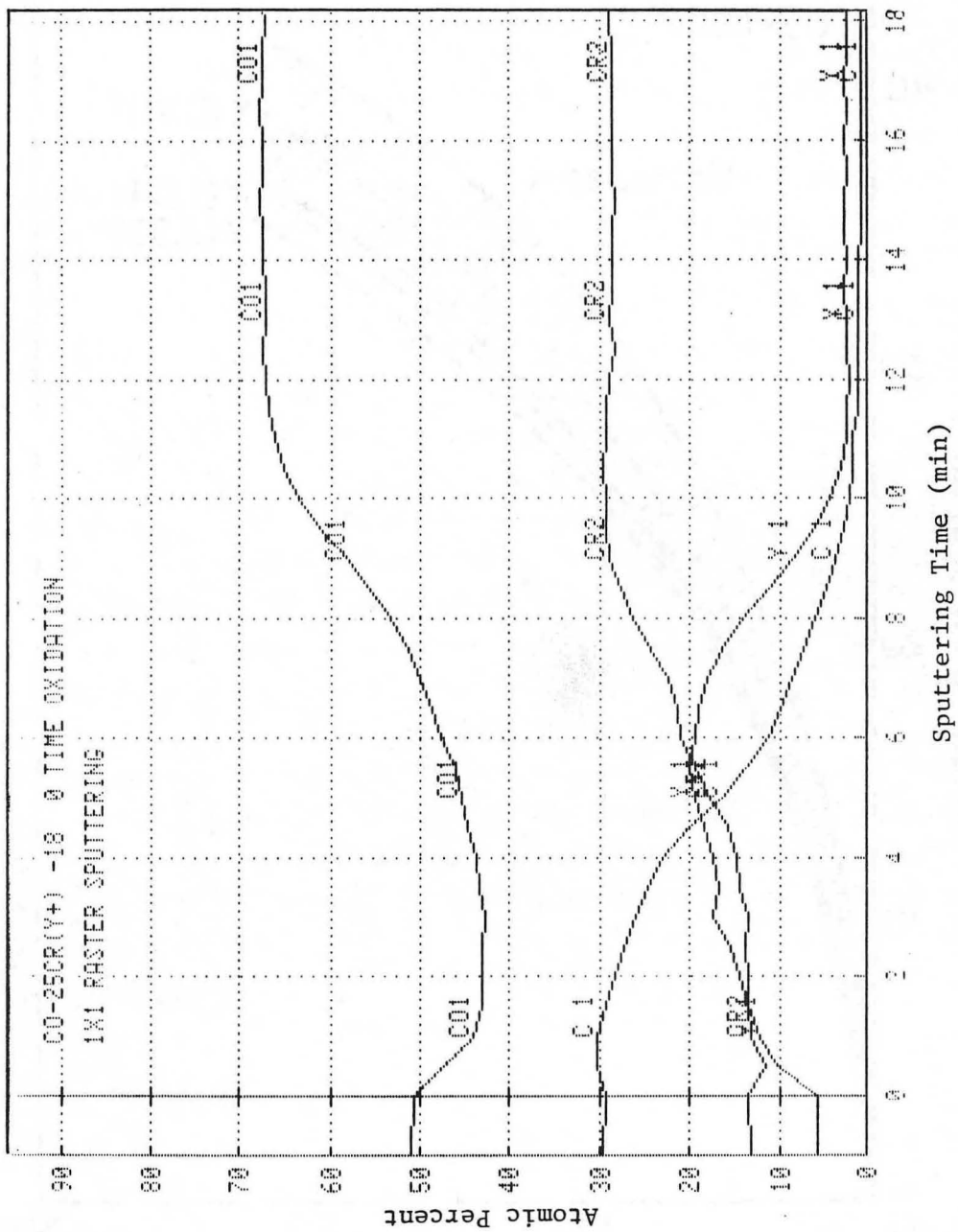
CO-25CR(Y+) -10 0 TIME OXIDATION
1X1 RASTER SPUTTERING
Atomic Percent
Sputtering Time (min)
CO1
CR2
Y 1
C 1

Figure 7

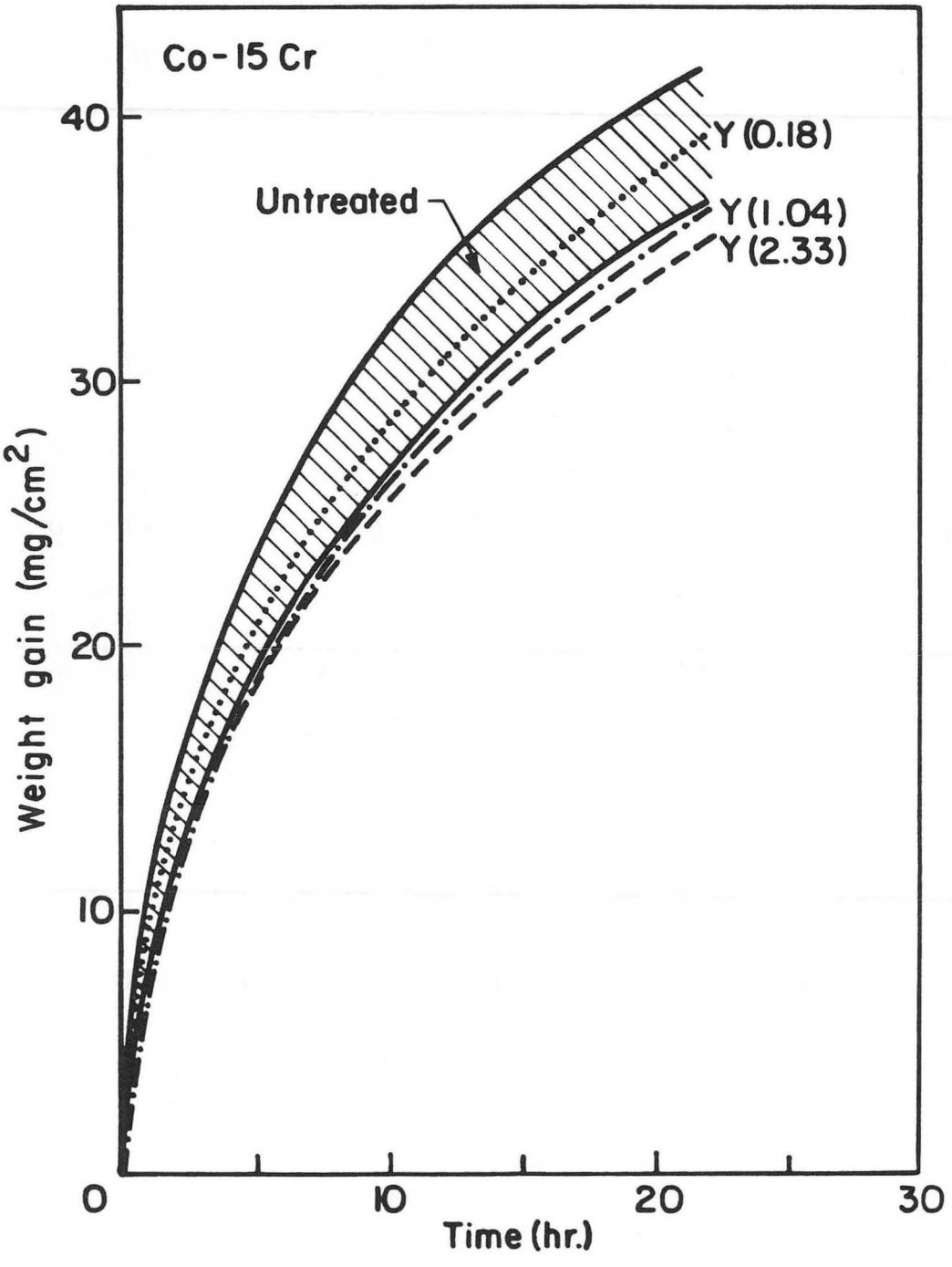
Co-15 Cr
Y (0.18)
Untreated
Y (1.04)
Y (2.33)
Weight gain (mg/cm²)
Time (hr.)
0
10
20
30
40
XBL 858-6584

Figure 8

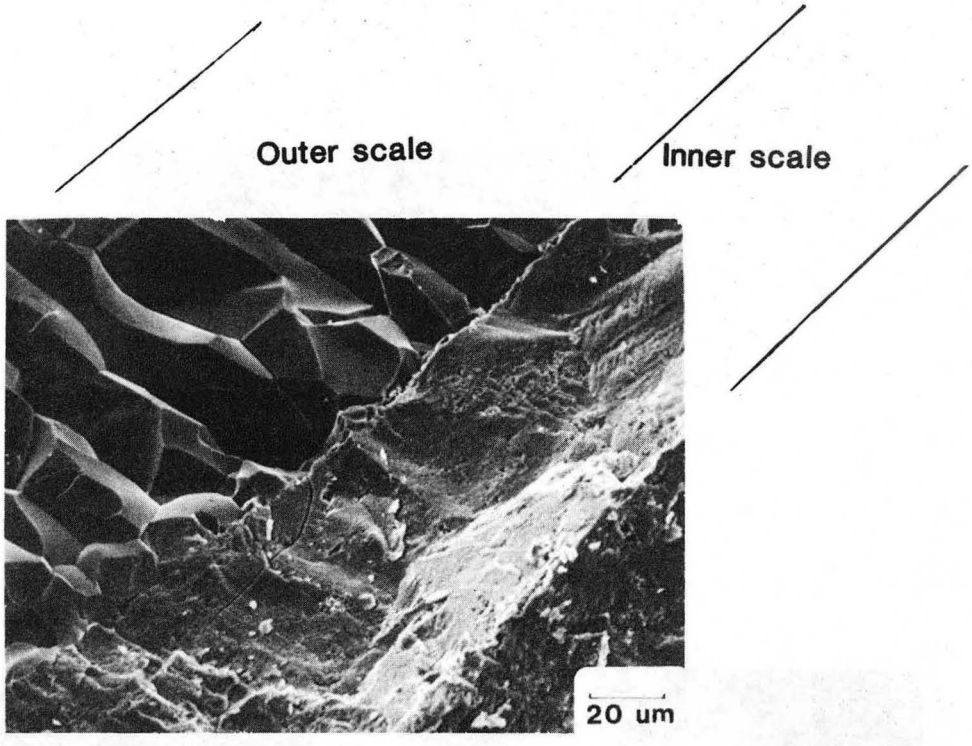

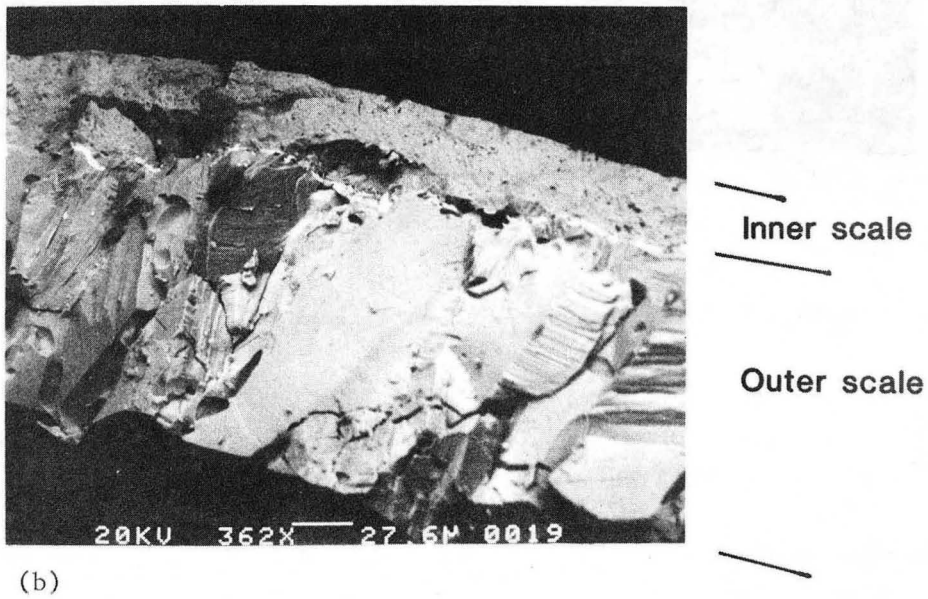

(b)

Figure 9

XBB 854-2633

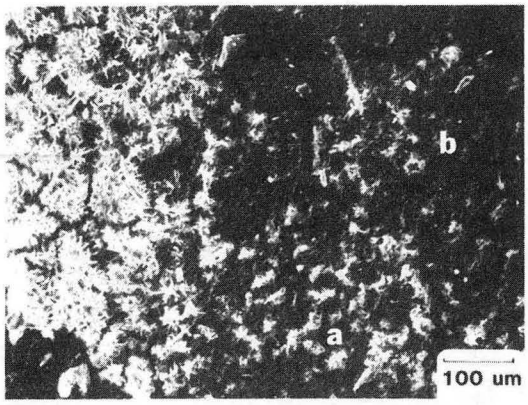

(a)

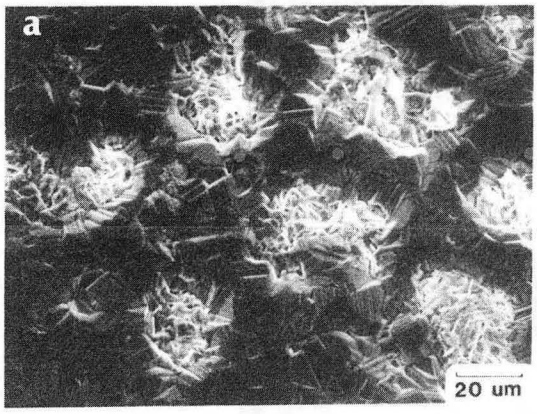

(b)

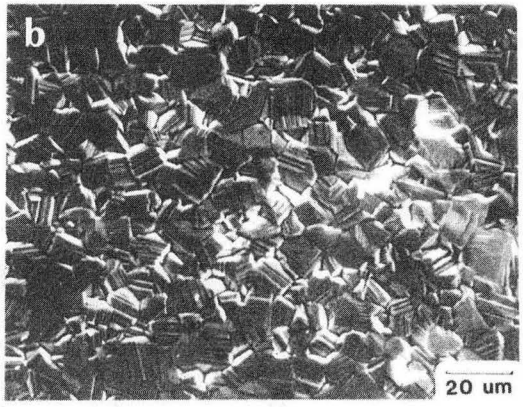

(c)

Figure 10

XBB 854-2641

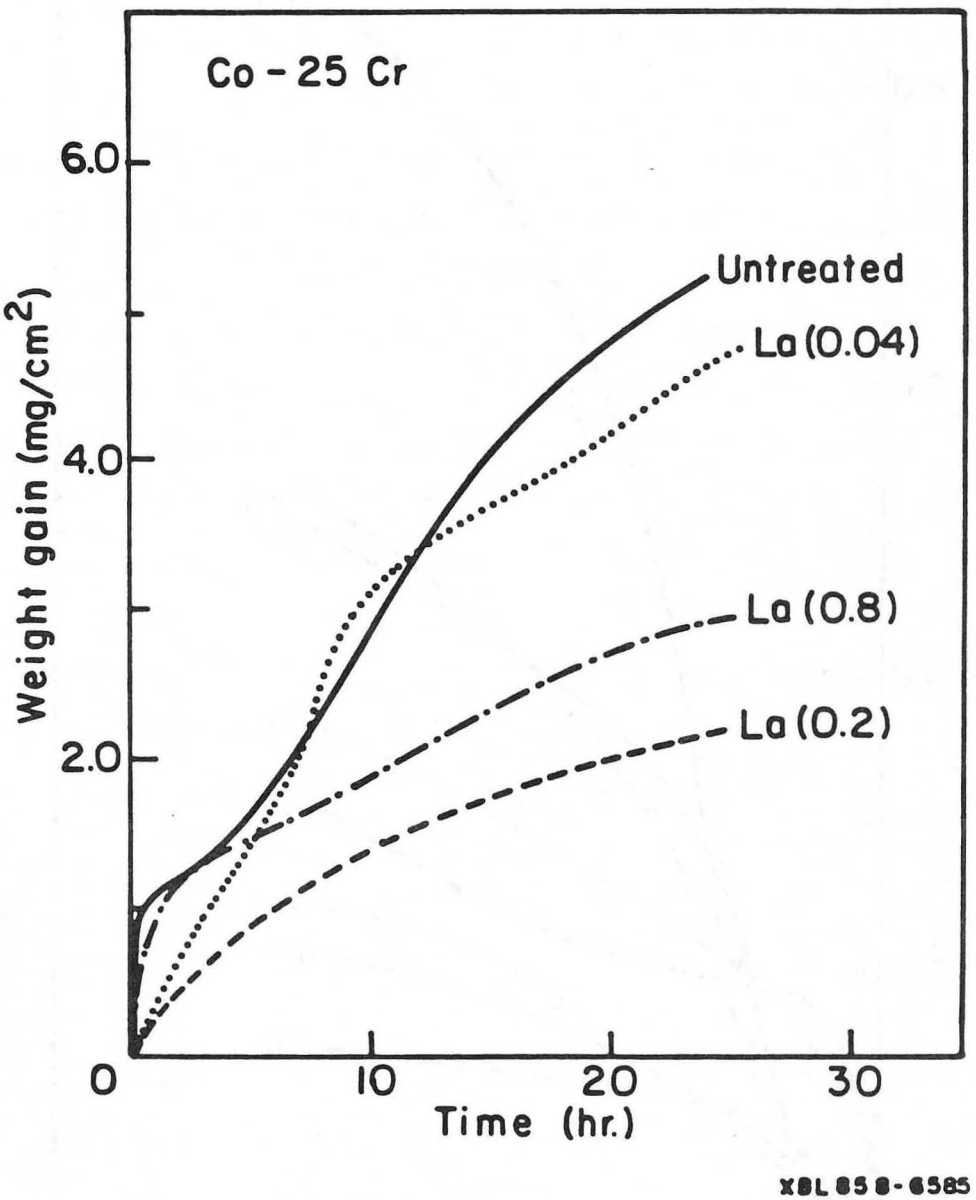
Co - 25 Cr
6.0
4.0
2.0
0
Weight gain (mg/cm²)
Untreated
La (0.04)
La (0.8)
La (0.2)
10
20
30
Time (hr.)
XBL 858-6585

Figure 11

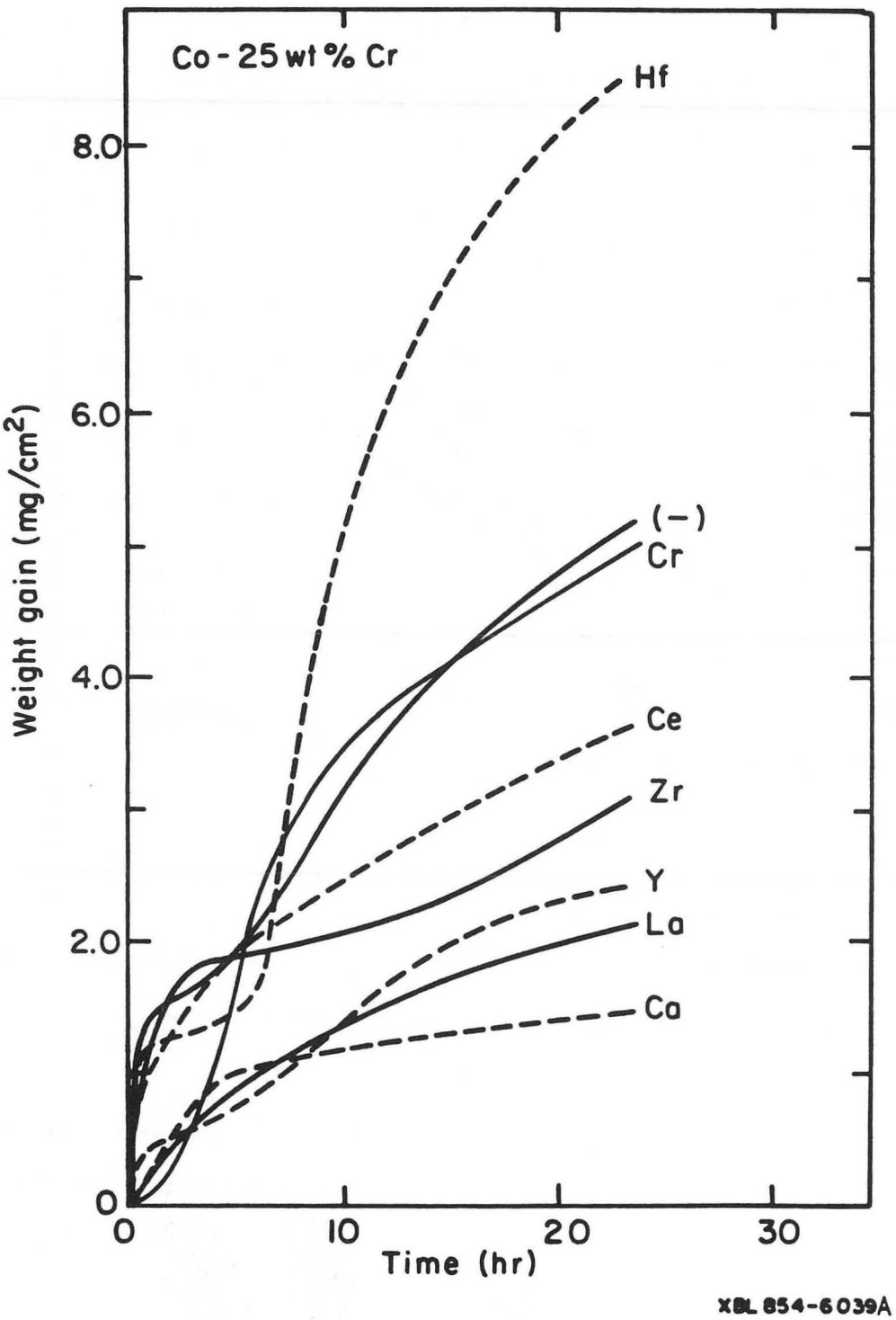
Co - 25 wt % Cr
Hf
(-)
Cr
Ce
Zr
Y
La
Ca
Weight gain (mg/cm²)
8.0
6.0
4.0
2.0
0
0
10
20
30
Time (hr)
XBL 854-6039A

Figure 12

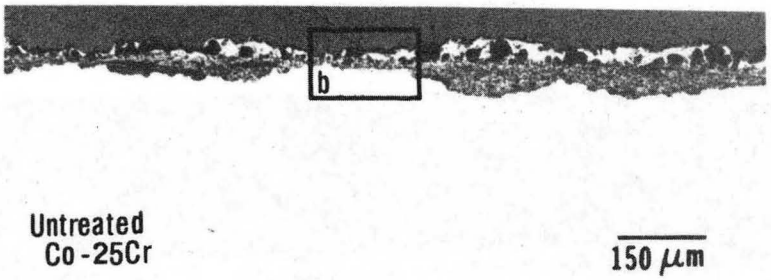

(a)

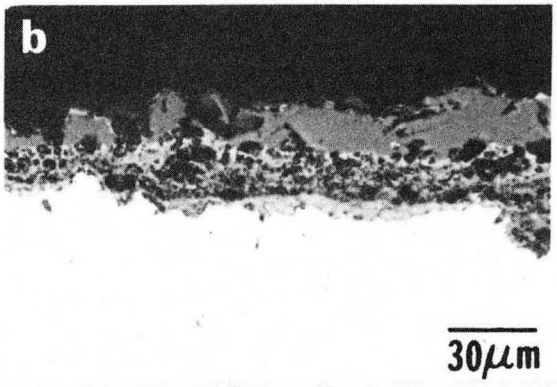

(b)

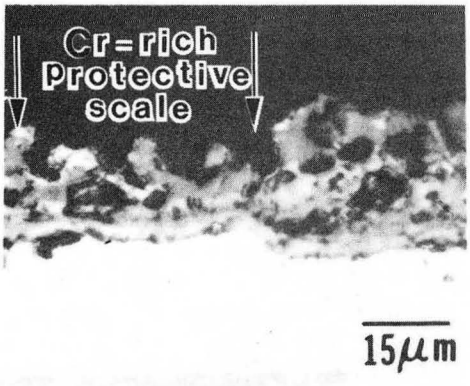

(c)

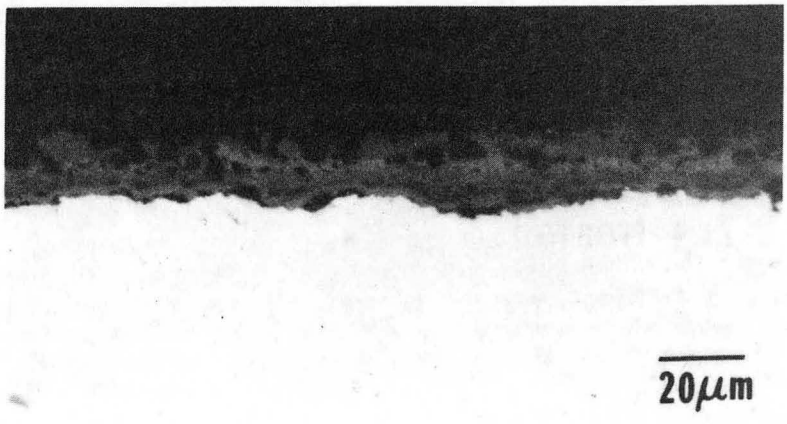

(d)

Figure 13

XBB 860-8772

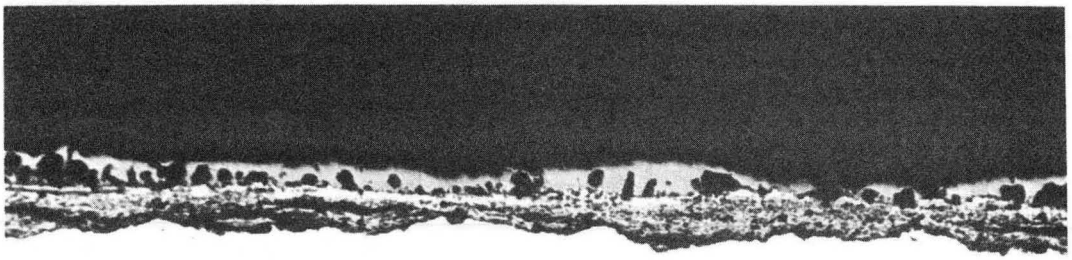

(a)

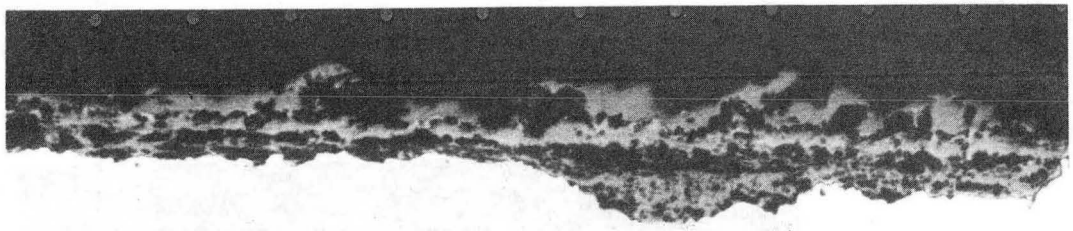

(b)

Figure 14

XBB 860-8774

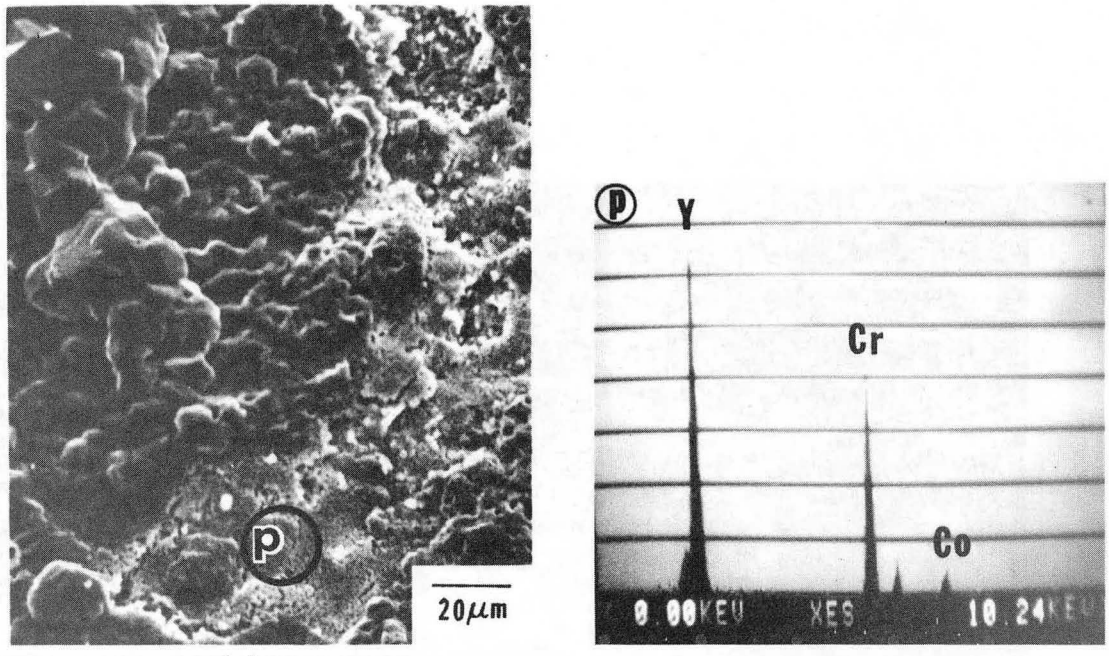

(a)

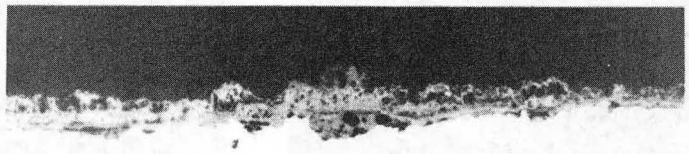

(b)

Figure 15

XBB 860-8773

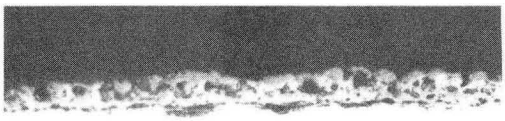

Ca – treated

20 μm

(a)

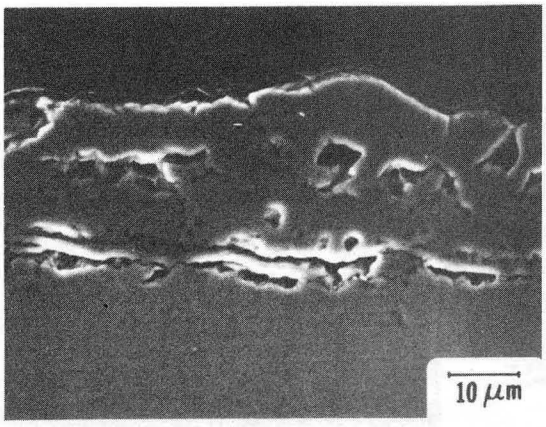

(b)

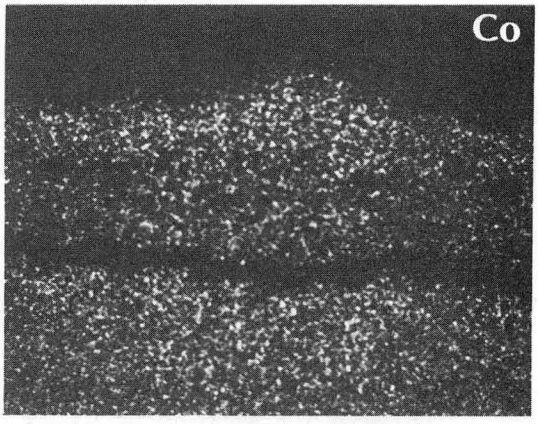

(c)

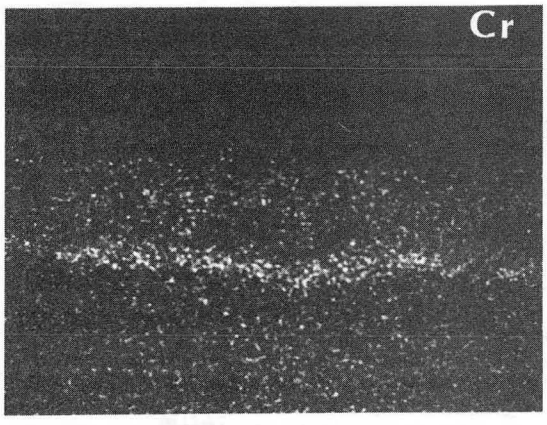

(d)

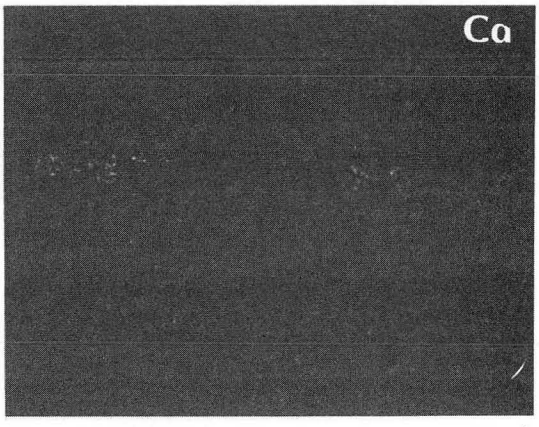

(e)

Figure 16

XBB 860-8776

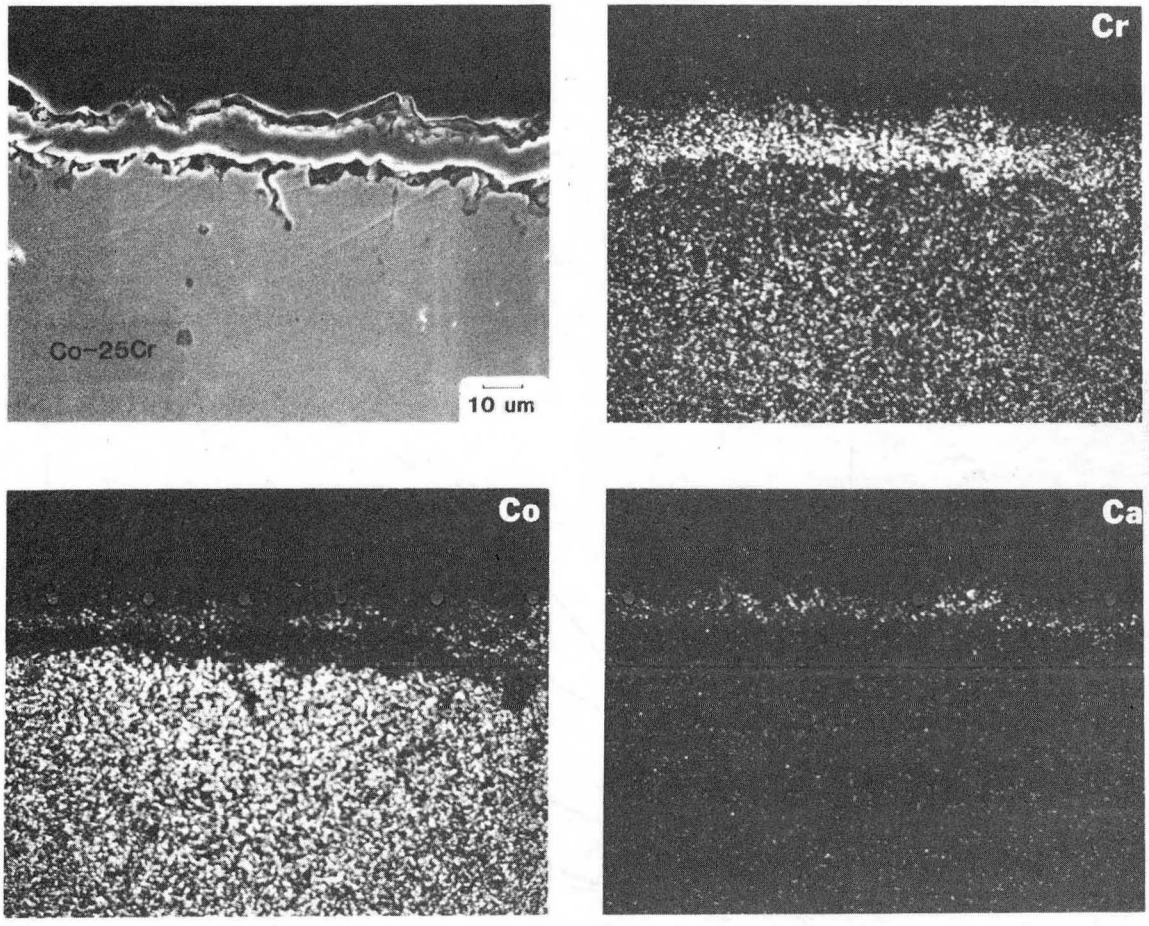

Figure 17

XBB 854-2637

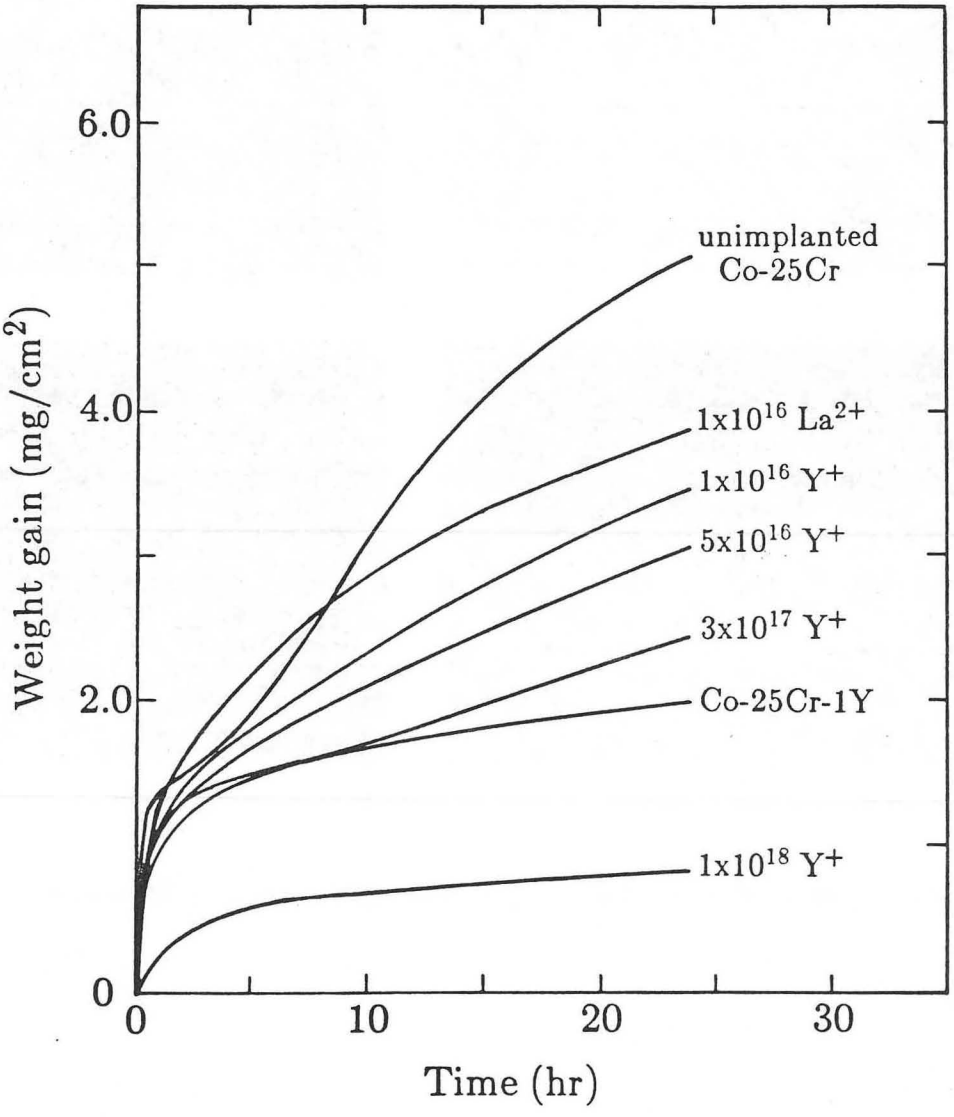

Figure 18

XBL 8612-4799

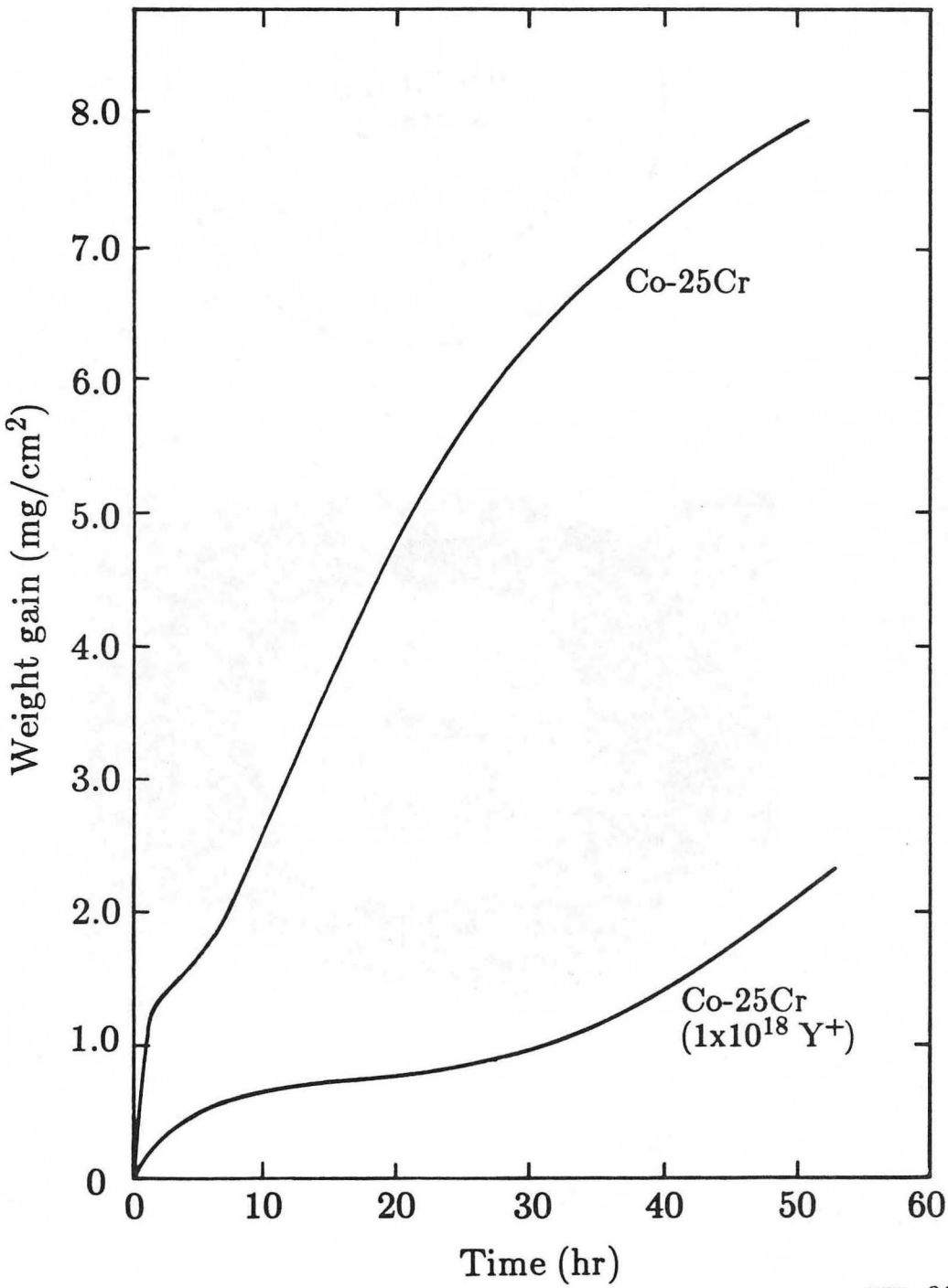

Figure 19

XBL 8612-4800

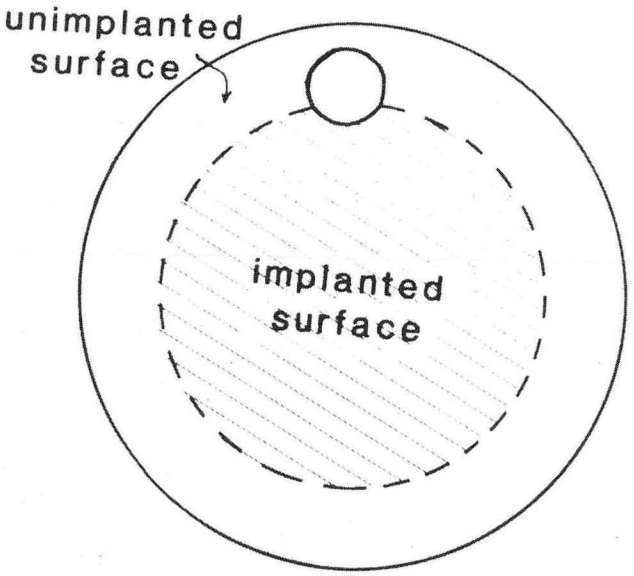

(a)

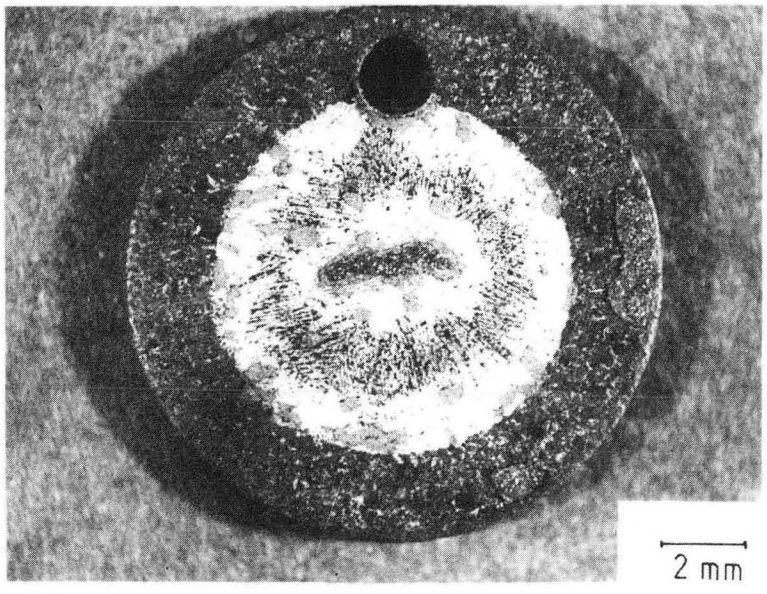

(b)

Figure 20

XBB 860-8771

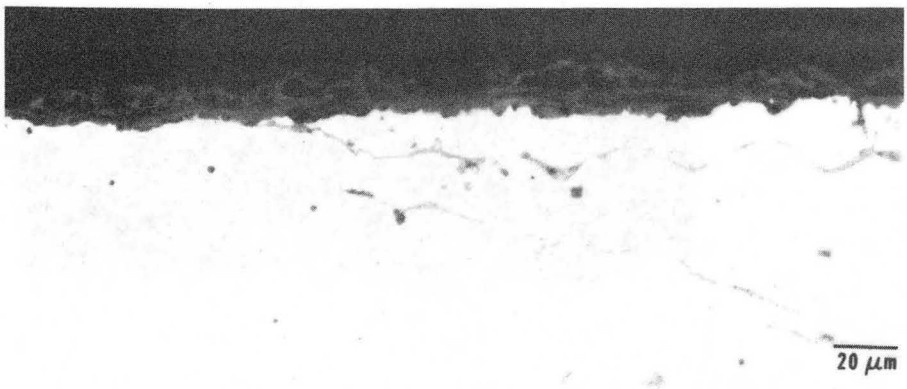

(a)

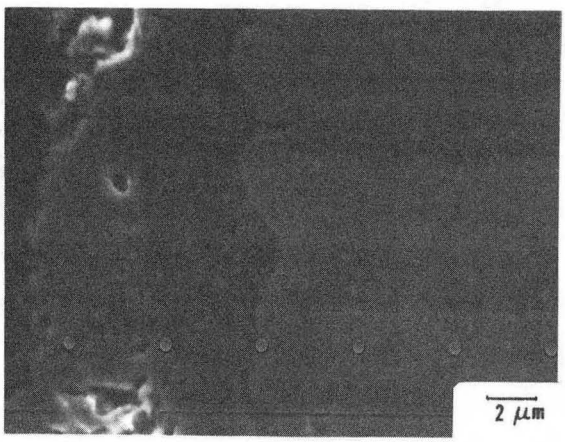

(b)

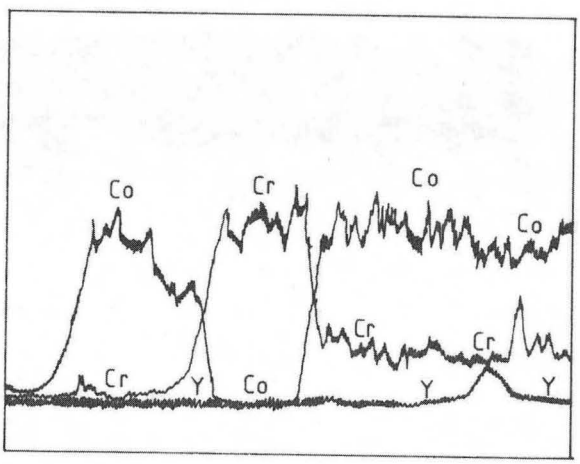

(c)

Figure 21

XBB 860-8781

10 μm

(a)

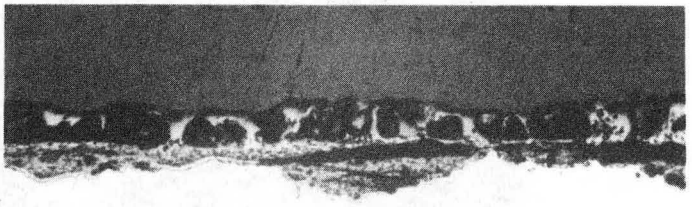

50 μm

(b)

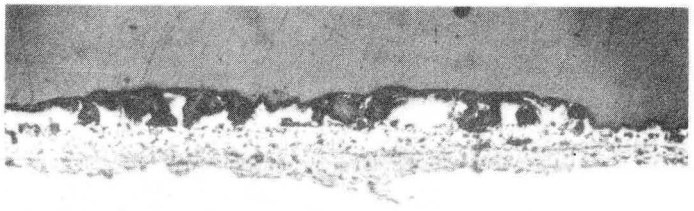

50 μm

Figure 22

XBB 860-8770

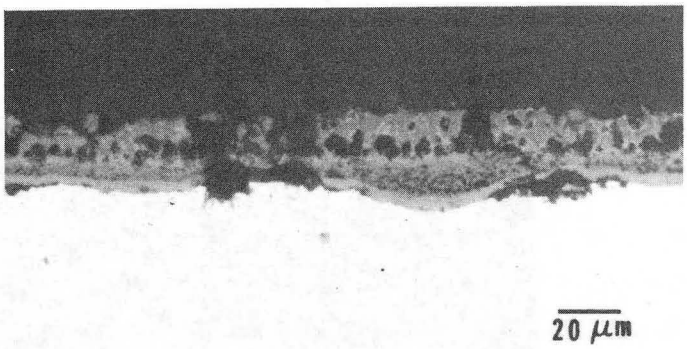

(a)

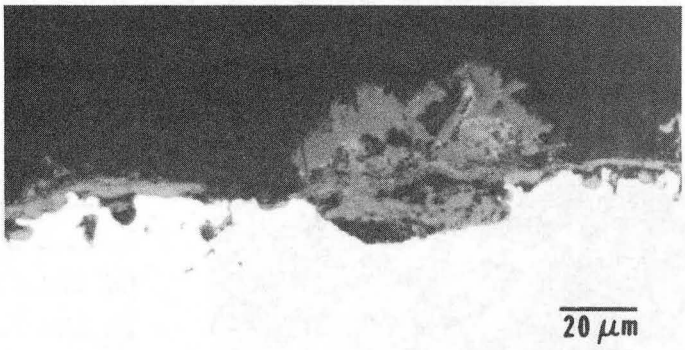

(b)

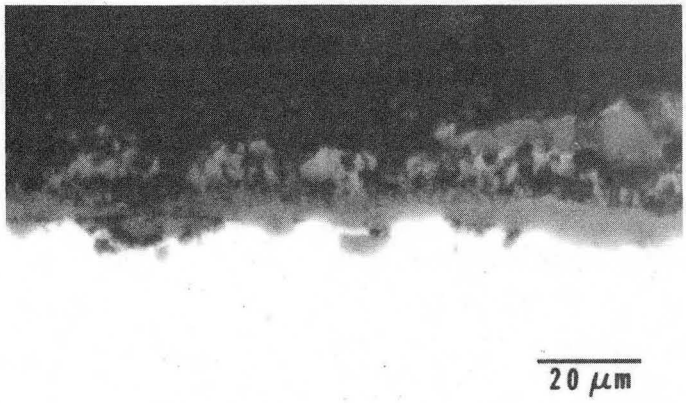

Figure 23

XBB 860-8769

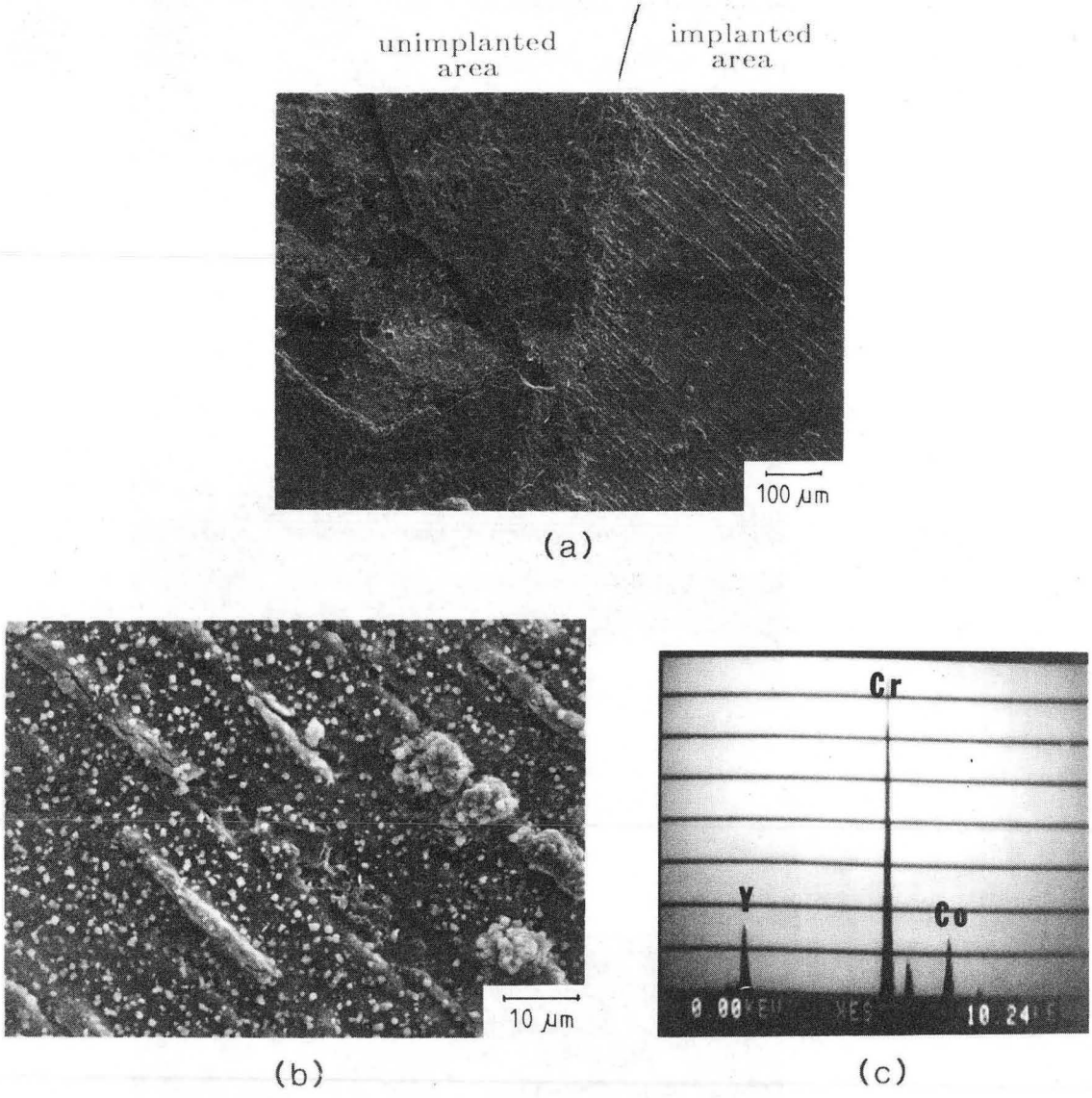

Figure 24

XBB 860-9552

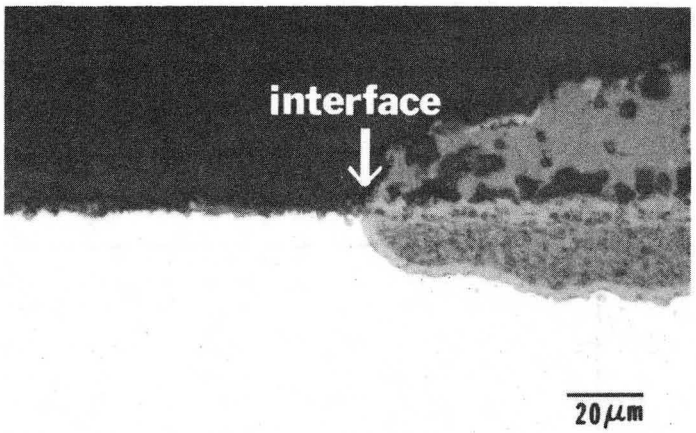

(a)

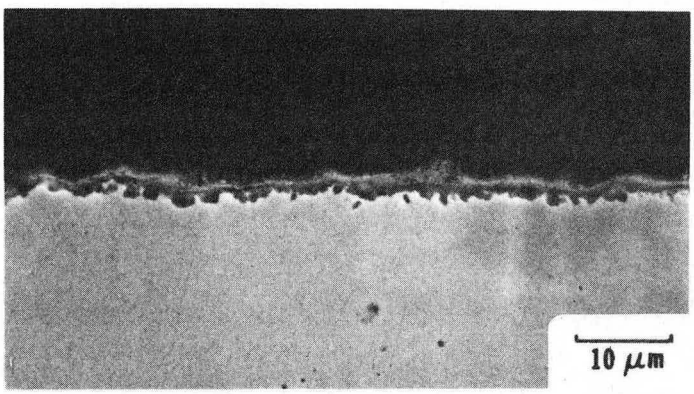

(b)

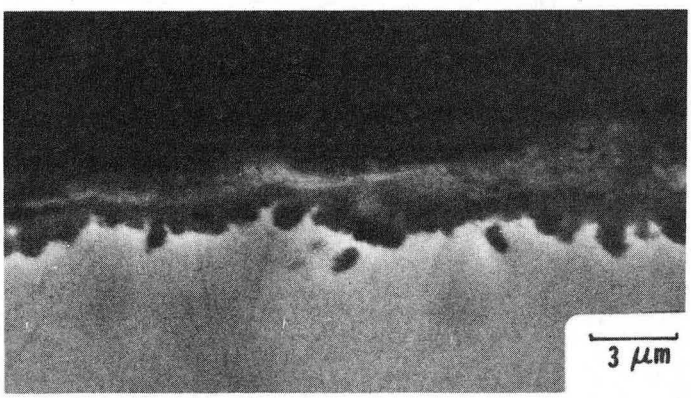

Figure 25

XBB 860-8768

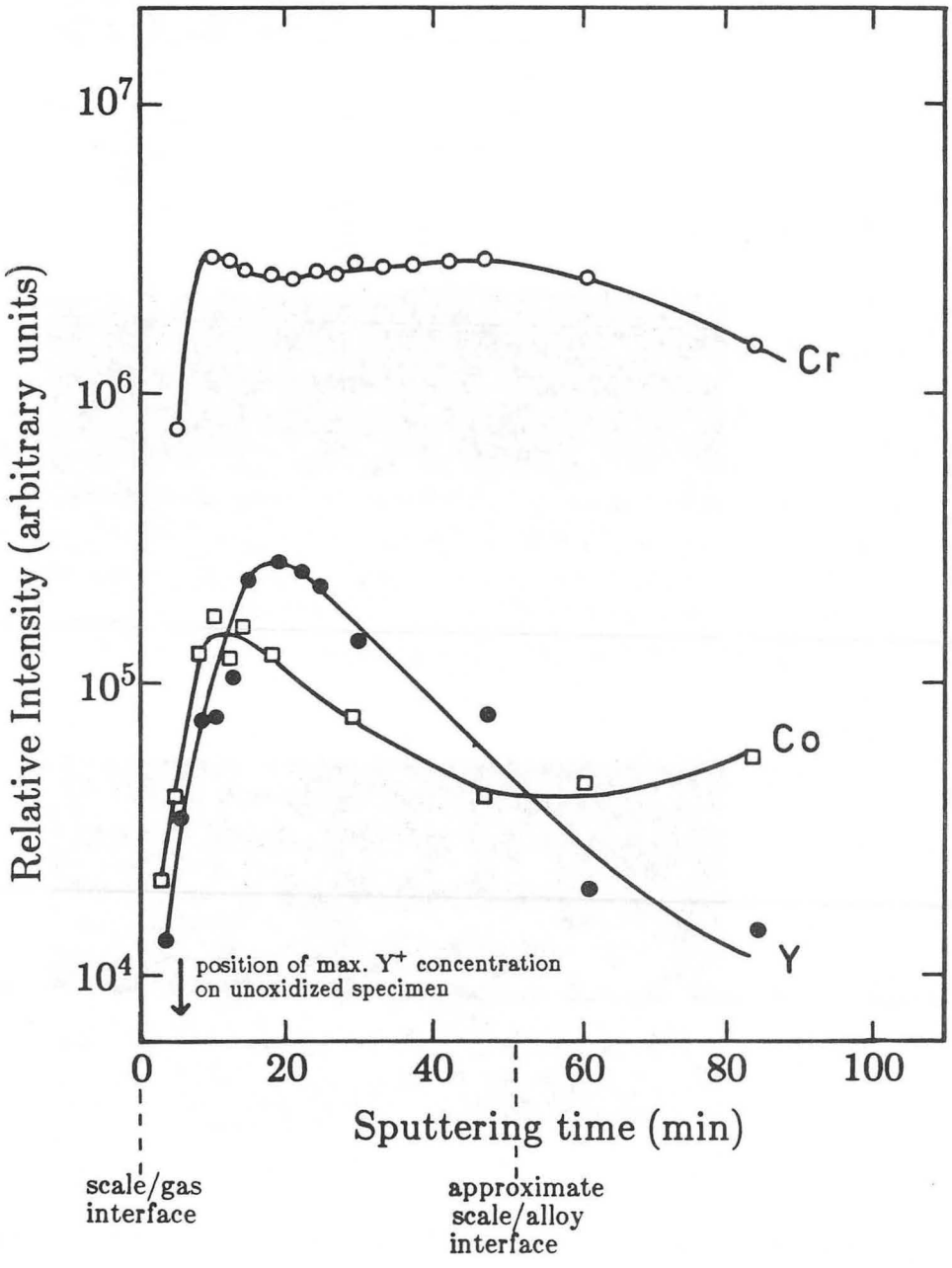

Figure 26

XBL 8612-4801

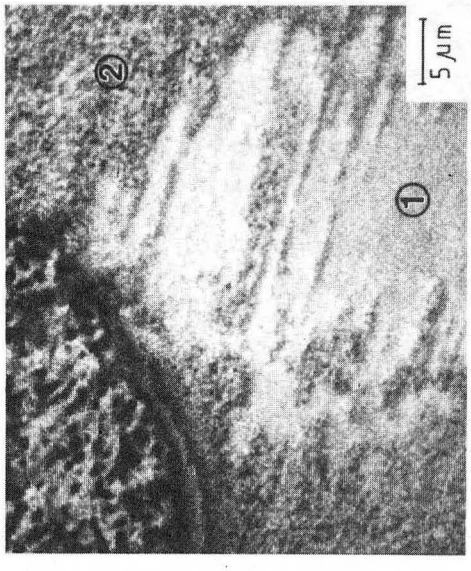

(b)

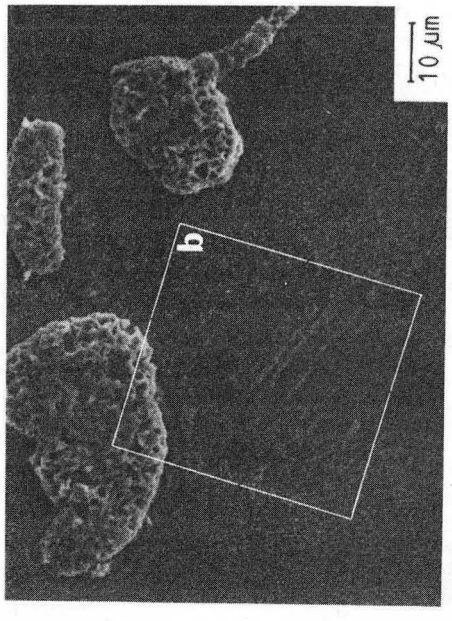

(a)

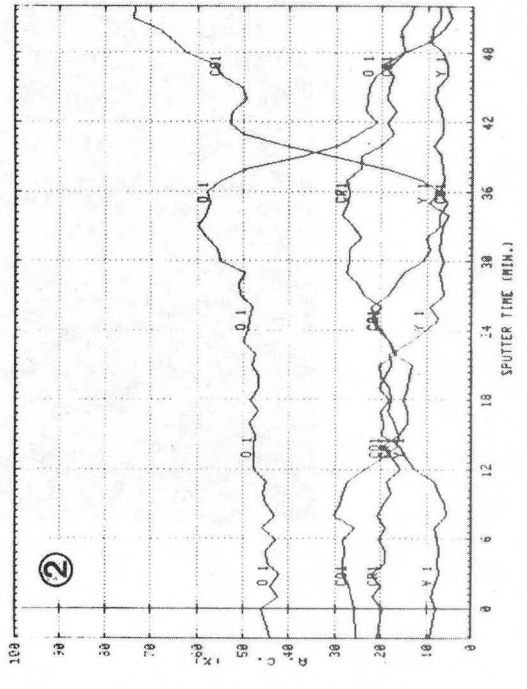

(d)

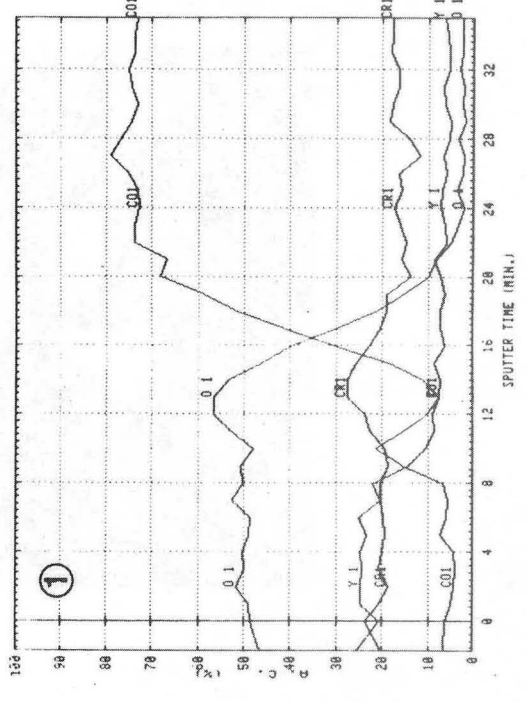

(c)

Figure 27

XBB 860-8777

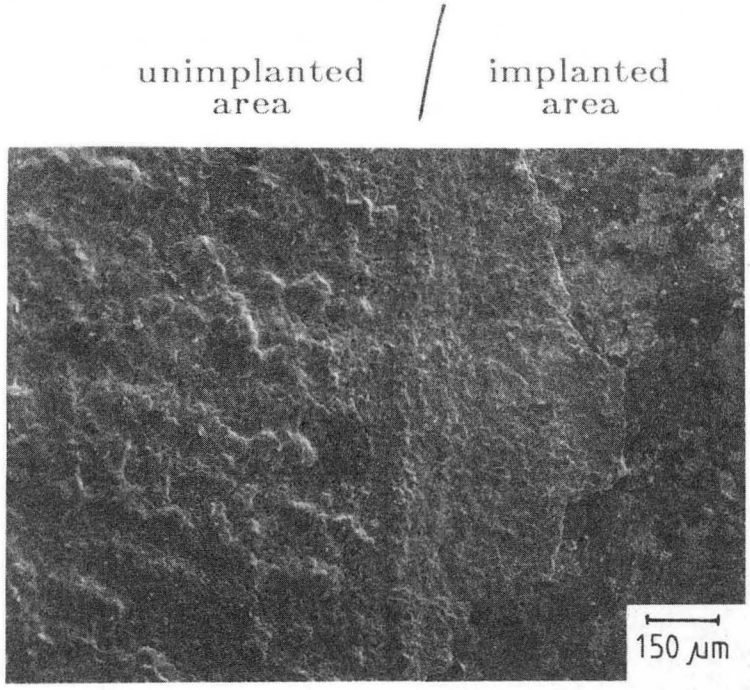

(a)

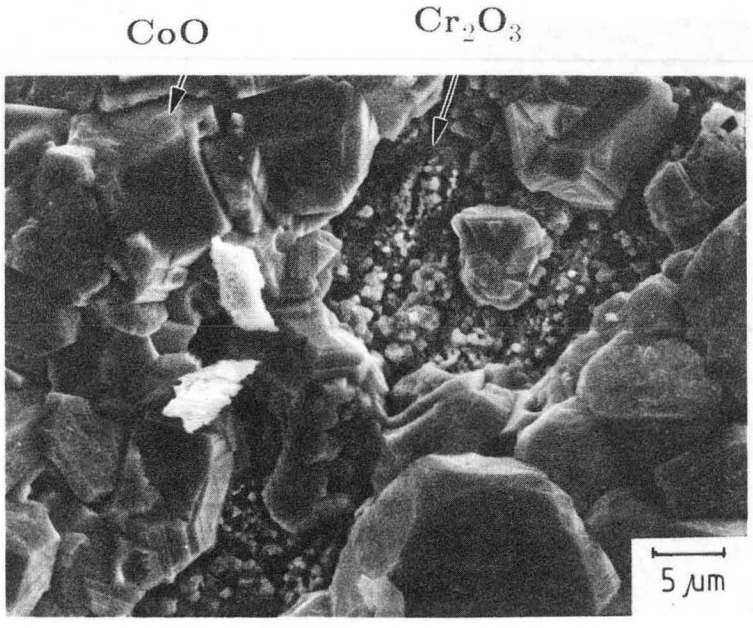

(b)

Figure 28

XBB 860-9555

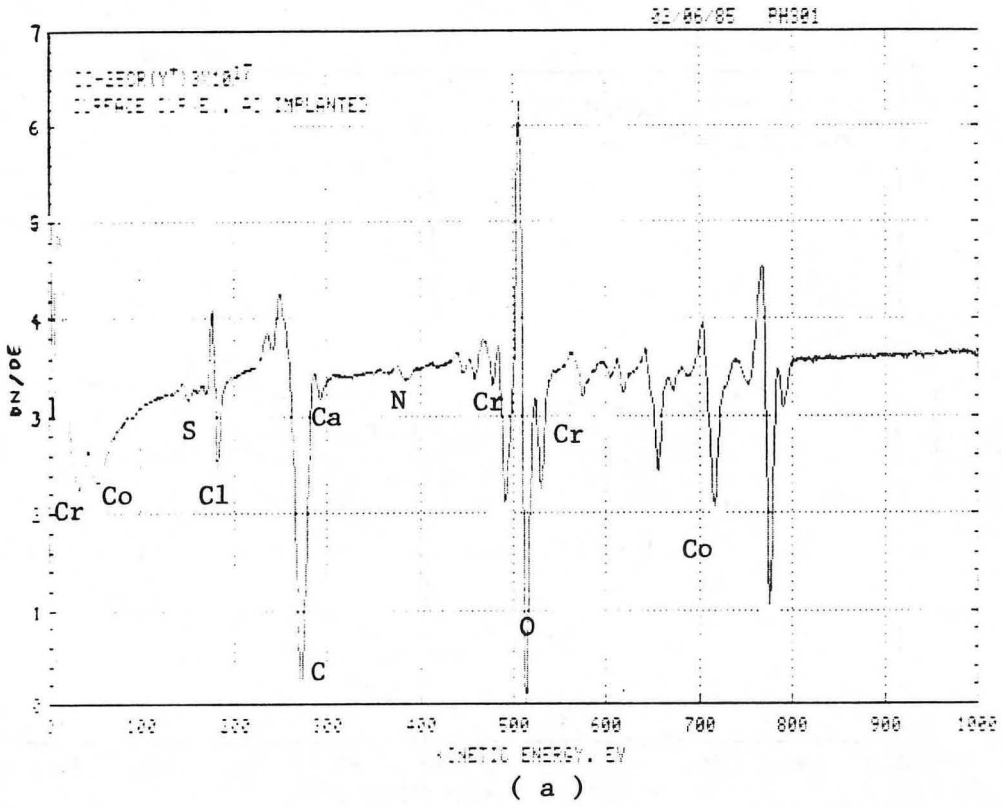
Cr
Co
S
Cl
Ca
C
N
Cr
O
Cr
Co
dN/dE
KINETIC ENERGY, EV

(a)

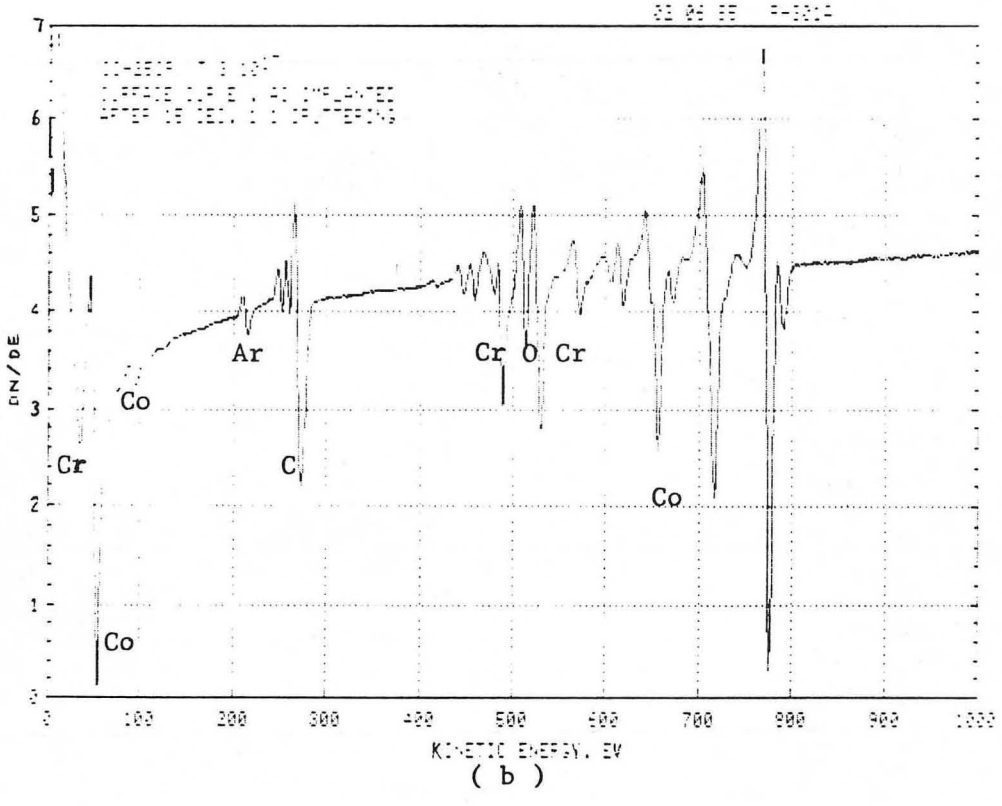
Co
Cr
Co
Ar
C
Cr
O
Cr
Co
dN/dE
KINETIC ENERGY, EV

(b)

Figure 29

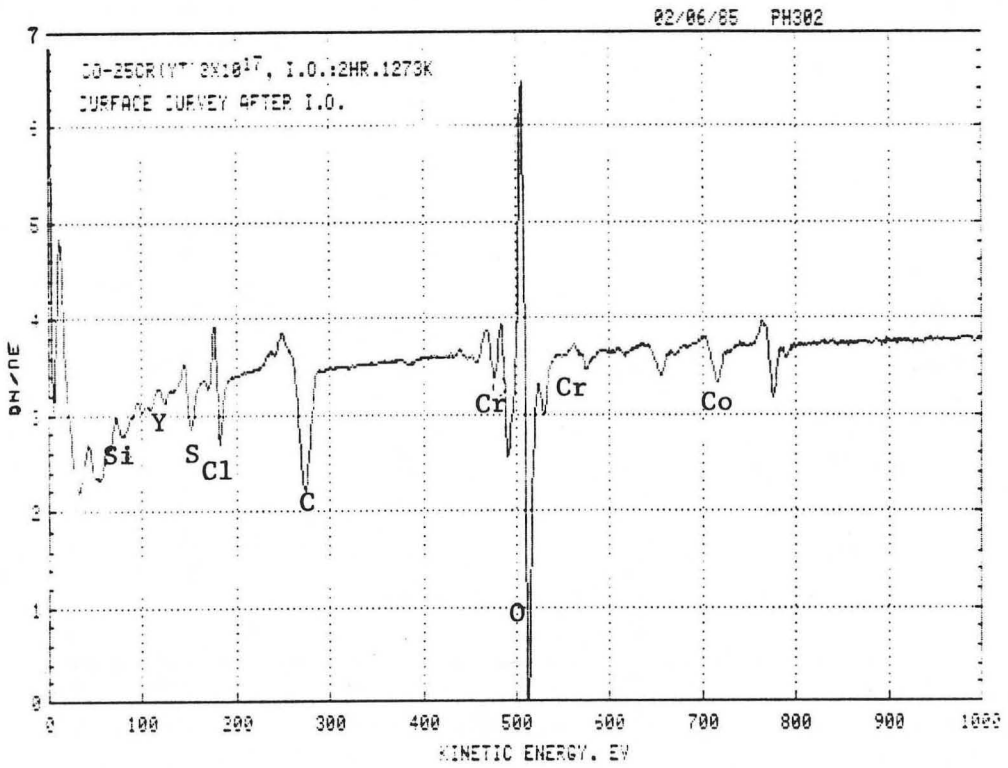
02/06/85 PH302
SURFACE SURVEY AFTER I.O.
Si
Y
S
Cl
C
O
Cr
Cr
Co
KINETIC ENERGY, EV

(a)

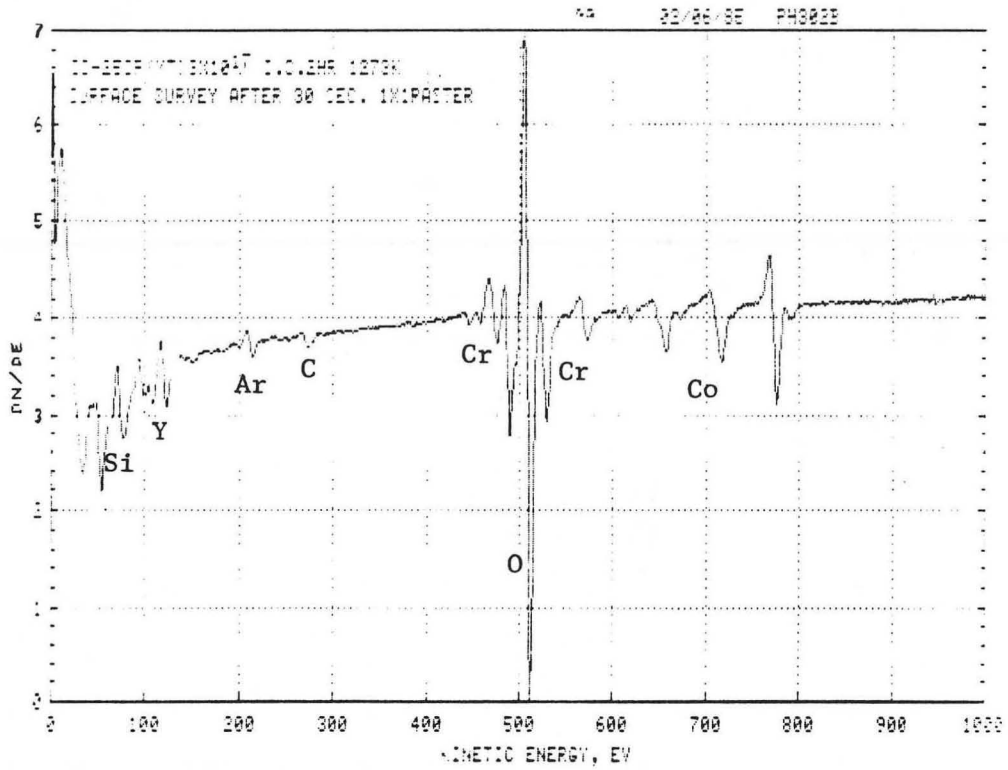
SURFACE SURVEY AFTER 30 SEC. 1X1RASTER
Si
Y
Ar
C
O
Cr
Cr
Co
KINETIC ENERGY, EV

(b)

Figure 30

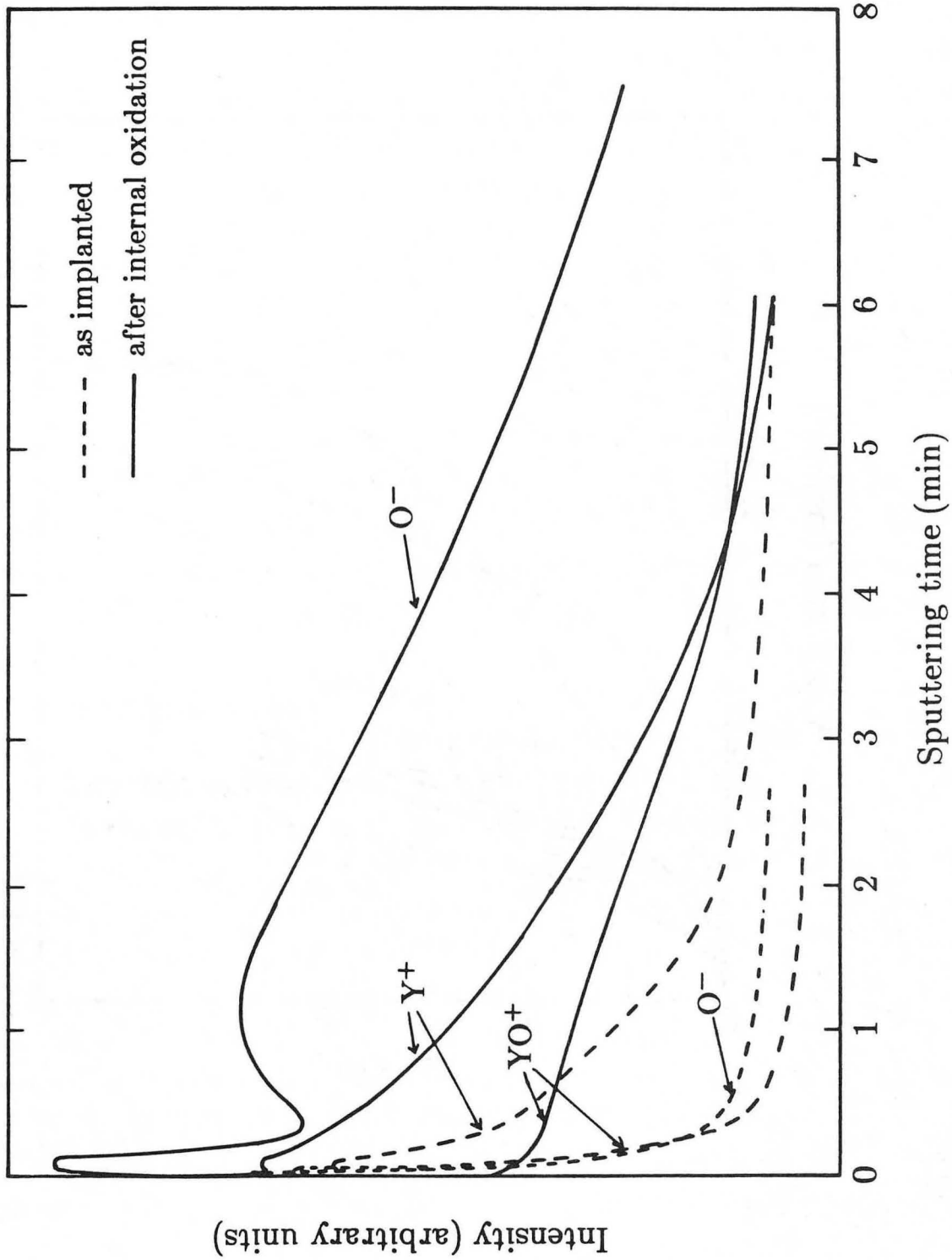

Figure 31

XBL8612-4802

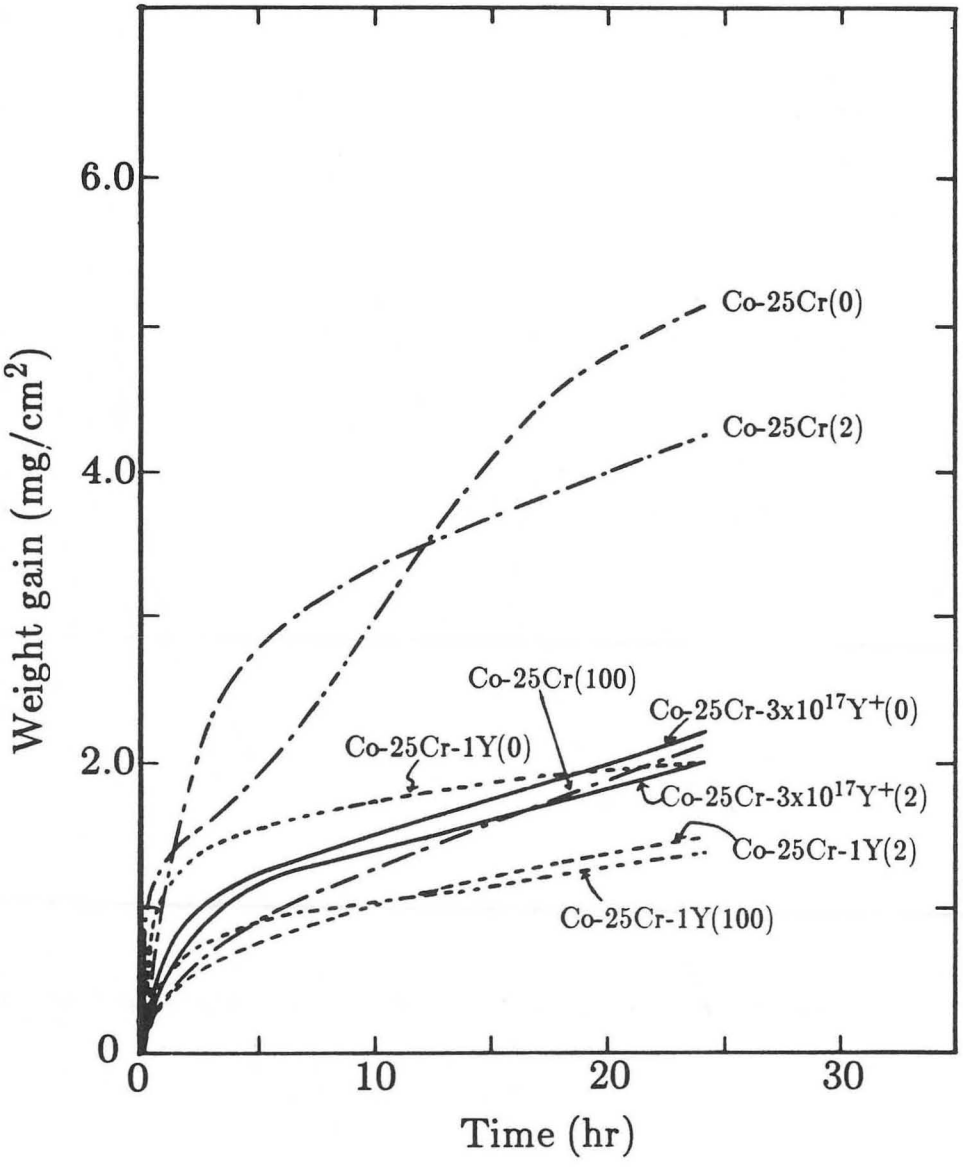

Figure 32

XBL 8612-4803

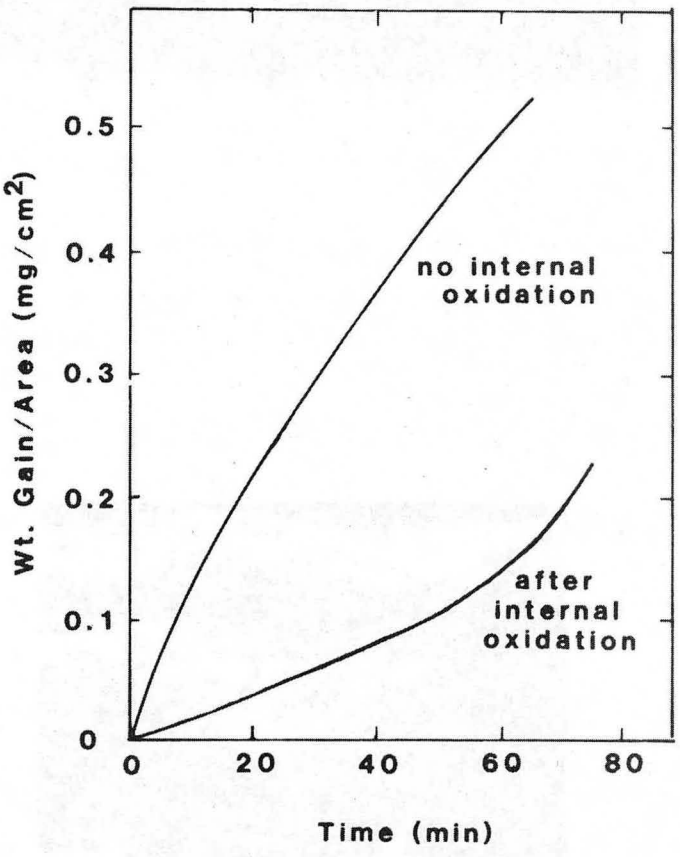

(a)

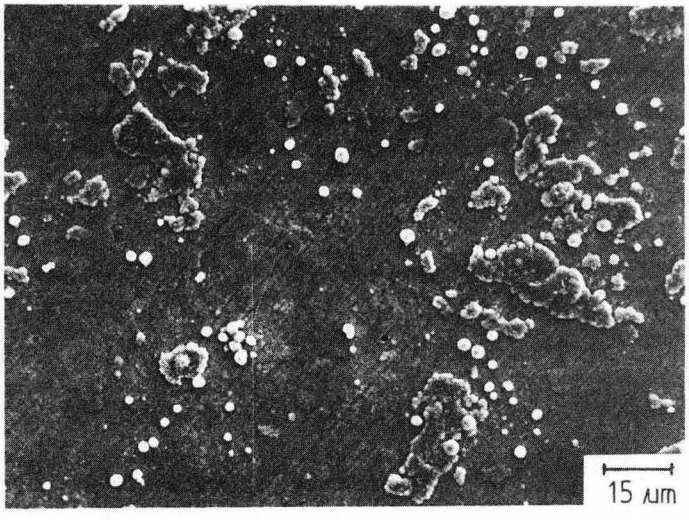

(b)

Figure 33

XBB 860-9549

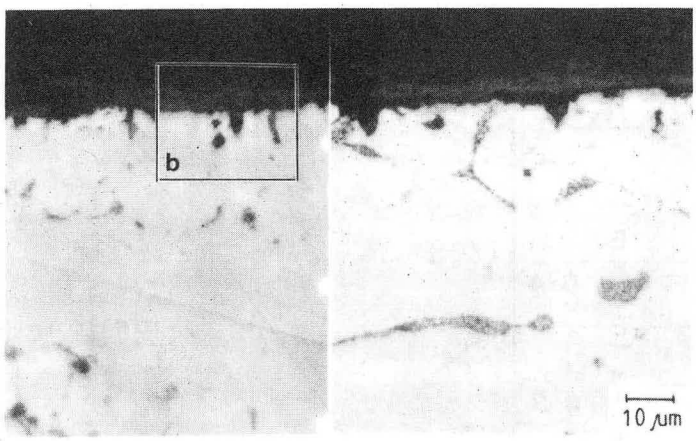

(a)

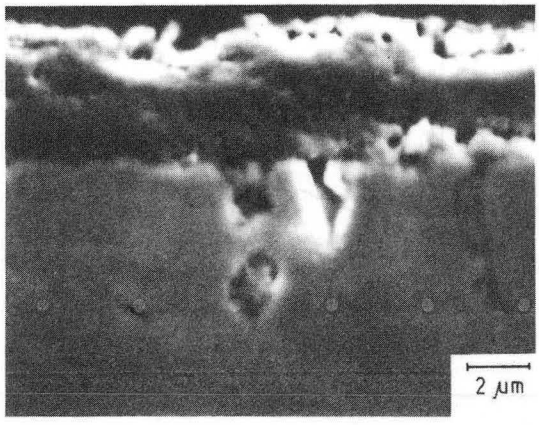

(b)

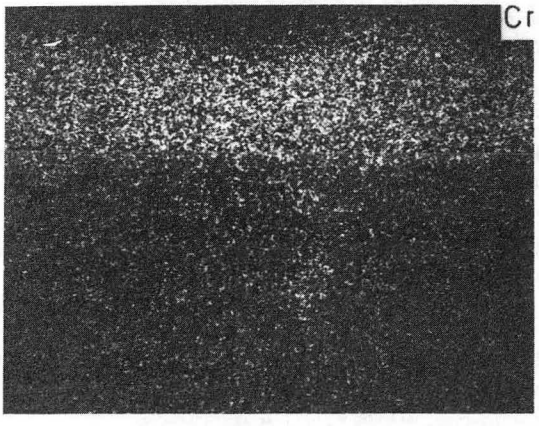

(c)

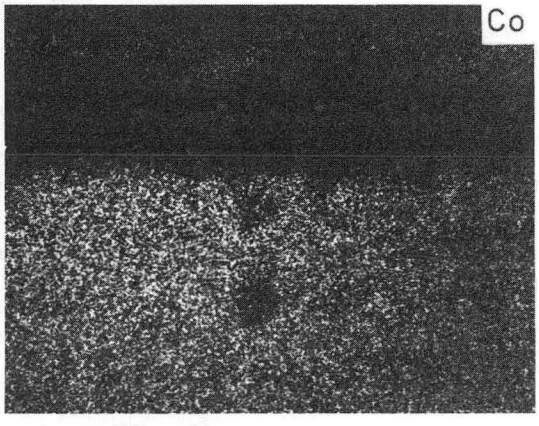

(d)

Figure 34

XBB 860-8779

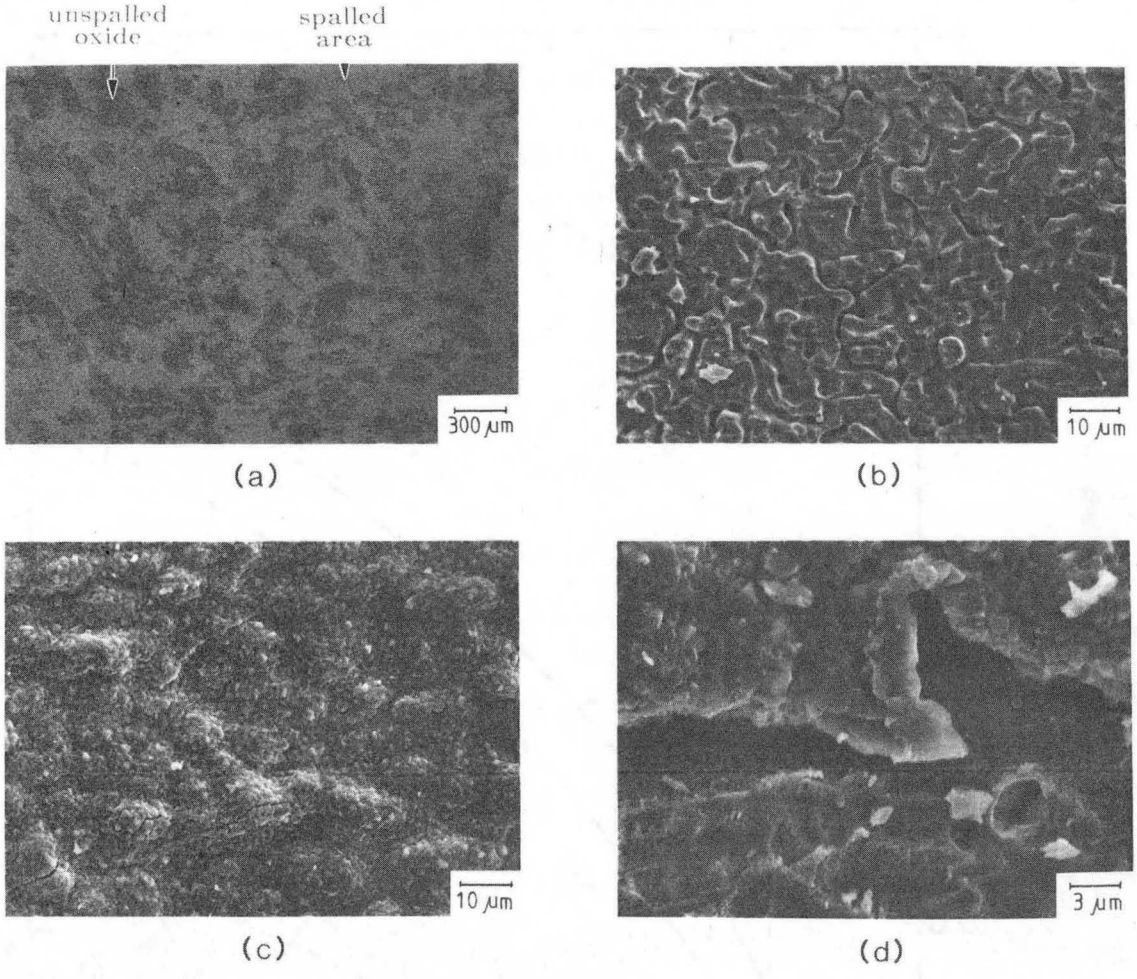

Figure 35

XBB 860-9554

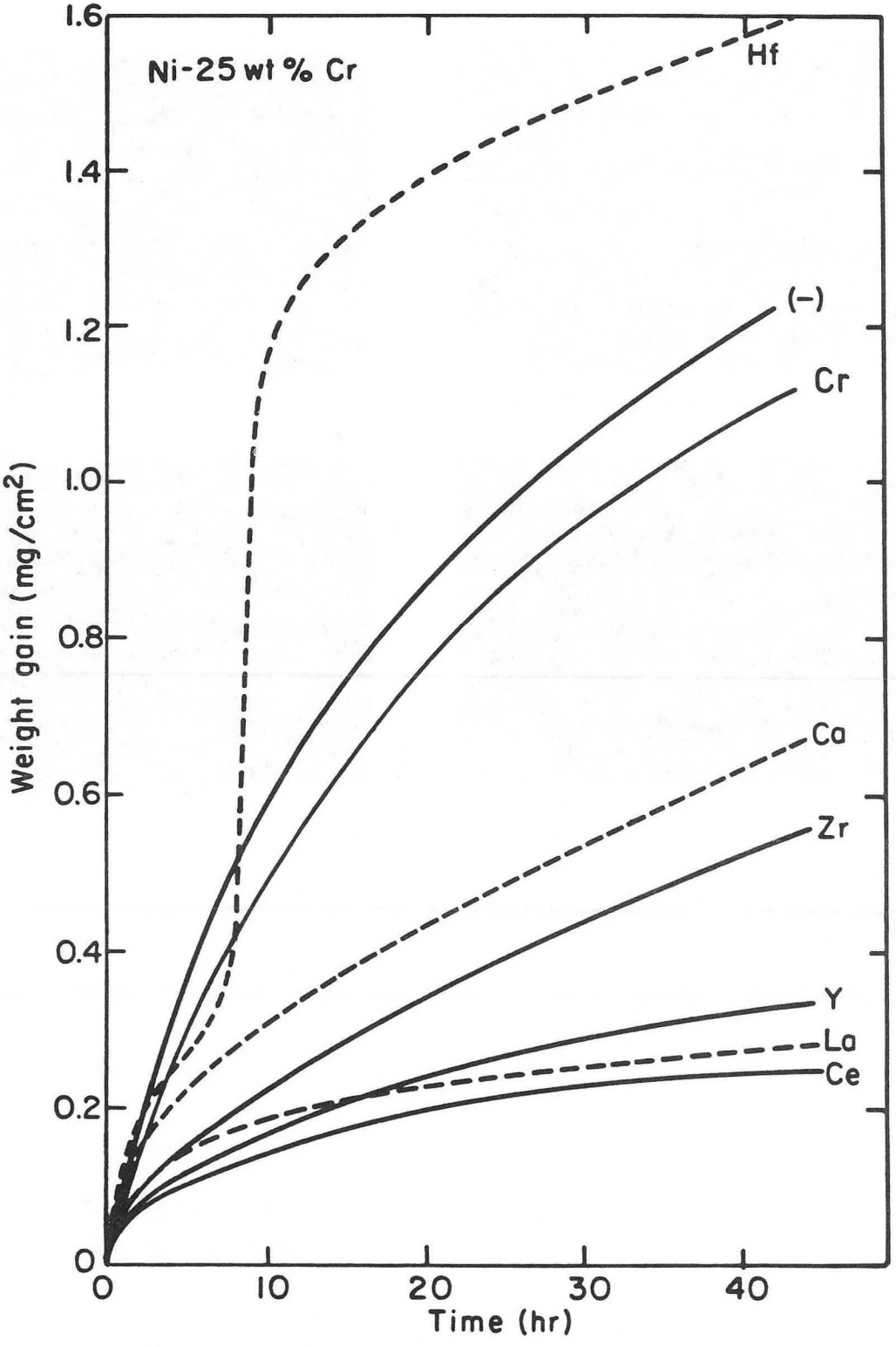

Figure 36

XBL 854-6038A

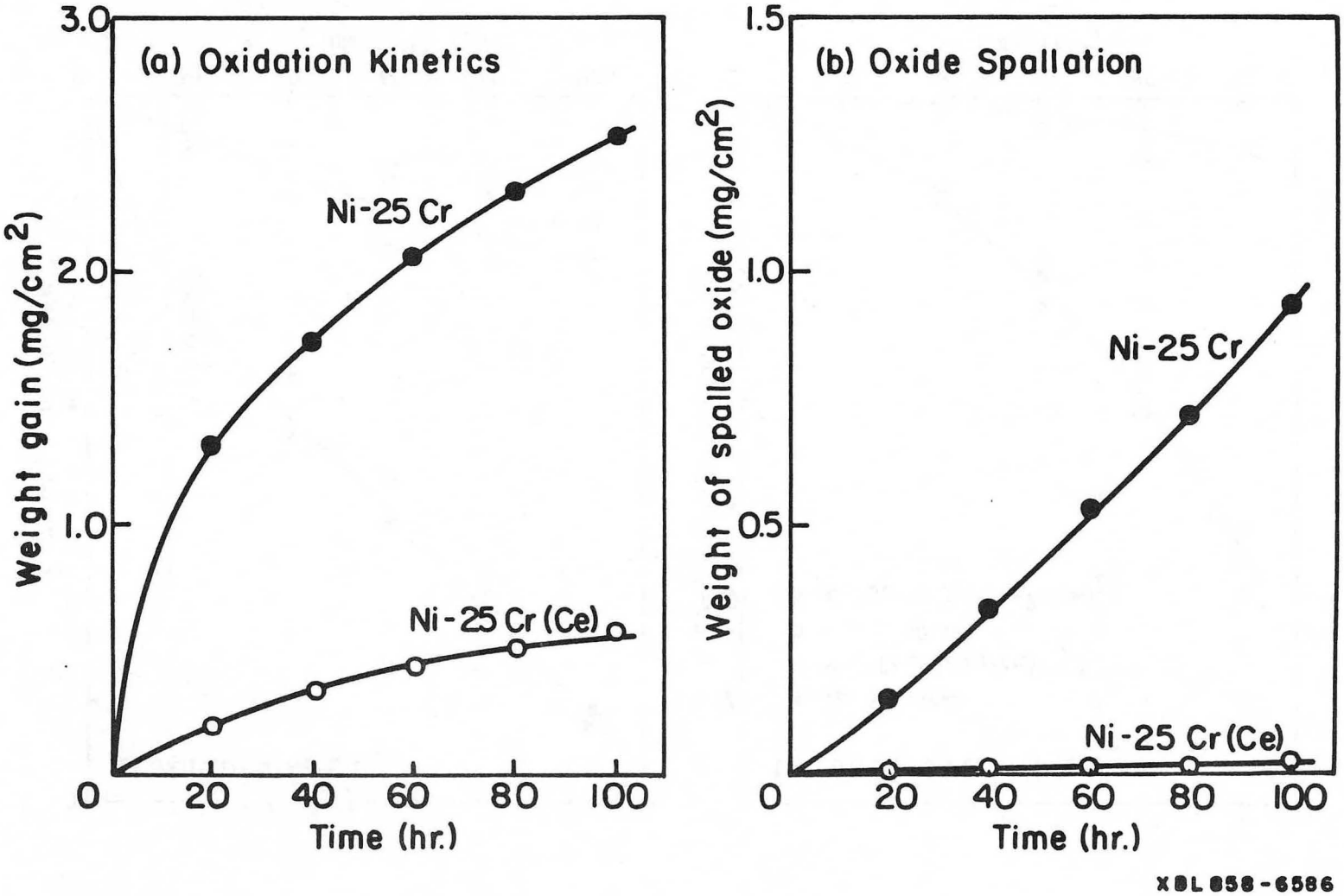
(a) Oxidation Kinetics
Weight gain (mg/cm²)
3.0
2.0
1.0
0
Ni-25 Cr
Ni-25 Cr (Ce)
20
40
60
80
100
Time (hr.)
(b) Oxide Spallation
Weight of spalled oxide (mg/cm²)
1.5
1.0
0.5
0
Ni-25 Cr
Ni-25 Cr (Ce)
20
40
60
80
100
Time (hr.)
XBL 858-6586

Figure 37

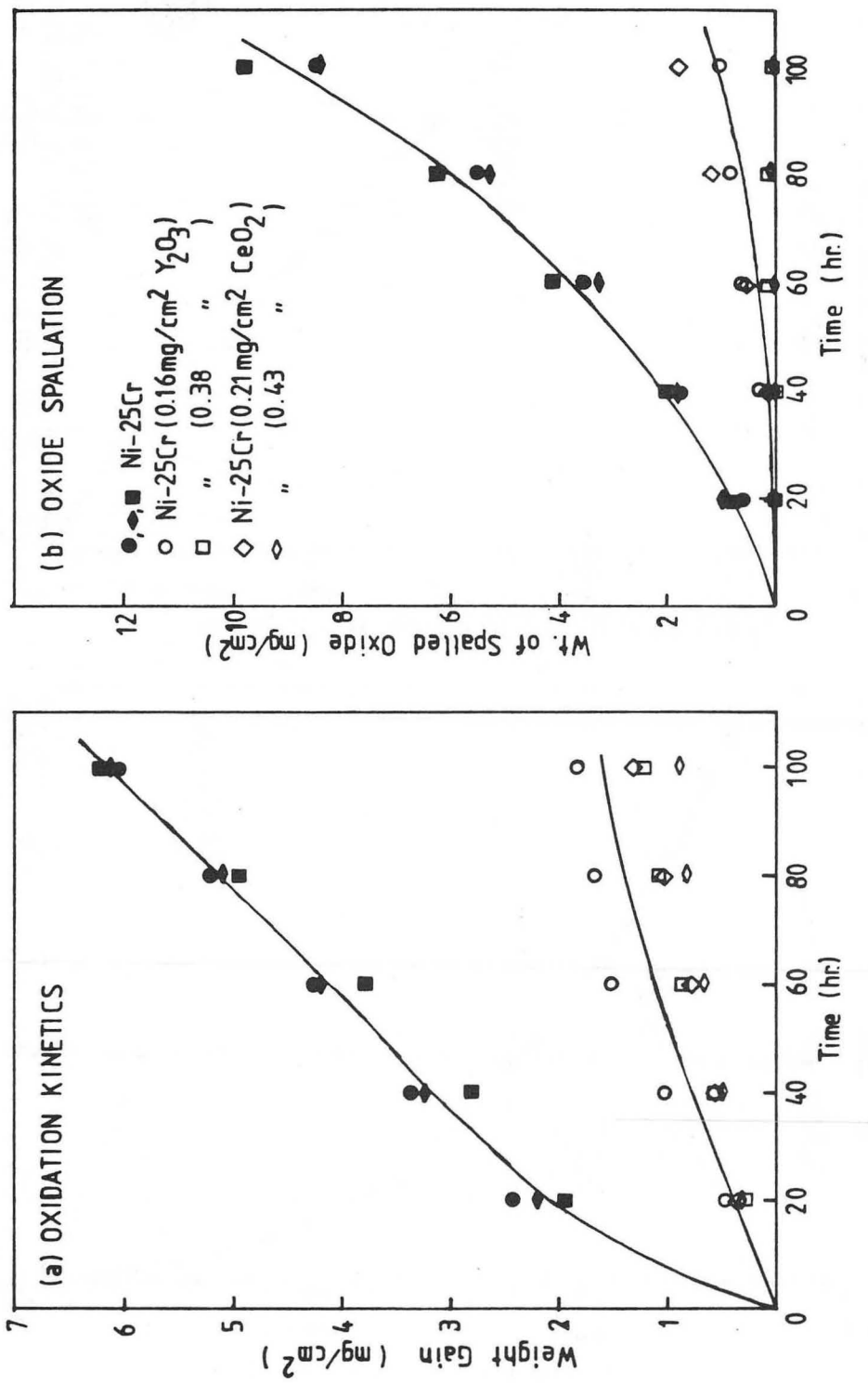
(a) OXIDATION KINETICS
Weight Gain (mg/cm²)
Time (hr.)
(b) OXIDE SPALLATION
●,◆,■ Ni-25Cr
○ Ni-25Cr (0.16mg/cm² Y₂O₃)
□ " (0.38 ")
◇ Ni-25Cr (0.21mg/cm² CeO₂)
◊ " (0.43 ")
Wt. of Spalled Oxide (mg/cm²)
Time (hr.)

Figure 38

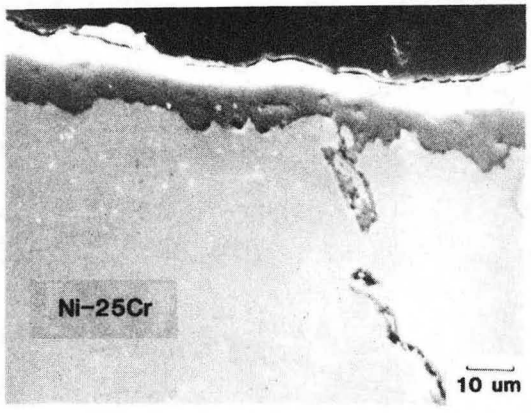

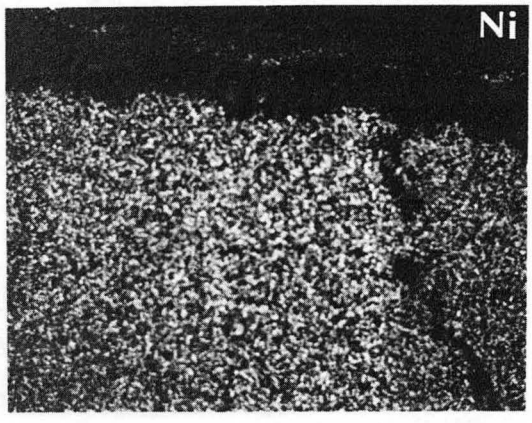

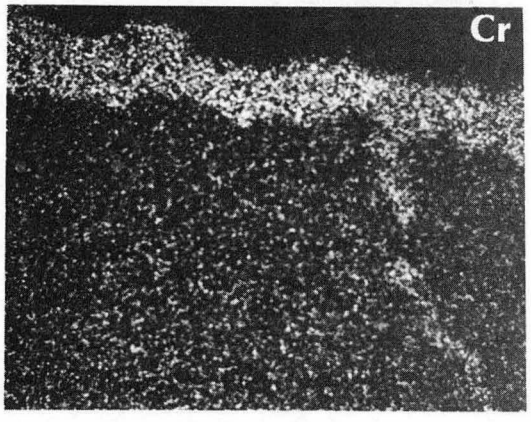

Figure 39

XBB 854-2642

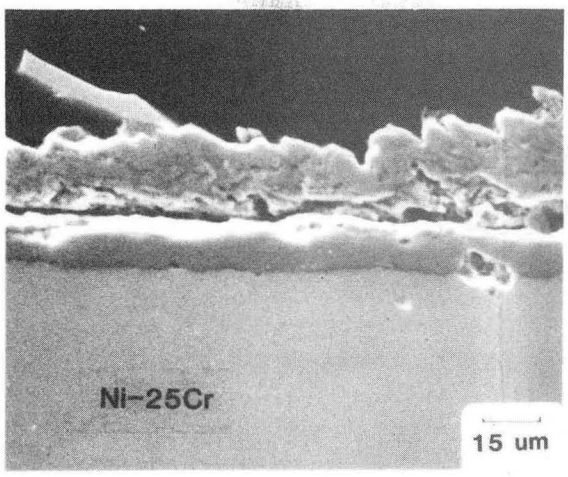

(a)

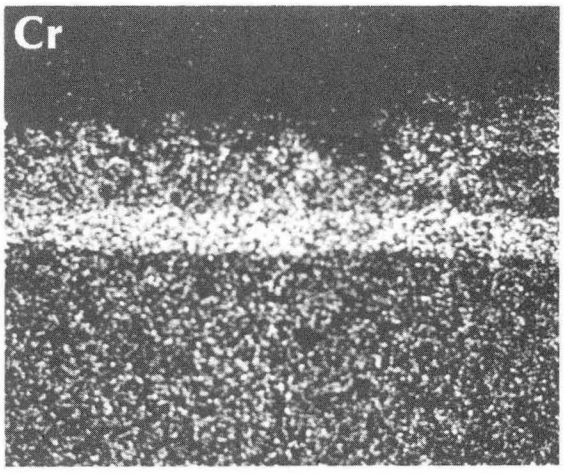

(b)

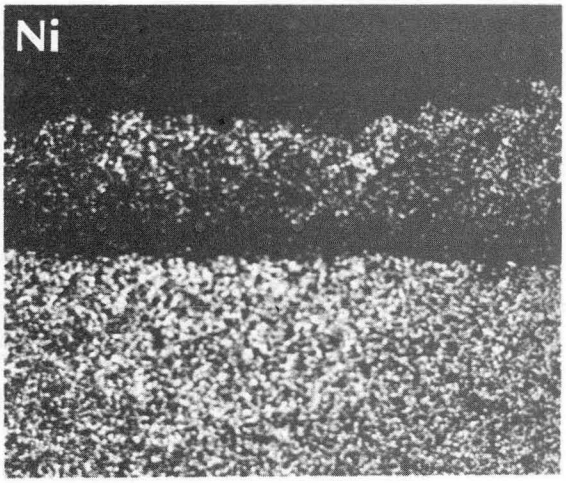

(c)

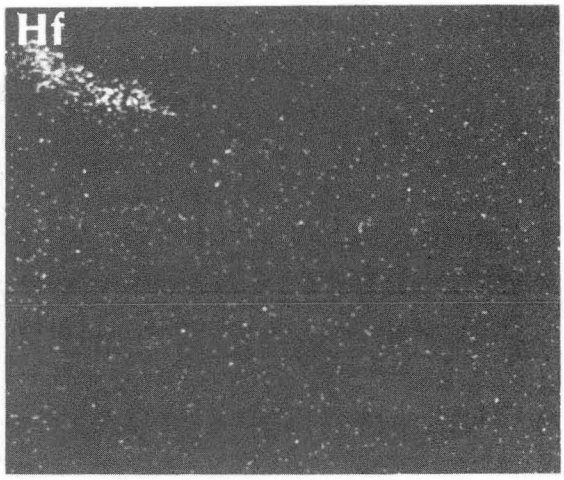

(d)

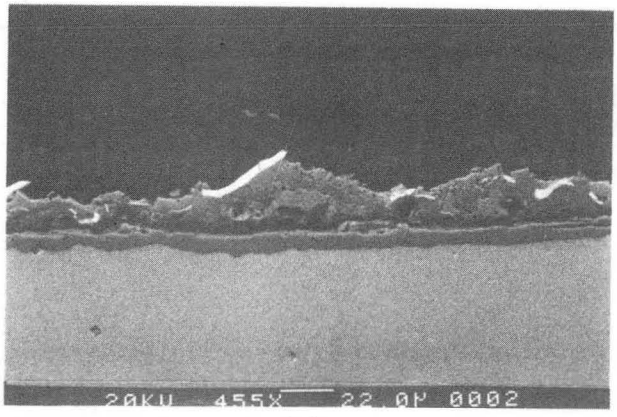

(e)

Figure 40

XBB 858-6445

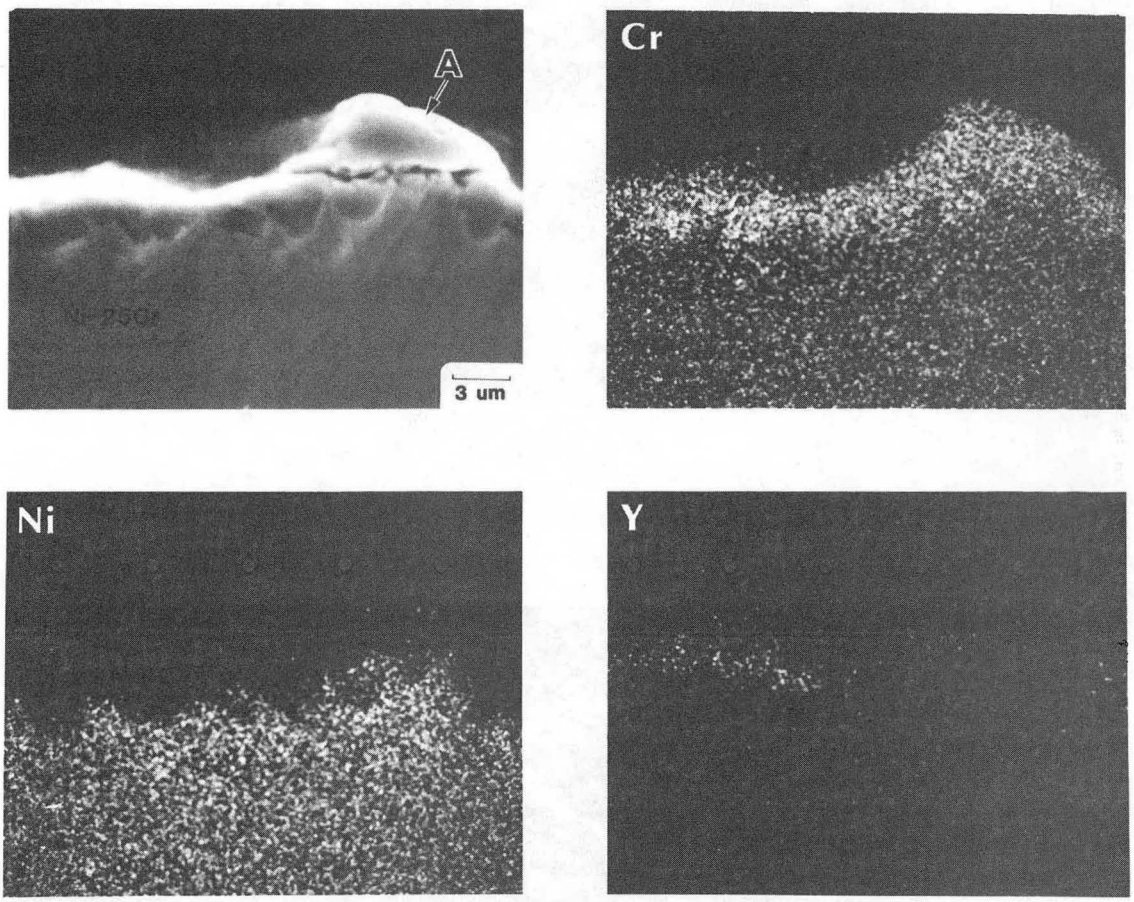

Figure 41

XBB 854-2636A

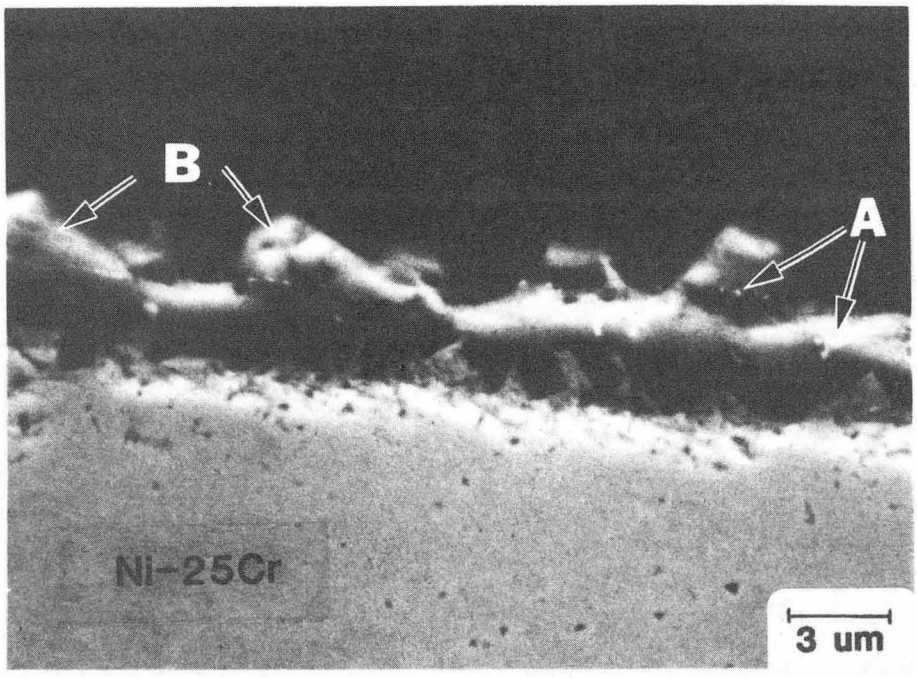

(a)

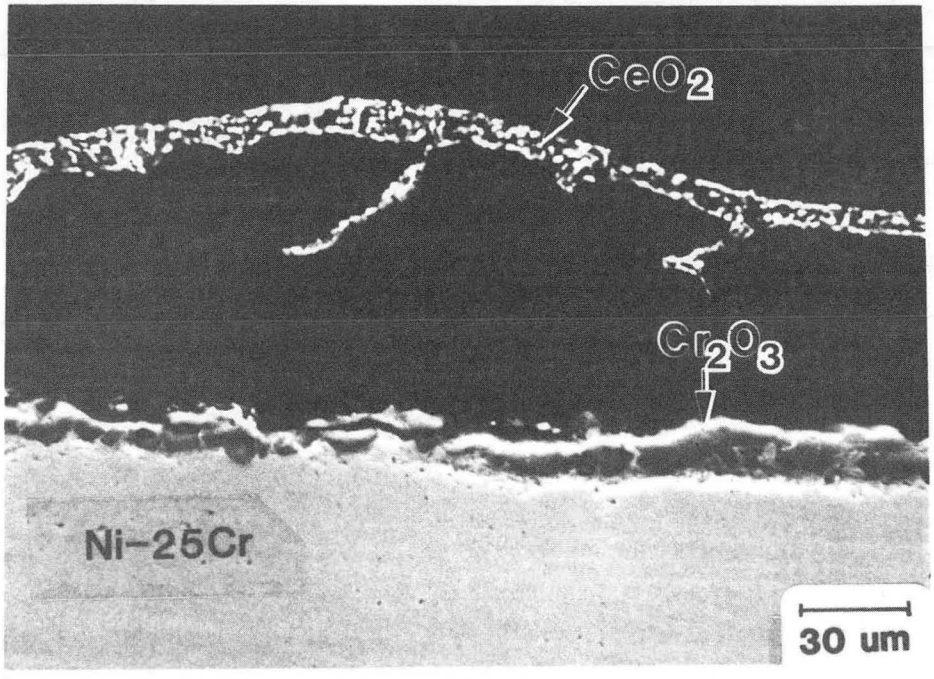

(b)

Figure 42

XBB 858-6443A

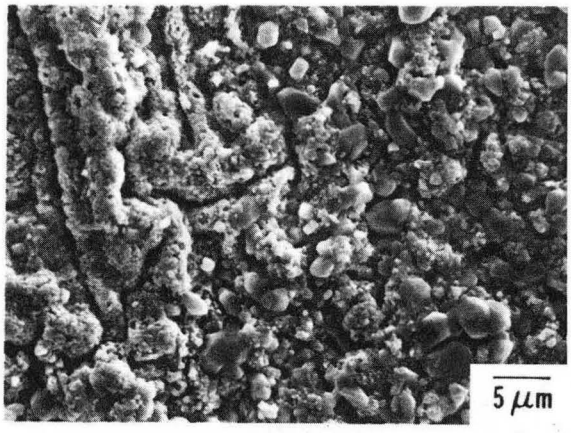

(a)

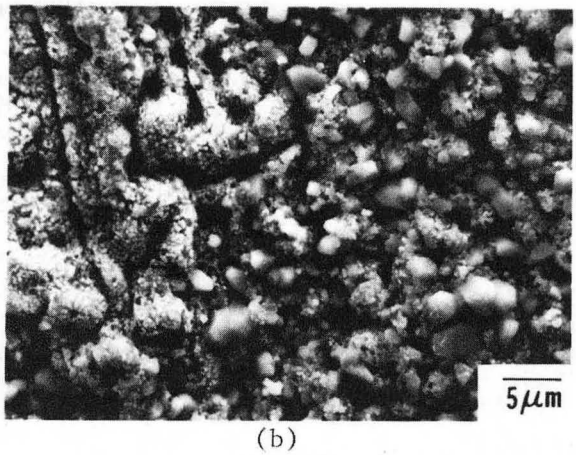

(b)

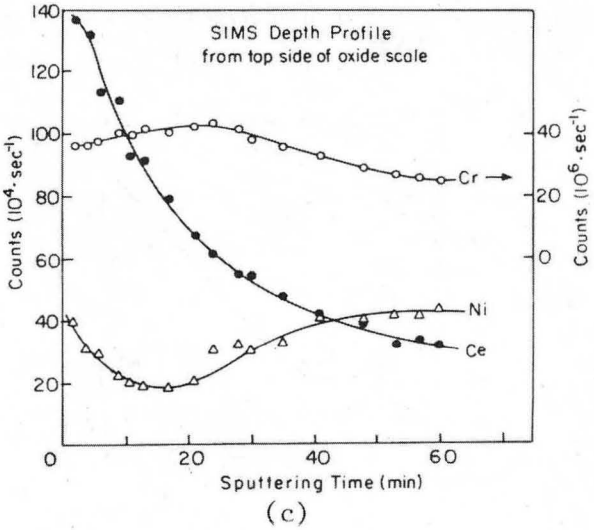

(c)

Figure 43

XBB 866-4919

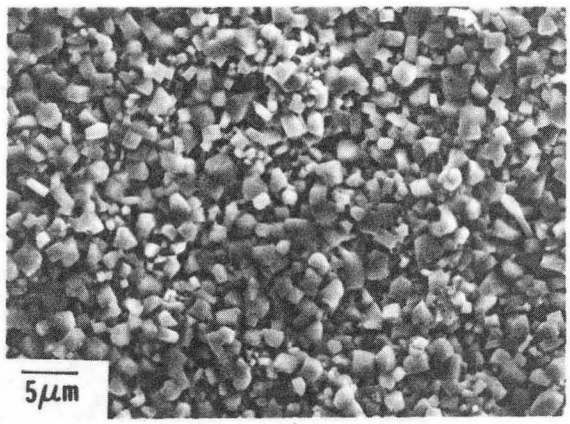

(a)

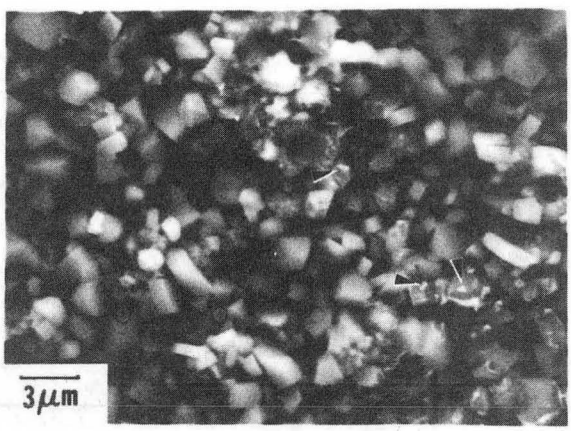

(b)

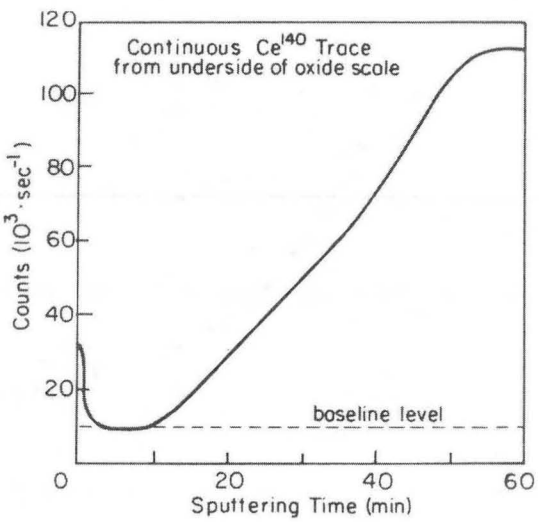

(c)

Figure 44

XBB 866-4920

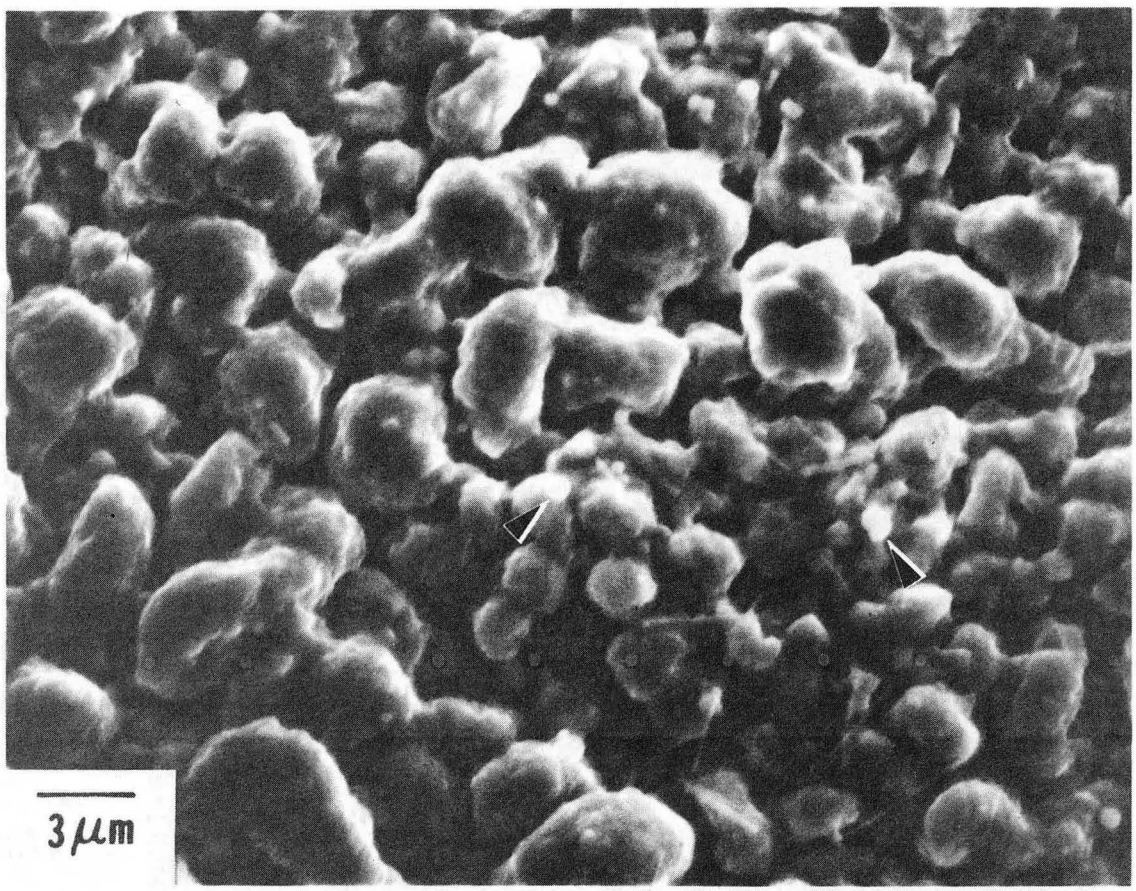

Figure 45

XBB 866-4916

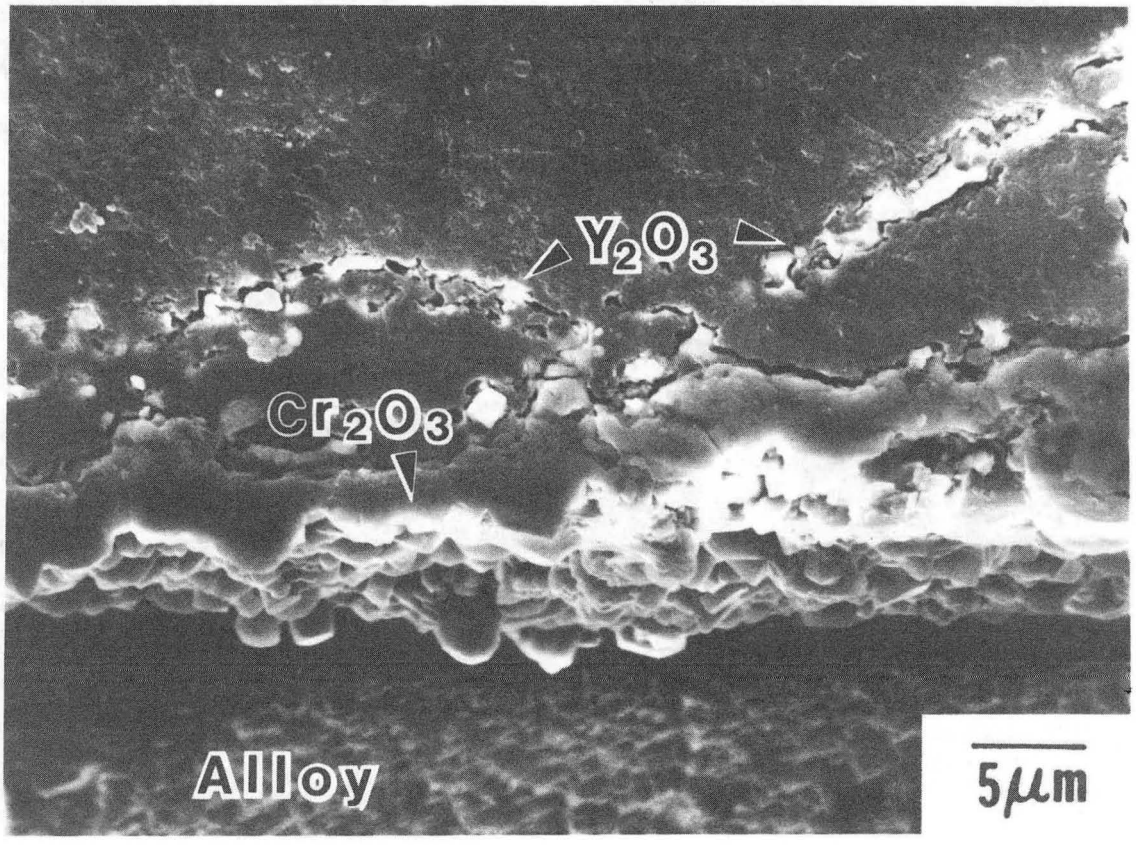

Figure 46

XBB 866-4915

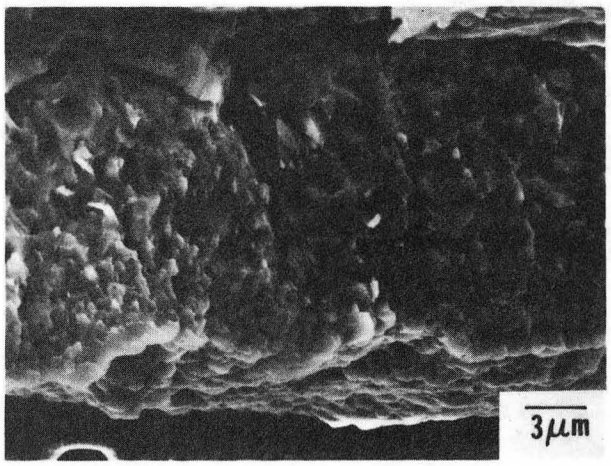

(a)

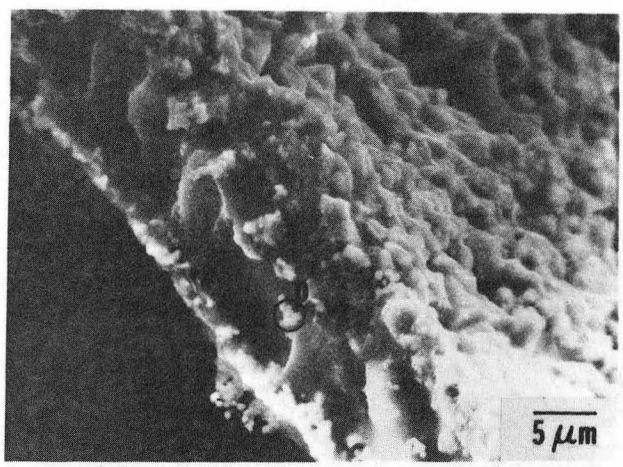

(b)

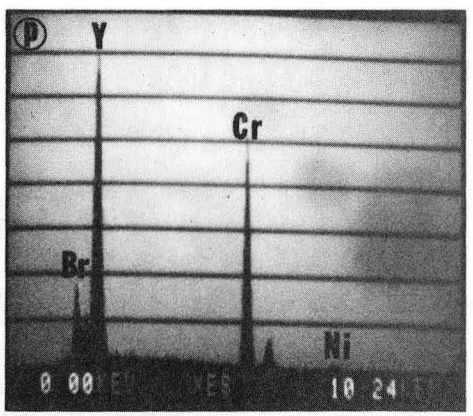

Figure 47

XBB 866-4917

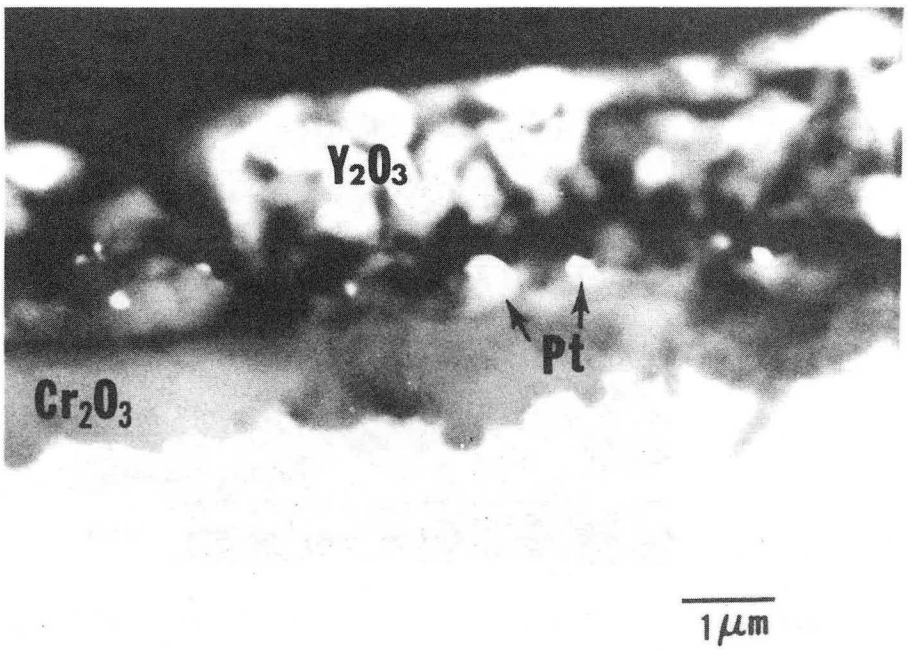

(a)

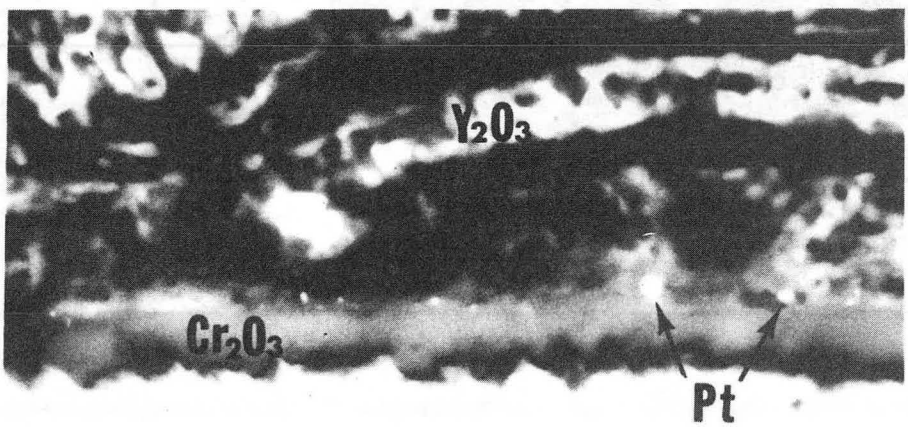

(b)

Figure 48

XBB 866-4509

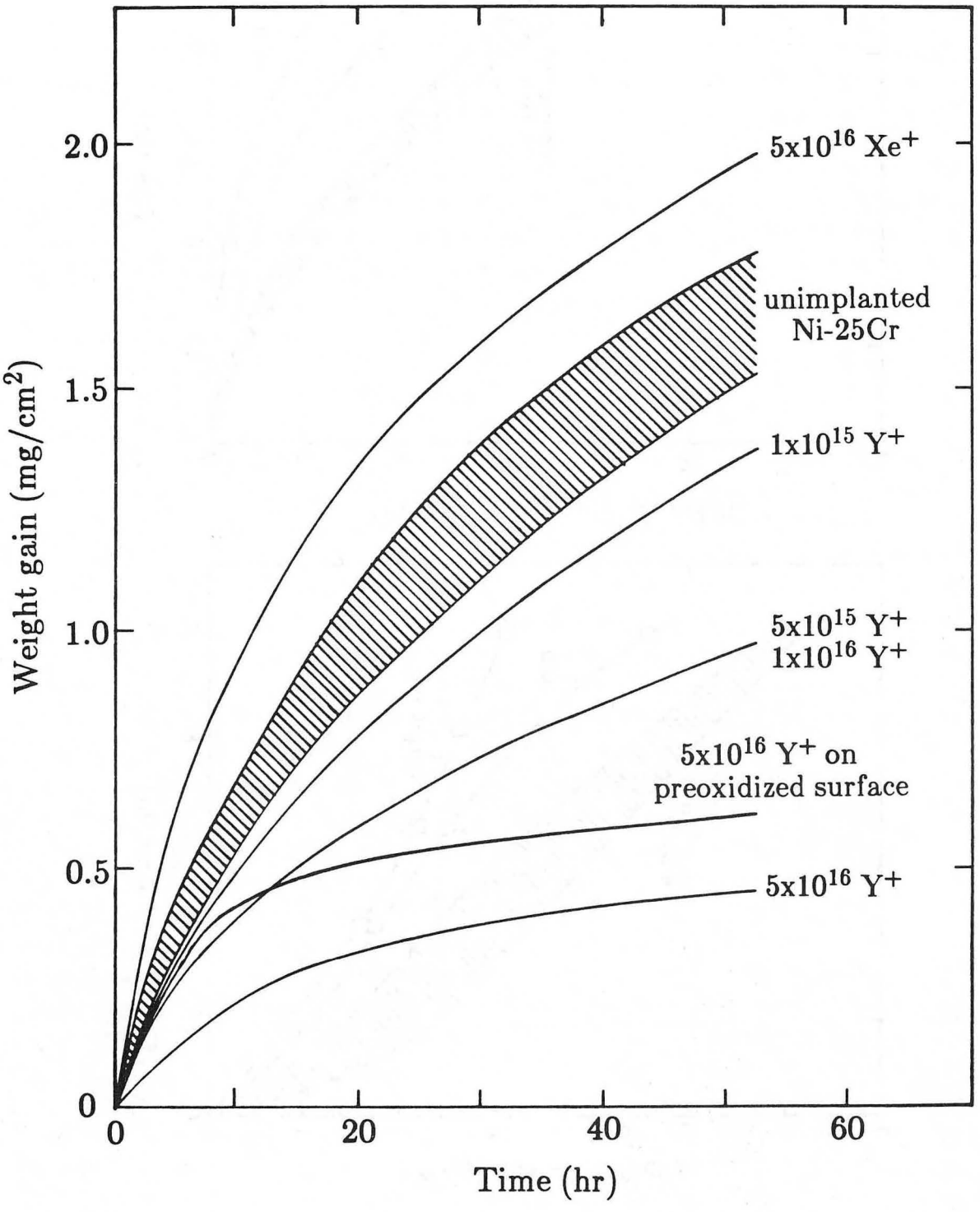

Figure 49

XBL 8612-4792

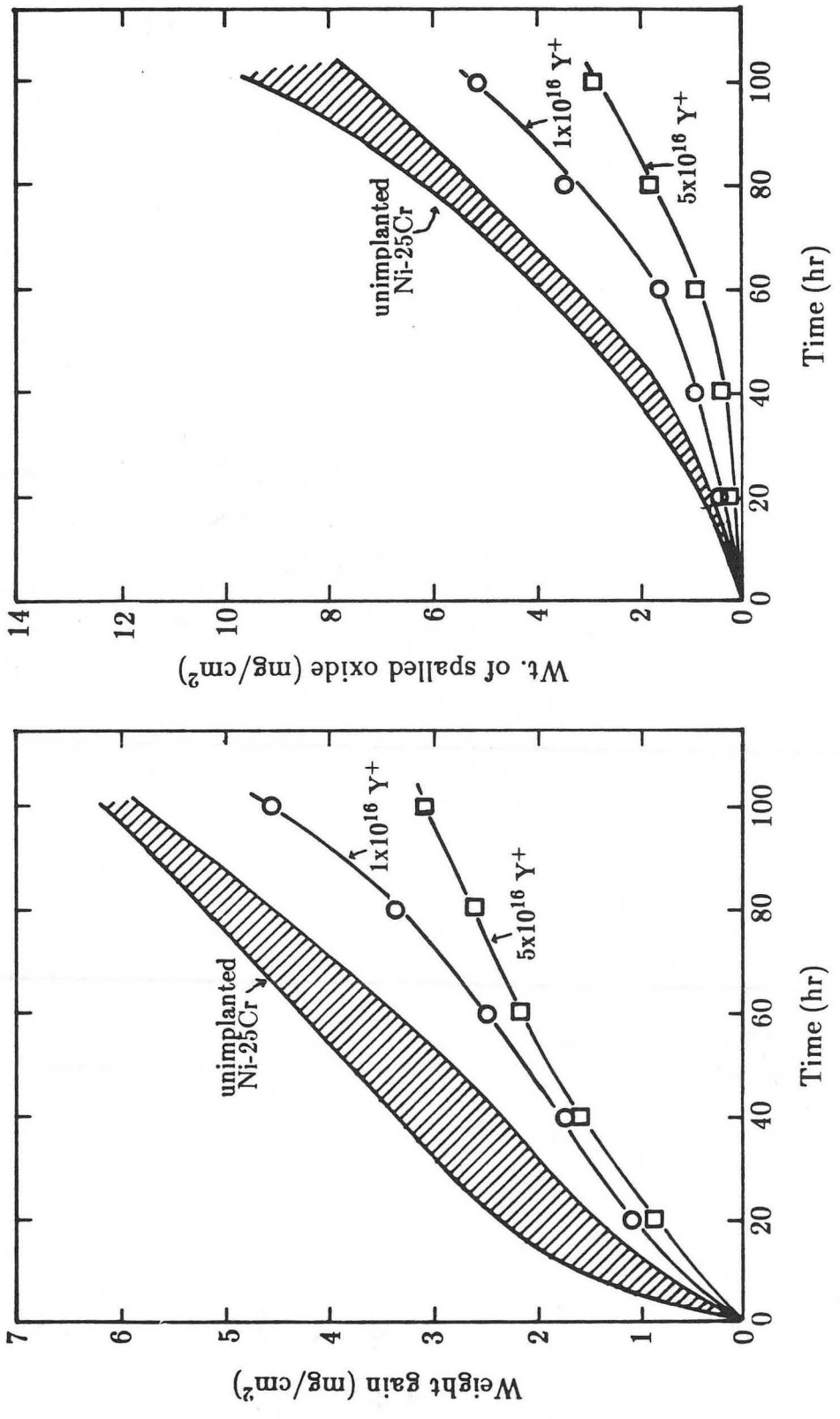

Figure 50

XBL 8612-4793

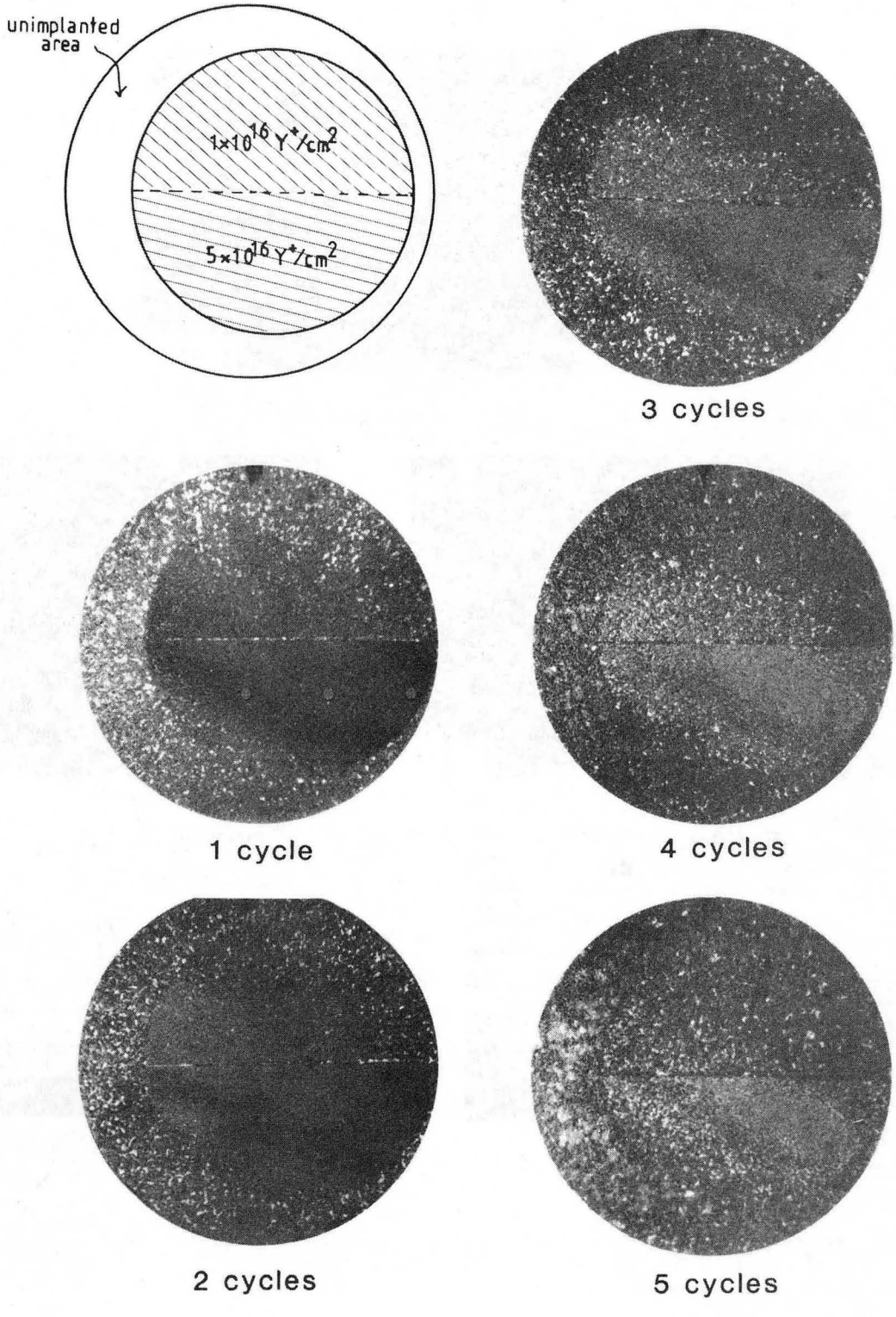

Figure 51

XBB 860-8780

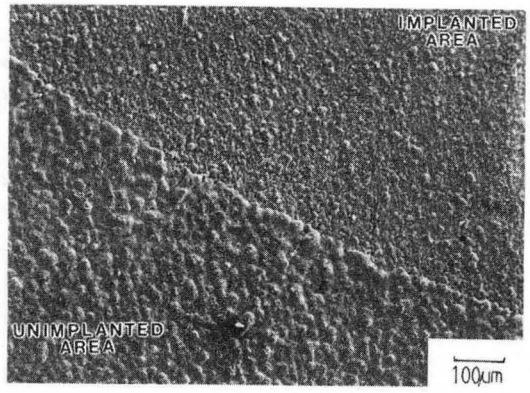

(a)

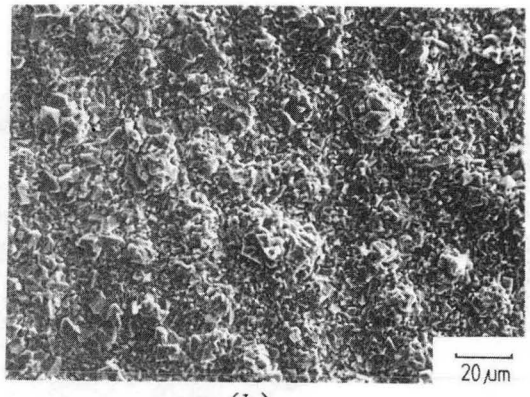

(b)

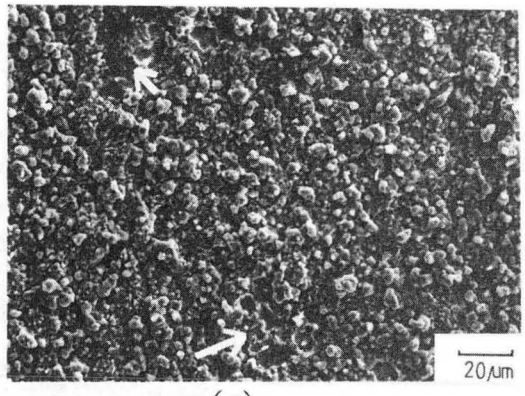

(c)

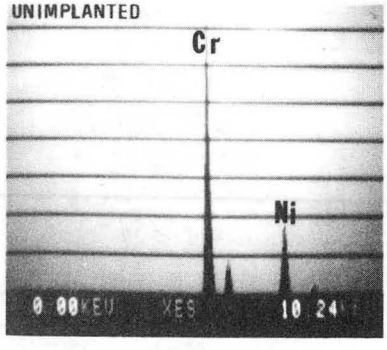

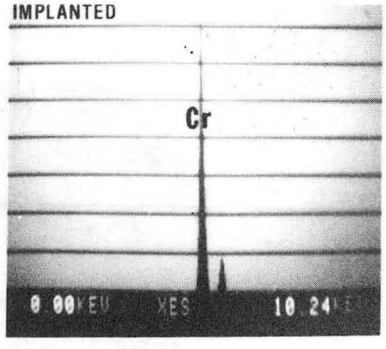

Figure 52

XBB 860-8778A

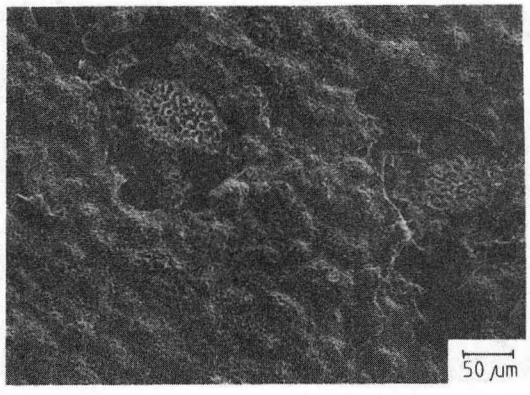

(a)

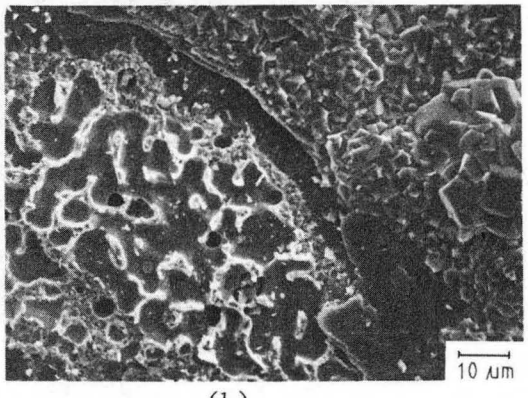

(b)

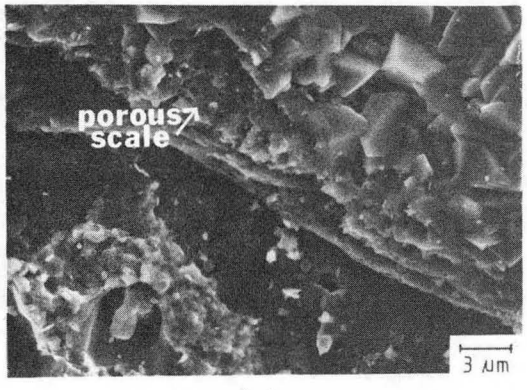

(c)

Figure 53

XBB 860-9550

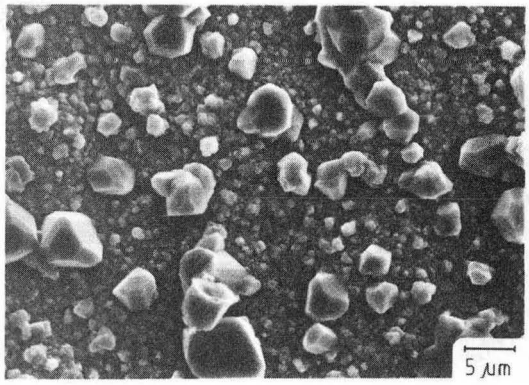

(a) $5x10^{16}$ Y^+/cm^2

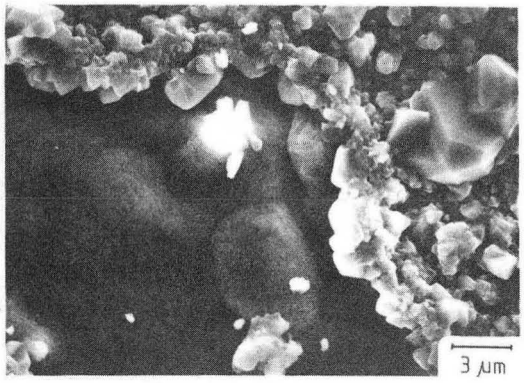

(b) $5x10^{16}$ Y^+/cm^2

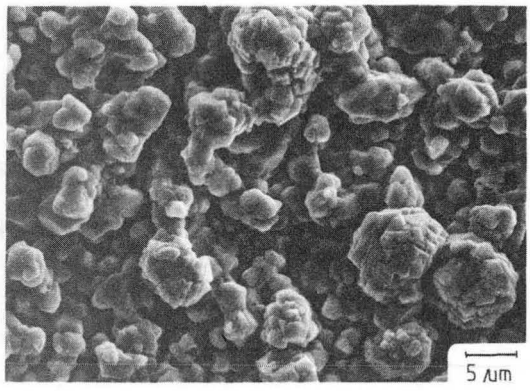

(c) $5x10^{15}$ Y^+/cm^2

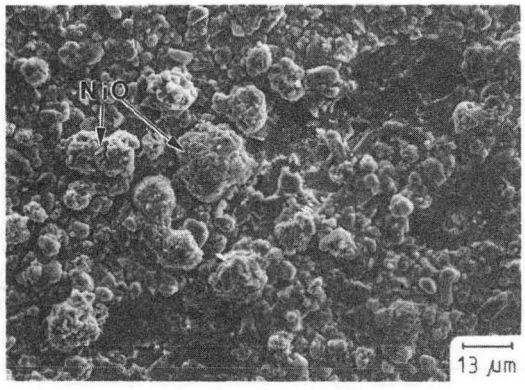

(d) $1x10^{15}$ Y^+/cm^2

Figure 54

XBB 860-9553

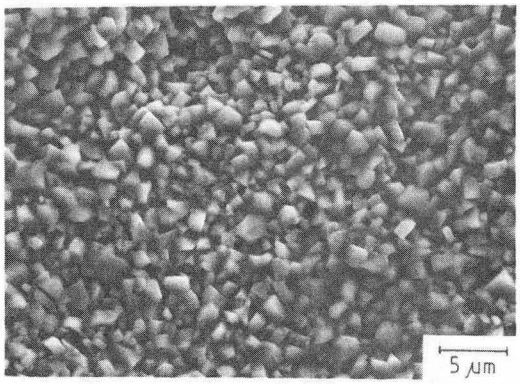

(a) $5x10^{15}$ Y^+

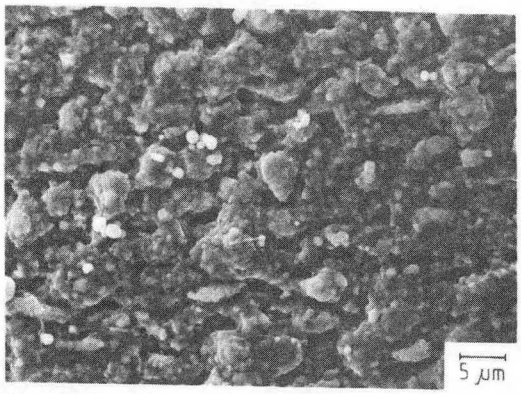

(b) $5x10^{15}$ Y^+

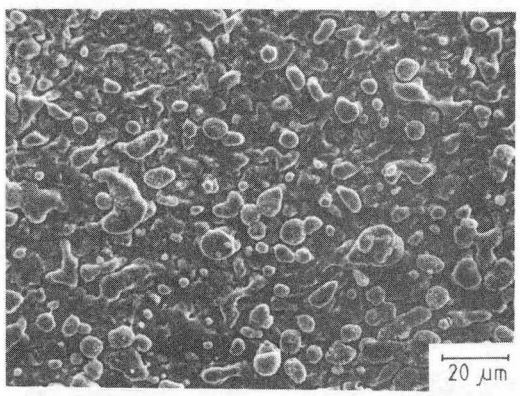

(c) $1x10^{15}$ Y^+

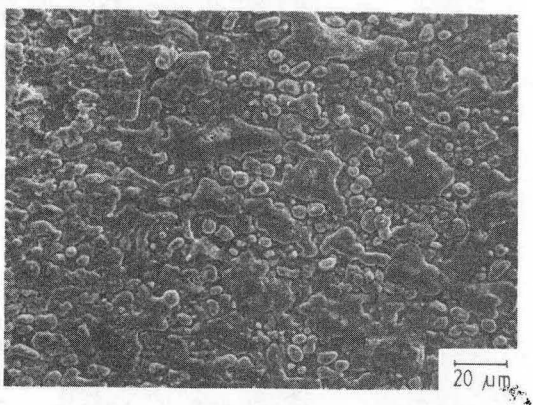

(d) unimplanted

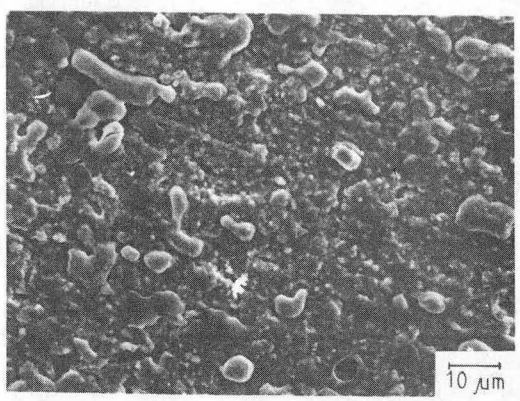

(e) $5x10^{15}$ Y^+, preoxidized

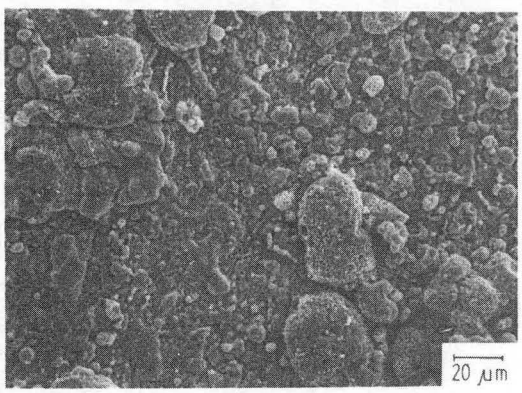

(f) $5x10^{15}$ Xe^+

Figure 55

XBB 860-9556

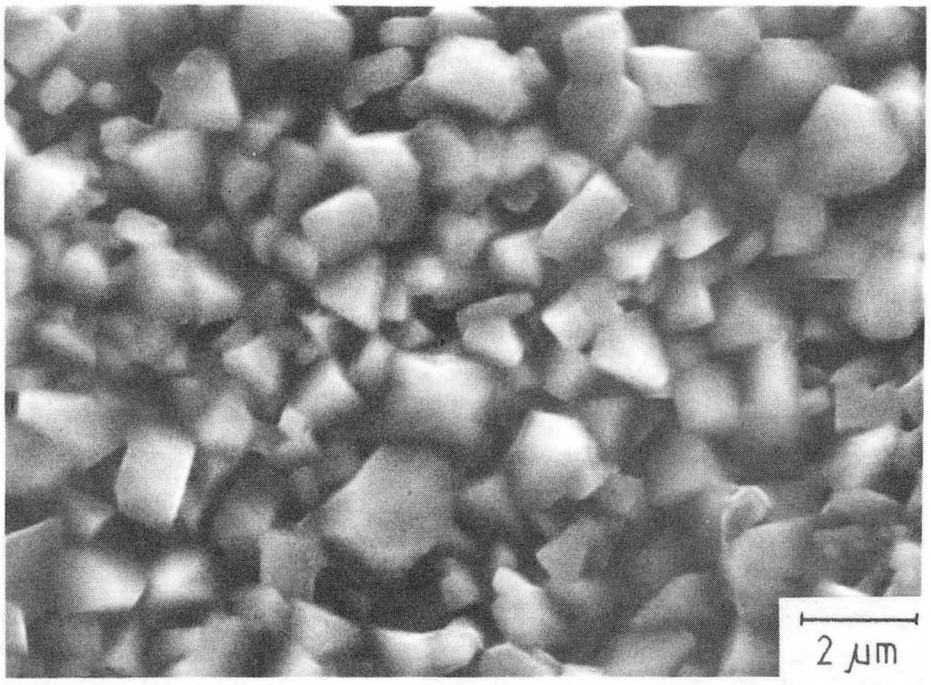

(a)

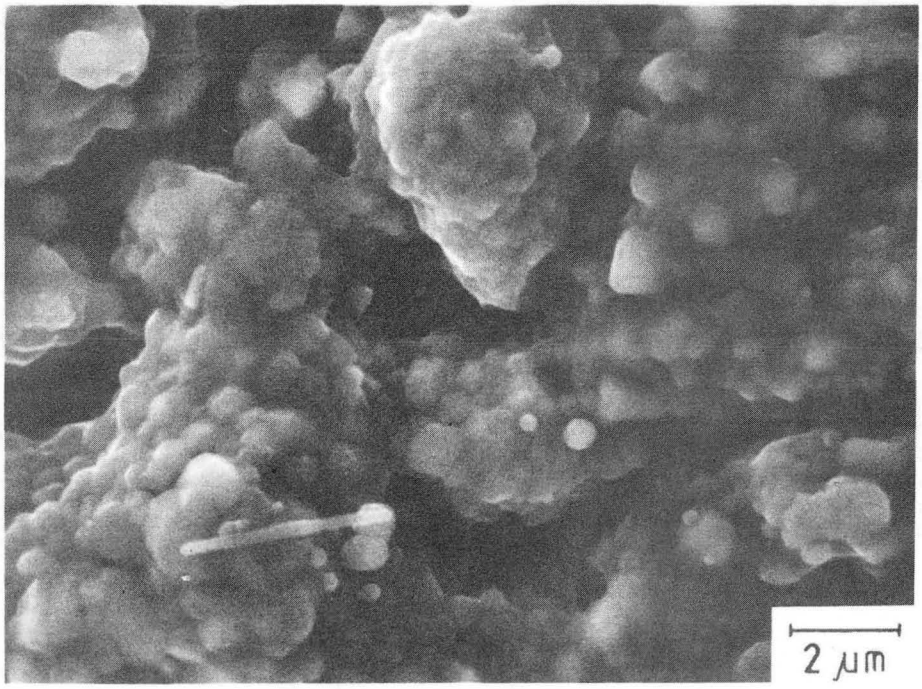

(b)

Figure 56

XBB 860-9548

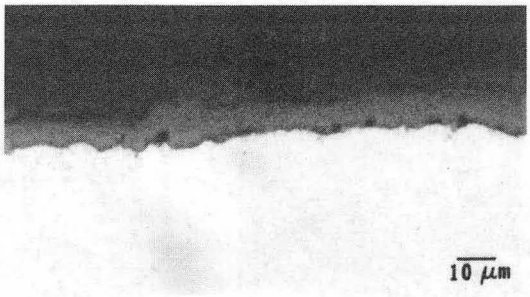

(a)

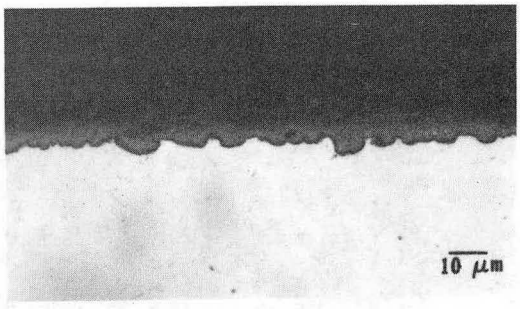

(b)

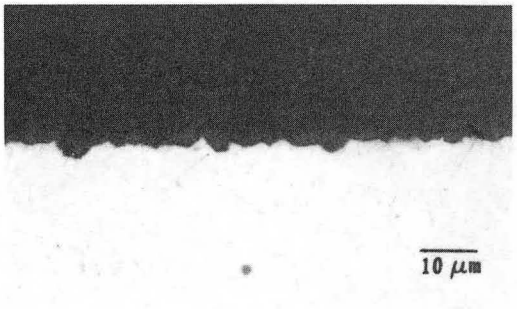

(c)

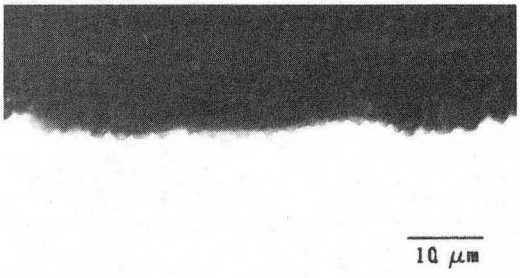

(d)

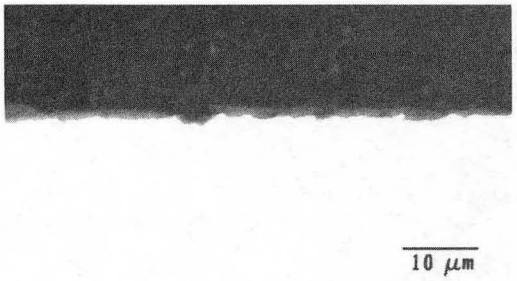

(e)

Figure 57

XBB 860-8775

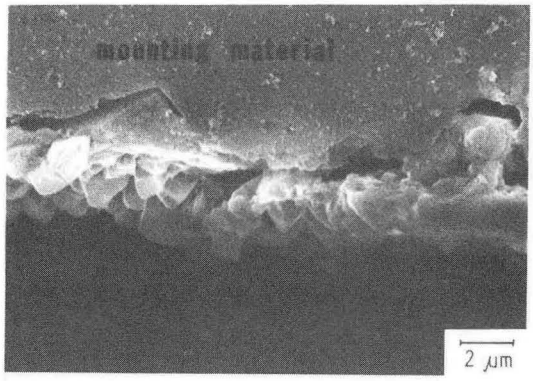

(a) $5x10^{}$ Y

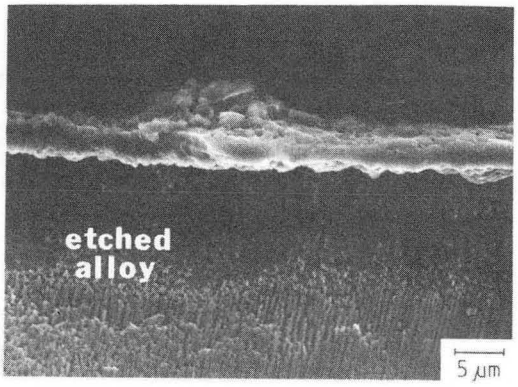

(b) $5x10^{16}$ Y^{+}, preoxidized

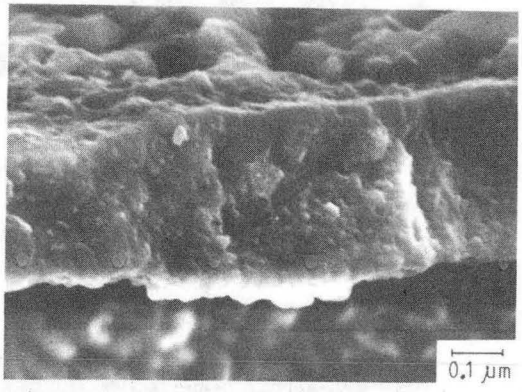

(c)

Figure 58

XBB 860-9551

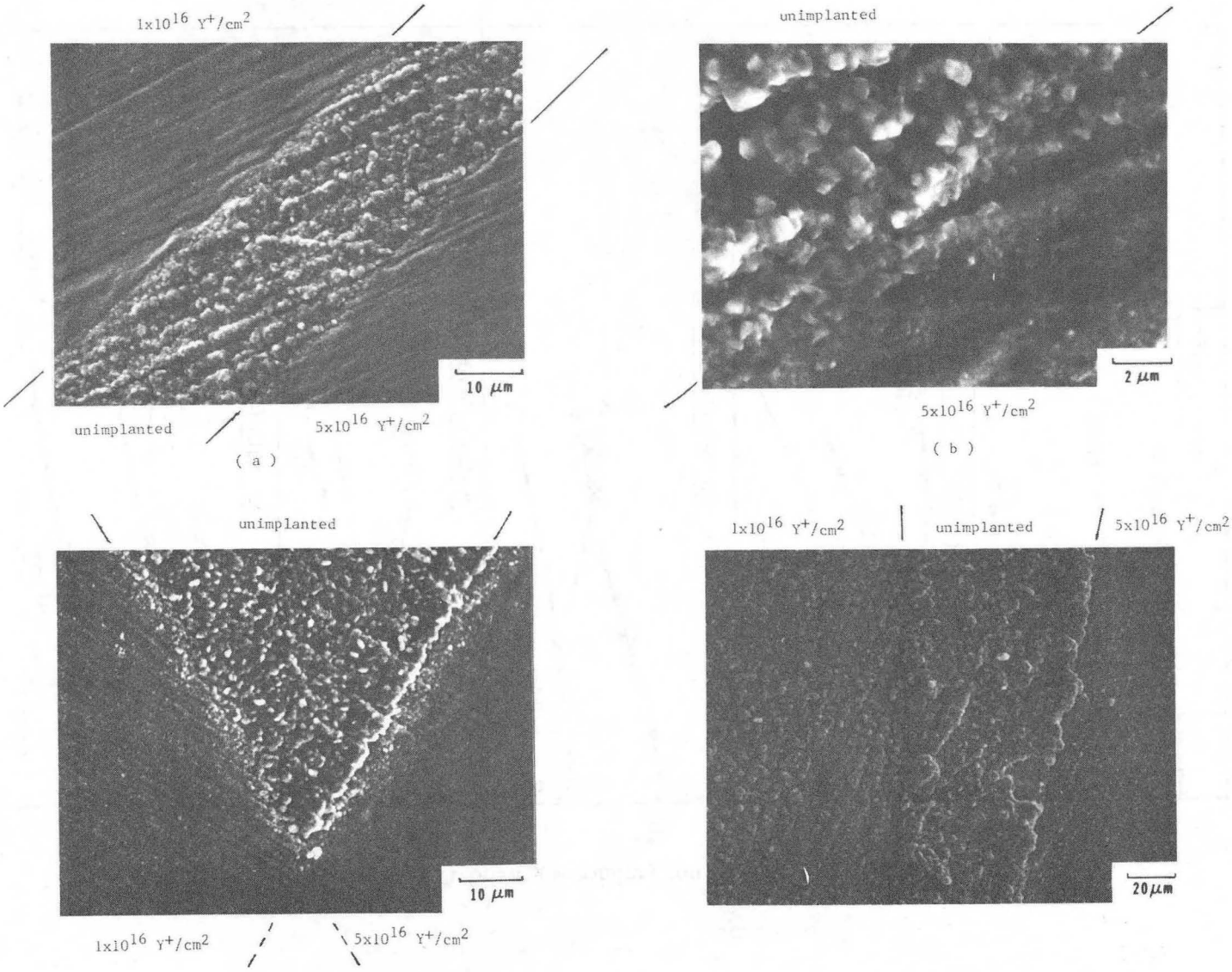

Figure 59

XBB 860-8782

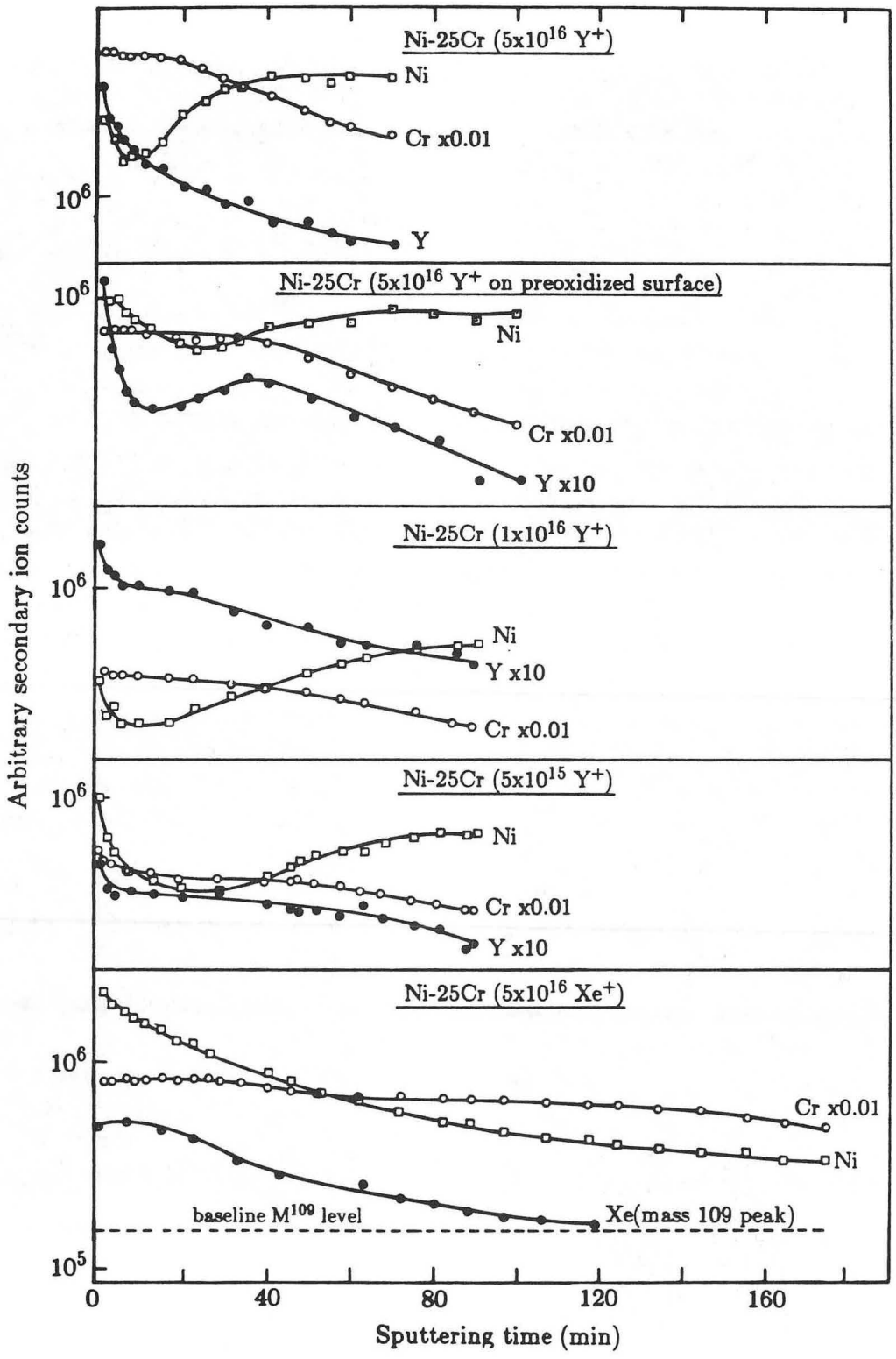

Figure 60

XBL 8612-4805

After Implantation

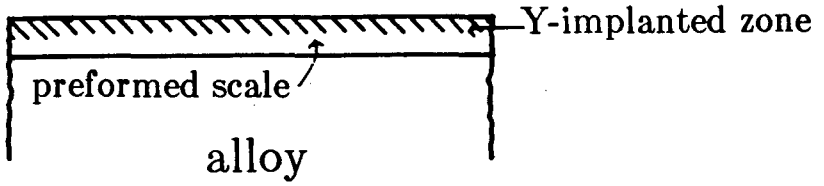

After Oxidation

I) Growth by chromium outward diffusion

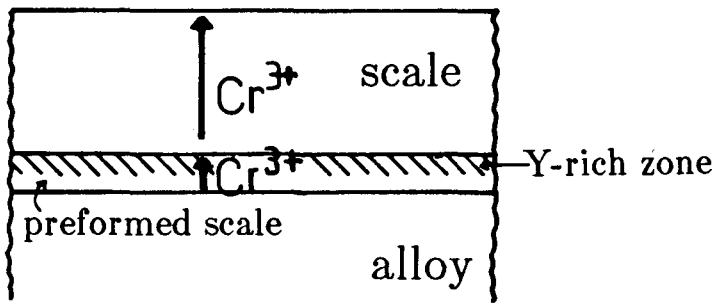

II) Growth by oxygen inward diffusion

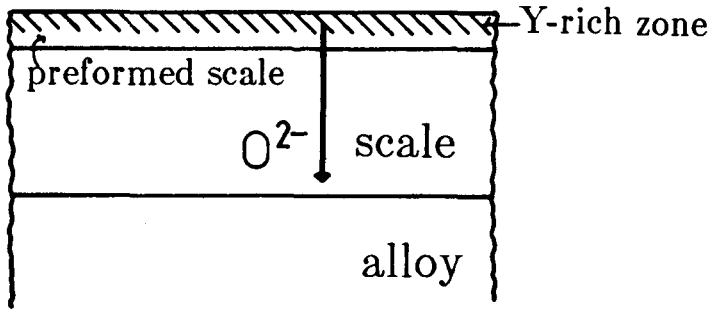

III) Growth by oxygen inward diffusion but fast chromium diffusion through preformed oxide layer

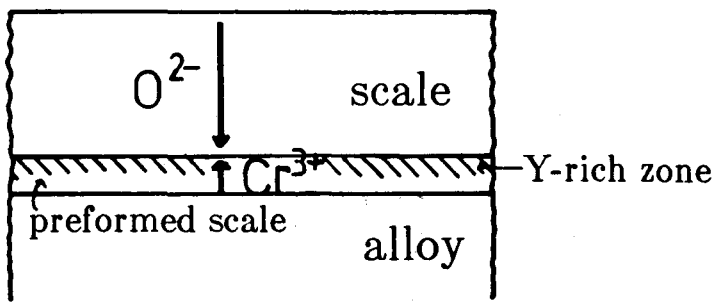

Figure 61

XBL 8612-4794

Ni - 25 Cr (Hf)

(I) INITIAL SCALE DEVELOPMENT

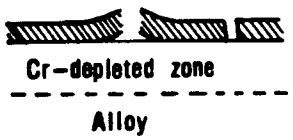

(II) CRACKING OF INITIAL SCALE

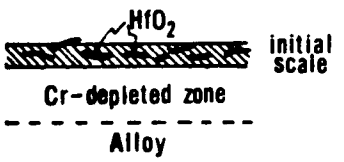

Exposing Cr-depleted region to oxidant
Leads to fast oxidation of base metal
and further damage of the initial scale

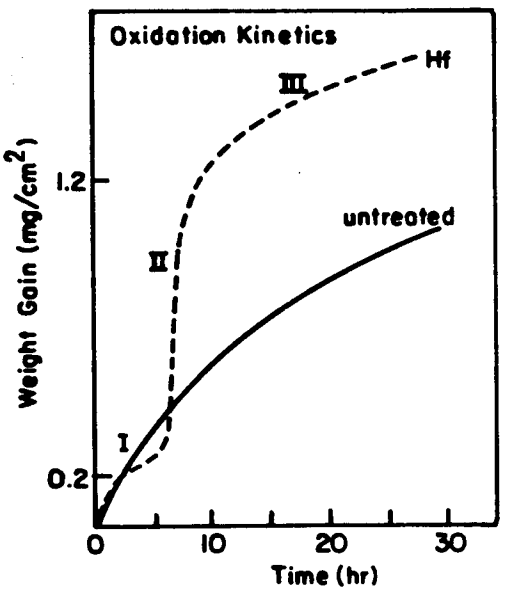

(III) Cr_2O_3 HEALING LAYER DEVELOPS

Subsequent oxidation involves
growth of this layer

Growth rate is similar to
that of the untreated Ni-25Cr

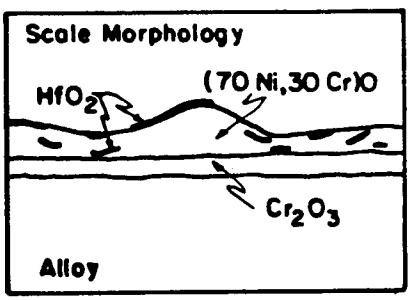

Figure 62

XBL866-7694

LAWRENCE BERKELEY LABORATORY
TECHNICAL INFORMATION DEPARTMENT
UNIVERSITY OF CALIFORNIA
BERKELEY, CALIFORNIA 94720